

**Transmission electron microscopy investigation of the microstructural mechanisms for
the piezoelectricity in lead-free perovskite ceramics**

by

Cheng Ma

A dissertation submitted to the graduate faculty
in partial fulfillment of the requirements for the degree of
DOCTOR OF PHILOSOPHY

Major: Materials Science and Engineering

Program of Study Committee:
Xiaoli Tan, Major Professor
Mufit Akinc
Nicola Bowler
Scott P. Beckman
Gordon J. Miller

Iowa State University

Ames, Iowa

2012

Copyright © Cheng Ma, 2012. All rights reserved.

DEDICATION

I would like to dedicate this thesis to my parents for their continuous love in my life.

TABLE OF CONTENTS

| | |
|---|------------|
| ABSTRACT..... | vii |
| CHAPTER 1. Introduction | 1 |
| 1.1 Motivation | 1 |
| 1.2 Dissertation organization..... | 6 |
| References..... | 8 |
| CHAPTER 2. Literature Review..... | 10 |
| 2.1 Piezoelectricity | 10 |
| 2.1.1 Direct and converse effect | 10 |
| 2.1.2 Symmetry requirement..... | 12 |
| 2.2 Ferroelectrics | 13 |
| 2.2.1 Definition and importance to piezoelectricity..... | 13 |
| 2.2.2 Perovskite structure..... | 16 |
| 2.2.3 Ferroelectric domains..... | 19 |
| 2.2.4 Normal ferroelectrics | 22 |
| 2.2.5 Relaxor ferroelectrics..... | 26 |
| 2.2.6 Morphotropic phase boundary (MPB) | 32 |
| 2.3 Antiferroelectrics and ferrielectrics..... | 33 |

| | | |
|-------|--|-----------|
| 2.4 | (Bi _{1/2} Na _{1/2})TiO ₃ -BaTiO ₃ solid solutions..... | 36 |
| 2.4.1 | (Bi _{1/2} Na _{1/2})TiO ₃ | 37 |
| 2.4.2 | Reported phase diagram..... | 40 |
| 2.4.3 | Structure-property relationship | 43 |
| 2.4.4 | Ferroelectric domain structure | 46 |
| | References..... | 47 |
| | CHAPTER 3. Experiment Details..... | 51 |
| 3.1 | Polycrystalline ceramic preparation | 51 |
| 3.2 | Dielectric/ferroelectric/piezoelectric characterization..... | 52 |
| 3.3 | Transmission electron microscopy (TEM) study | 53 |
| | CHAPTER 4. Domain Structure-Dielectric Property Relationship in Lead-Free (1-x)(Bi_{1/2}Na_{1/2})TiO₃-xBaTiO₃ Ceramics..... | 56 |
| | Abstract | 56 |
| 4.1 | Introduction | 57 |
| 4.2 | Experimental procedure | 61 |
| 4.3 | Results | 63 |
| 4.3.1 | Dielectric characterization | 63 |
| 4.3.2 | TEM study | 64 |
| 4.4 | Discussion | 68 |

| | |
|---|-----|
| 4.5 Conclusions | 75 |
| Acknowledgements..... | 76 |
| Figures..... | 77 |
| References..... | 87 |
| CHAPTER 5. <i>In situ</i> Transmission Electron Microscopy Study on the Phase Transitions in Lead-Free $(1-x)(\text{Bi}_{1/2}\text{Na}_{1/2})\text{TiO}_3-x\text{BaTiO}_3$ Ceramics..... 89 | |
| Abstract..... | 89 |
| 5.1 Introduction | 90 |
| 5.2 Experimental procedure | 92 |
| 5.3 Results and discussion..... | 93 |
| 5.3.1 Phase transitions across T_d | 93 |
| 5.3.2 Transitions across and beyond T_{RE} and T_m | 97 |
| 5.4 Conclusions | 101 |
| Acknowledgements..... | 101 |
| Figures..... | 103 |
| References..... | 110 |
| CHAPTER 6. Creation and Destruction of Morphotropic Phase Boundaries through Electrical Poling of Ferroelectric Materials.....113 | |
| Abstract..... | 113 |

| | | |
|-----|---|------------|
| 6.1 | Introduction | 114 |
| 6.2 | Experiments and methods | 118 |
| 6.3 | Results and discussion..... | 119 |
| 6.4 | Conclusions | 125 |
| | Acknowledgements..... | 126 |
| | Figures..... | 127 |
| | Supplemental material | 131 |
| | References..... | 135 |
| | CHAPTER 7. Concluding Remarks..... | 138 |
| 7.1 | General conclusions | 138 |
| 7.2 | Directions for future research..... | 141 |
| | References..... | 144 |
| | ACKNOWLEDGEMENTS | 146 |
| | APPENDIX: Publication List | 148 |

ABSTRACT

Lead-free materials with superior piezoelectricity are in increasingly urgent demand in the current century, because the industrial standard $\text{Pb}(\text{Zr},\text{Ti})\text{O}_3$ -based piezoelectrics, which contain over 60 weight% of the toxic element lead, pose severe environmental hazards. Although significant research efforts have been devoted in the past decade, no effective lead-free substitute for $\text{Pb}(\text{Zr},\text{Ti})\text{O}_3$ has been identified yet. One of the primary hindrances to the development of lead-free piezoelectrics lies in the ignorance of the microstructural mechanism for the electric-field-induced strains in the currently existing compositions.

In this dissertation, the microstructural origin for the high piezoelectricity in $(1-x)(\text{Bi}_{1/2}\text{Na}_{1/2})\text{TiO}_3-x\text{BaTiO}_3$ [(1- x)BNT- x BT], the most widely studied lead-free piezoelectric system, has been elucidated. The combination of dielectric characterization and conventional transmission electron microscopy (TEM) demonstrates that the phase relationship for unpoled ceramics is different from that for poled ceramics. This discovery leads to the update of the BNT-BT phase diagram that has been widely accepted for 20 years. The hot-stage TEM study further extends the updated phase diagram to 600 °C and clarifies the complicated relationship between the crystal/domain structures and dielectric properties. Based on these findings, the electric-field *in-situ* TEM investigation reveals that the morphotropic phase boundary (MPB) in this system, along with the associated

piezoelectricity enhancement, could be created, destroyed, or even replaced by another MPB during electrical poling, an indispensable process for ferroelectric materials to exhibit usable piezoelectricity. The optimal piezoelectric response in the originally single-phase composition $x = 7\%$ is found to be the result of a stable MPB induced by electric fields during poling.

The discovery summarized in this dissertation not only elucidates the microstructural mechanism for the high piezoelectricity in BNT-BT, but also fundamentally alters the long-standing guiding rule for designing superior piezoelectric materials. It suggests that even single-phase compositions, which were largely excluded before, may also exhibit strong piezoelectricity if stable MPBs form during poling. Such a paradigm shift adds a new dimension to the development of next generation high-performance piezoelectrics.

CHAPTER 1. Introduction

1.1 Motivation

Piezoelectric materials, which enable the conversion between mechanical and electrical energies,¹⁻³ are crucial in a wide range of applications including energy harvesting,⁴ medical imaging,^{3,4} and minimally invasive surgery,⁵ etc.. For the past six decades, Pb(Zr,Ti)O₃-based materials have been dominating the piezoelectric industry due to their excellent properties, ease of processing, and low cost.¹⁻³ However, these materials contain over 60 weight% of the toxic element lead.³ The calcination and sintering of Pb(Zr,Ti)O₃ (where PbO evaporates), the hard machining of components, and the recycling/waste disposal process, etc., are all releasing considerable amounts of lead into the environment.³ The lead pollution associated with the piezoelectric industry is causing more and more severe hazards to the environment and human health.³ As a result, the restriction of lead use in electronic devices has been demanded by legislations in many regions in the world, including the European Union, part of Asia, and several U.S. states.³ Lead-free materials with piezoelectric properties comparable to Pb(Zr,Ti)O₃ are in urgent demand.³

The world-wide search for lead-free piezoelectric materials began at around 2000.³ One decade of intensive research efforts have identified two lead-free piezoelectric systems with promising performances (Fig. 1.1): the alkali-niobium-based compounds (Na_{1-x}K_x)NbO₃,

and the bismuth-alkali-based compounds $(Bi_{1/2}Na_{1/2})TiO_3$ -BaTiO₃. Over the years, various chemical modifications and processing techniques have been implemented on these two systems to improve the piezoelectric properties. However, no effective lead-free replacement for Pb(Zr,Ti)O₃ has been identified yet.³ One of the primary hindrances to the development of lead-free piezoelectric materials is the ignorance of the microstructural mechanism for the relatively high performances of these two prototype compounds, especially $(Bi_{1/2}Na_{1/2})TiO_3$ -BaTiO₃ (abbreviated as BNT-BT in the following), the most extensively studied lead-free piezoelectric system (Fig. 1.1).

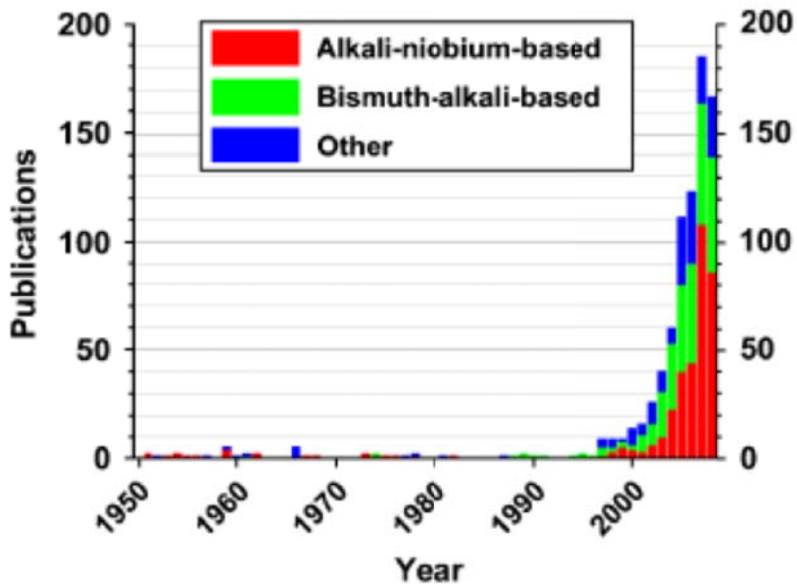


Figure 1.1 Publications on lead-free piezoelectrics in refereed journals for the time range from 1950 to November 2008.³ The alkali-niobium-based and bismuth-alkali-based compounds refer to $(Na_{1-x}K_x)NbO_3$ and $(Bi_{1/2}Na_{1/2})TiO_3$ -BaTiO₃, respectively.

Similar to the case of $\text{Pb}(\text{Zr},\text{Ti})\text{O}_3$,¹⁻³ the optimal piezoelectricity in BNT-BT emerges at the vicinity of the morphotropic phase boundary (MPB), where multiple ferroelectric phases coexist.³ Since BNT-BT solid solutions are essentially ferroelectric materials like $\text{Pb}(\text{Zr},\text{Ti})\text{O}_3$, they also need to be poled with electric fields in order to exhibit usable piezoelectricity.³ However, the microstructural mechanism for the high piezoelectricity in $\text{Pb}(\text{Zr},\text{Ti})\text{O}_3$ is apparently not applicable for BNT-BT. The most commonly accepted model for $\text{Pb}(\text{Zr},\text{Ti})\text{O}_3$ attributes the high piezoelectricity of the MPB compositions to a monoclinic phase bridging the rhombohedral and tetragonal ferroelectric phases.⁶ The low-symmetry monoclinic phase offers more polarizable directions and facilitates the polarization alignment process during poling, yielding an enhanced piezoelectric performance.⁶ In contrast, the piezoelectric response of $(1-x)\text{BNT}-x\text{BT}$, although significantly enhanced in the vicinity of the MPB, actually peaks at a single-phase composition $x = 7\%$.⁷ Moreover, unlike $\text{Pb}(\text{Zr},\text{Ti})\text{O}_3$, crystal structure changes were observed in BNT-BT after electrical poling.⁸⁻¹⁰ These imply the microscopic origin for the piezoelectric behavior of BNT-BT must be interpreted differently from that of $\text{Pb}(\text{Zr},\text{Ti})\text{O}_3$.

Knowledge of the real-time polarization alignment process during electrical poling is essentially important in studying the microstructural mechanism of the piezoelectricity, because poling imparts piezoelectricity to the originally non- or weak-piezoelectric materials and largely determine the induced piezoelectric performances.¹⁻³ However, such knowledge

is currently missing for BNT-BT. The alignment of polarizations under poling fields is manifested as the evolution of crystal structures and domain morphologies, which is very difficult to be thoroughly analyzed due to three primary difficulties. First of all, the crystal structures of different perovskite ferroelectric phases are often too similar to be well resolved by x-ray or neutron diffractions. It is particularly difficult to distinguish a material with coexisting phases from a single-phase material with a more complicated crystal structure. For example, there has been a continued debate on the crystal structures of the MPB compositions in $\text{Pb}(\text{Zr},\text{Ti})\text{O}_3$ (single monoclinic phase *vs.* mixed rhombohedral and tetragonal phases),^{6,11} the most important and widely studied piezoelectric material. Second, *in-situ* application of electric fields in ferroelectric materials inevitably leads to a large piezoelectric strain and causes a complicated shifting of the diffraction peaks ($\eta_{hkl} = (d_{hkl}^E - d_{hkl}^0)/d_{hkl}^0$, where η_{hkl} is the piezoelectric lattice strain, d_{hkl}^E and d_{hkl}^0 are the lattice spacing of the (hkl) plane with and without field, respectively).¹² Moreover, electric-field-induced domain texture has to be taken into account in the structural analysis. These complications make the phase identification using x-ray/neutron diffractions particularly challenging. Third, the x-ray and neutron diffractions cannot provide detailed information about ferroelectric domains, which are the fundamental microstructural units dictating the dielectric/ferroelectric/piezoelectric behaviors.¹ These difficulties keep the microstructural mechanism of the piezoelectricity in BNT-BT unknown for at least two decades.³

The transmission electron microscopy (TEM) can properly address the issues described above. Unlike x-ray/neutron diffraction, which analyzes the crystal structure by the average Bragg diffractions from multiple grains of the sample, TEM is capable of precisely resolving the crystal structure of each individual phase among mixed phases through selected area electron diffraction. In addition to diffraction peak positions/splittings that are subject to change with the presence of lattice strain, different crystal structures can be distinguished under TEM by extremely weak superlattice diffractions, which are invisible to x-ray/neutron diffraction.¹³ Because the presence of superlattice diffractions is not influenced by strains, the structural analysis could be properly performed even when considerably large strain exists in the lattice. Furthermore, *in-situ* TEM can directly visualize the real-time domain morphology evolution under electric field. However, TEM (especially electric-field *in-situ* TEM) study on bulk materials requires very delicate sample preparation, and thus the number of such studies is still very limited.¹⁴⁻¹⁸

In this dissertation, the microscopic origin of the high piezoelectricity in (1- x)BNT- x BT ceramics is explored using various TEM techniques. The conventional, hot-stage, and electric-field *in-situ* TEM studies are performed to investigate the microstructure evolution with composition, temperature, and electric field, respectively. The study focuses on several compositions in the range of $4\% \leq x \leq 11\%$, which contains the MPB region showing significantly enhanced piezoelectricity. The structural phase diagram for the virgin-state

ceramics are constructed through conventional and hot-stage TEM study. By comparing the structural characteristics and dielectric behaviors, the structure-property relationship is established. Based on these findings, the electric-field *in-situ* TEM is performed to study the evolution of crystal structure and domain morphology during electrical poling, which reveals the microstructural mechanism for the high piezoelectricity in BNT-BT.

1.2 Dissertation organization

Following the introduction chapter presented above, Chapter 2 provides an overview of piezoelectricity, ferroelectrics, and antiferroelectrics. The important concepts that will be frequently visited in this dissertation are described in detail. Following this is a comprehensive review of the current research status of the microscopic origin for the high piezoelectric performances in the BNT-BT system.

In Chapter 3, the procedures for sample preparation, electrical property measurement, and structural characterization are described. Especially, the specimen configuration, connection, and experimental setup of the unique electric-field *in-situ* TEM technique are illustrated in detail.

Chapter 4 is a paper published in *Journal of Applied Physics*. A detailed conventional TEM study is performed to reveal the crystal structure and domain morphologies of unpoled

(1- x)BNT- x BT ceramics with $x = 4\%$, 6% , 7% , 9% , and 11% . The composition-dependent phase relationship of unpoled ceramics is demonstrated to be different from that of poled ceramics for the first time. These results are summarized as a phase diagram for the unpoled BNT-BT ceramics.

Chapter 5 is a paper published in *Journal of the American Ceramic Society*. While Chapter 4 primarily focuses on the composition-dependent structure-property relationship at room temperature, this chapter investigates the temperature-dependent phase transitions in unpoled (1- x)BNT- x BT ceramics through hot-stage TEM. The results extend the phase diagram of unpoled BNT-BT ceramics constructed in Chapter 4 up to 600 °C. A comparison between this phase diagram and that of poled ceramics clearly suggests complicated phase transitions occur during the electrical poling of the compositions around the MPB ($x \sim 6\%$), which exhibit optimal piezoelectric property. A detailed electric-field *in-situ* TEM study that probes the structural evolution during poling is thus critical in interpreting the microstructural mechanism for the piezoelectricity in BNT-BT.

Chapter 6 is a paper under review in *Physical Review Letters*. Electric-field *in-situ* TEM is performed on three compositions, $x = 5.5\%$, 6% , and 7% . All of them are in the vicinity of the MPB. The detailed crystal structure and domain morphology evolution during electrical poling is visualized directly, and the phenomena in sharp contrast to

conventional expectations are observed. This study not only provides the microscopic origin for the high piezoelectricity in BNT-BT, but also alters the universal guiding rule for the development of high-performance piezoelectric materials.

Finally, Chapter 7 summarizes the main conclusions of this dissertation and proposes several perspectives that are worth of further in-depth investigation.

References

- ¹ B. Jaffe, W. R. Cook, and H. Jaffe, *Piezoelectric Ceramics* (Academic Press, London, 1971).
- ² G. H. Haertling, *J. Am. Ceram. Soc.* **82**, 797 (1999).
- ³ J. Rödel, W. Jo, K. Seifert, E. M. Anton, T. Granzow, and D. Damjanovic, *J. Am. Ceram. Soc.* **92**, 1153 (2009).
- ⁴ M. Ahart, M. Somayazulu, R. E. Cohen, P. Ganesh, P. Dera, H.-K. Mao, R. J. Hemley, Y. Ren, P. Liermann, and Z. Wu, *Nature* **451**, 545 (2008).
- ⁵ G. Pavlíková, R. Foltán, M. Horká, T. Hanzelka, H. Borunská, J. Šedý, *Int. J. Oral Maxillofac. Surg.* 2011, 40, 451.
- ⁶ R. Guo, L. E. Cross, S.-E. Park, B. Noheda, D. E. Cox, and G. Shirane, *Phys. Rev. Lett.* **84**, 5423 (2000).

- ⁷ W. Jo, J. E. Daniels, J. L. Jones, X. Tan, P. A. Thomas, D. Damjanovic, and J. Rödel, *J. Appl. Phys.* **109**, 014110 (2011).
- ⁸ W. Jo, T. Granzow, E. Aulbach, J. Rödel, and D. Damjanovic, *J. Appl. Phys.* **105**, 094102 (2009).
- ⁹ J. E. Daniels, W. Jo, J. Rödel, and J. L. Jones, *Appl. Phys. Lett.* **95**, 032904 (2009).
- ¹⁰ H. Simons, J. Daniels, W. Jo, R. Dittmer, A. Studer, M. Avdeev, J. Rödel, and M. Hoffman, *Appl. Phys. Lett.* **98**, 082901 (2011).
- ¹¹ K. A. Schoenau, L. A. Schmitt, M. Knapp, H. Fuess, R. A. Eichel, H. Kungl, and M. J. Hoffmann, *Phys. Rev. B* **75**, 184117 (2007).
- ¹² M. Hinterstein, J. Rouquette, J. Haines, Ph. Papet, M. Knapp, J. Glaum, and H. Fuess, *Phys. Rev. Lett.* **107**, 077602 (2011).
- ¹³ D. I. Woodward and I. M. Reaney, *Acta Cryst. B* **61**, 387 (2005).
- ¹⁴ Y. Sato, T. Hirayama, and Y. Ikuhara, *Phys. Rev. Lett.* **107**, 187601 (2011).
- ¹⁵ X. Tan, Z. Xu, J. K. Shang, and P. Han, *Appl. Phys. Lett.* **77**, 1529 (2000).
- ¹⁶ H. He and X. Tan, *Phys. Rev. B* **72**, 024102 (2005).
- ¹⁷ X. Tan, C. Ma, J. Frederick, S. Beckman, and K. G. Webber, *J. Am. Ceram. Soc.* **94**, 4091 (2011).
- ¹⁸ C. A. Randall, D. J. Barber, and R.W. Whatmore, *J. Microsc.* **145**, 275 (1987).

CHAPTER 2. Literature Review

This chapter provides a technical background for the dissertation. It begins with a general introduction of the piezoelectric phenomenon. Following this is a detailed description of the characteristics of ferroelectric and antiferroelectric materials, as well as the influence of these characteristics on piezoelectric properties. Finally, the current understanding of the structure, property, and structure-property relationship in $(\text{Bi}_{1/2}\text{Na}_{1/2})\text{TiO}_3$ - BaTiO_3 solid solutions is comprehensively reviewed.

2.1 Piezoelectricity

2.1.1 Direct and converse effect

The direct piezoelectric effect refers to the linear coupling between the mechanical stress and electric polarization.¹ The degree of this coupling is characterized by the piezoelectric coefficient d , which is intrinsic to the material. The direct piezoelectric effect can be described in the matrix expression as:

$$\begin{pmatrix} P_1 \\ P_2 \\ P_3 \end{pmatrix} = \begin{pmatrix} d_{11} & d_{12} & d_{13} & d_{14} & d_{15} & d_{16} \\ d_{21} & d_{22} & d_{23} & d_{24} & d_{25} & d_{26} \\ d_{31} & d_{32} & d_{33} & d_{34} & d_{35} & d_{36} \end{pmatrix} \begin{pmatrix} X_1 \\ X_2 \\ X_3 \\ X_4 \\ X_5 \\ X_6 \end{pmatrix}$$

where P is the electric polarization, X is the stress, and d is the piezoelectric coefficient.

The subscripts indicate the directions of the components of these physical quantities.

The converse piezoelectric effect refers to the linear coupling between the mechanical strain (x) and applied electric field (E). Thermodynamic arguments suggest equivalence between the direct and converse piezoelectric effect,¹ so the piezoelectric coefficient d is also used to describe the converse effect. Similar to the direct piezoelectric effect, the converse effect can also be expressed in matrix:

$$\begin{pmatrix} x_1 \\ x_2 \\ x_3 \\ x_4 \\ x_5 \\ x_6 \end{pmatrix} = \begin{pmatrix} d_{11} & d_{21} & d_{31} \\ d_{12} & d_{22} & d_{32} \\ d_{13} & d_{23} & d_{33} \\ d_{14} & d_{24} & d_{34} \\ d_{15} & d_{25} & d_{35} \\ d_{16} & d_{26} & d_{36} \end{pmatrix} \begin{pmatrix} E_1 \\ E_2 \\ E_3 \end{pmatrix}$$

2.1.2 Symmetry requirement

The Neumann's principle states that the symmetry of any physical property of a crystal must include the symmetry elements of the point group of the crystal.¹ In another word, the piezoelectric matrix (d_{ij}) must not change after any symmetry operation within the point group of the crystal:

$$(d_{ij}) \xrightarrow{\text{symmetry operation}} (d'_{ij}) = (d_{ij}) \quad (1)$$

where (d_{ij}) and (d'_{ij}) are the piezoelectric matrices before and after the symmetry operation, respectively. Therefore, if the point group of the crystal contains such a symmetry operation that makes (d'_{ij}) = -(d_{ij}), which yields (d_{ij}) = -(d_{ij}) = 0 according to Eq (1), piezoelectricity is forbidden. As a result, only 20 among the total 32 crystallographic point groups allow piezoelectricity:¹ 1, 2, m, mm2, 222, 3, 32, 3m, 4, 6, $\bar{4}$, 4mm, 6mm, 422, 622, $\bar{4}2m$, $\bar{6}$, $\bar{6}m2$, $\bar{4}3m$, and 23.

In addition to single crystals, the basic conclusions deducted from the Neumann's principle are also applicable for polycrystalline materials. However, in the case of polycrystalline materials, the macroscopic symmetry of the entire sample rather than the crystal structure of each individual grain is concerned. Similar to the 32 crystallographic point groups describing the symmetry of the crystal structure, 7 Curie groups (∞ , ∞m , $\infty 2$, ∞/m , ∞/mm , $\infty\infty$, and $\infty\infty m$) are used to describe the macroscopic symmetry of the material.

After applying Neumann's principle on the piezoelectric matrix with the symmetry operations of these Curie groups, it is found that only 3 of them allow piezoelectricity:¹ ∞ , ∞m , and $\infty 2$.

It should be noted that none of the piezoelectric point groups (the 20 crystallographic point groups and 3 Curie groups mentioned above) contains centrosymmetry. Apparently centrosymmetry is not compatible with the presence of piezoelectricity. The as-sintered polycrystalline ceramics are macroscopically isotropic due to the random orientation of the grains. As a result, regardless of the crystal structure of the individual grains, they belong to the centrosymmetric Curie group $\infty\infty m$, which forbids piezoelectricity.¹ The macroscopic isotropy must be broken in order to introduce piezoelectricity into polycrystalline ceramics. This can be easily realized in materials displaying ferroelectricity.

2.2 Ferroelectrics

2.2.1 Definition and importance to piezoelectricity

Ferroelectric materials refer to a type of material with spontaneous electric polarizations that can be reversed by the externally applied electric field.² In order to exhibit ferroelectricity, the crystal structure (for both single crystals and polycrystalline materials) must be polar, i.e. the charge center of the cations and that of the anions must be

displaced.² The point groups satisfying this requirement coincide with the pyroelectric point groups, a subgroup of piezoelectric point groups.¹ In addition to the symmetry requirement, the spontaneous polarization of a ferroelectric material must also be reversible by the external electric field.² Therefore, only the pyroelectrics with electric-field-reversible polarizations are ferroelectrics. This relationship is illustrated in Fig. 2.1.

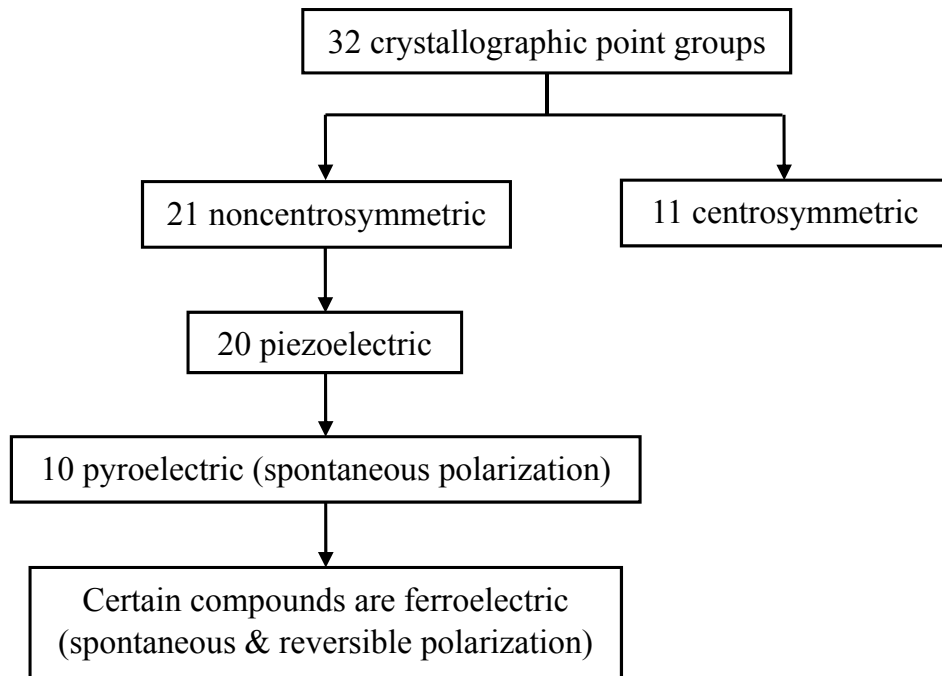


Figure 2.1 Symmetry requirements for piezoelectrics, pyroelectrics and ferroelectrics

Polycrystalline ceramics are much more widely used than single crystals in the piezoelectric industry due to the ease of processing and low cost.²⁻⁴ In order to exhibit

usable piezoelectricity, a polycrystalline ceramic must firstly be ferroelectric so that the macroscopic isotropy could possibly be broken under external driving forces.² By definition, the spontaneous polarization associated with the lattice is reversible by electric fields only in ferroelectric materials.² This nature allows the randomly oriented polarizations, which eliminate the macroscopic piezoelectricity in as-sintered ceramics, to be properly aligned by an intense electric field, yielding a piezoelectric Curie group ∞m .¹ The process of aligning polarizations with externally applied electric fields is referred to as electrical poling. The piezoelectricity of polycrystalline ceramics is directly influenced by the poling process. Therefore, the research of the structure-property relationships in piezoelectric ceramics is largely focused on the ferroelectric aspects.^{2,4}

As mentioned above, all of the piezoelectric ceramics, i.e. poled ferroelectric ceramics, belong to the Curie group ∞m , regardless of the crystal structure. After applying Neumann's principle (section 2.1.2), the piezoelectric matrix of poled ceramics must have the form:¹

$$\begin{pmatrix} 0 & 0 & 0 & 0 & d_{15} & 0 \\ 0 & 0 & 0 & d_{15} & 0 & 0 \\ d_{31} & d_{31} & d_{33} & 0 & 0 & 0 \end{pmatrix}$$

There are only three independent components for the piezoelectric coefficient. Among them, d_{33} is very frequently used to evaluate the piezoelectric performance of a polycrystalline ceramic, because it describes the polarization/strain that can be generated along the direction of the applied stress/electric field.

2.2.2 Perovskite structure

The perovskite structure is of significant technological importance with regard to the piezoelectric properties, as exemplified by the industrial standard piezoelectric material $\text{Pb}(\text{Zr},\text{Ti})\text{O}_3$ ² and the most extensively studied lead-free piezoelectric system BNT-BT.⁴ The compounds with perovskite structure possess the general formula ABO_3 . The prototypic perovskite structure is displayed in Fig. 2.2. It consists of a 3-dimensional lattice of corner-sharing BO_6 octahedra enclosing a cavity in which the 12-coordinated A cation locates. The prototypic perovskite structure is cubic, which is non-polar and centrosymmetric. Therefore, neither ferroelectricity nor piezoelectricity can be expected.

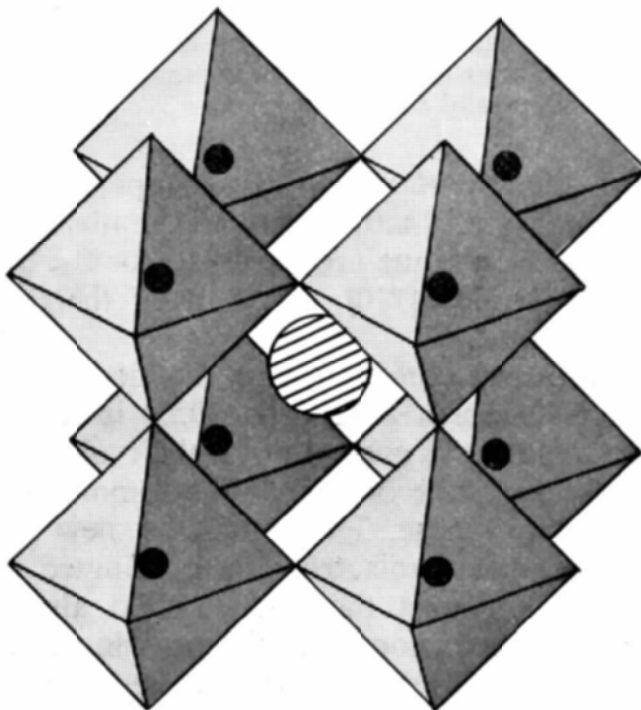


Figure 2.2 Prototypic perovskite structure with the general formula ABO_3 .⁵ The oxygen anions are the vertices of the octahedra, B cations the black circles, and A cations the hatched circle.

The ferroelectricity in perovskites can only exist in compounds which deviate from the prototypic structure in such a way that the charge centers of cations and anions are displaced and therefore spontaneous polarizations emerge in the unit cell.^{1,2} The deviations from the prototypic perovskite structure are artificially divided into two components:⁵ i) cation displacement, and ii) tilting of oxygen octahedra enclosing the B-site cations. Both of them may cause the displacement of cations/anions and induce polarization. Since the spontaneous polarization in perovskites arises from the distortions of the unit cell and lattice, the physical origins for the ferroelectric and piezoelectric behaviors are frequently interpreted

in terms of crystal structures. This can be well exemplified by $\text{Pb}(\text{Zr},\text{Ti})\text{O}_3$.¹ Figure 2.3 displays a portion of the phase diagram for $\text{Pb}(\text{Zr},\text{Ti})\text{O}_3$. Above the Curie temperature T_C , only the cubic structure is stable. No polarization exists because the charge centers of the cations and anions overlap. The material is paraelectric and thus cannot be poled to develop piezoelectricity. Below T_C , the rhombohedrally and tetragonally distorted structures are stable at the PbZrO_3 -rich and PbTiO_3 -rich sides, respectively. Although deviated differently from the prototypic structure, both rhombohedral and tetragonal phases carry spontaneous polarizations in their unit cells. In the rhombohedral phase, the displacement between the charge centers of cations and anions is along $\langle 111 \rangle$, forming a spontaneous polarization along the same crystallographic direction within the unit cell. Similarly, the tetragonal phase exhibits the charge center displacement along the $\langle 001 \rangle$ direction, and so as the orientation of the spontaneous polarization. Because of the flexibility of the perovskite structure, the orientations of these polarizations can be switched when exposed to sufficiently strong electric fields.² Therefore, they are ferroelectric. The polycrystalline ceramics exhibiting either of these two structures can be poled to exhibit piezoelectricity.

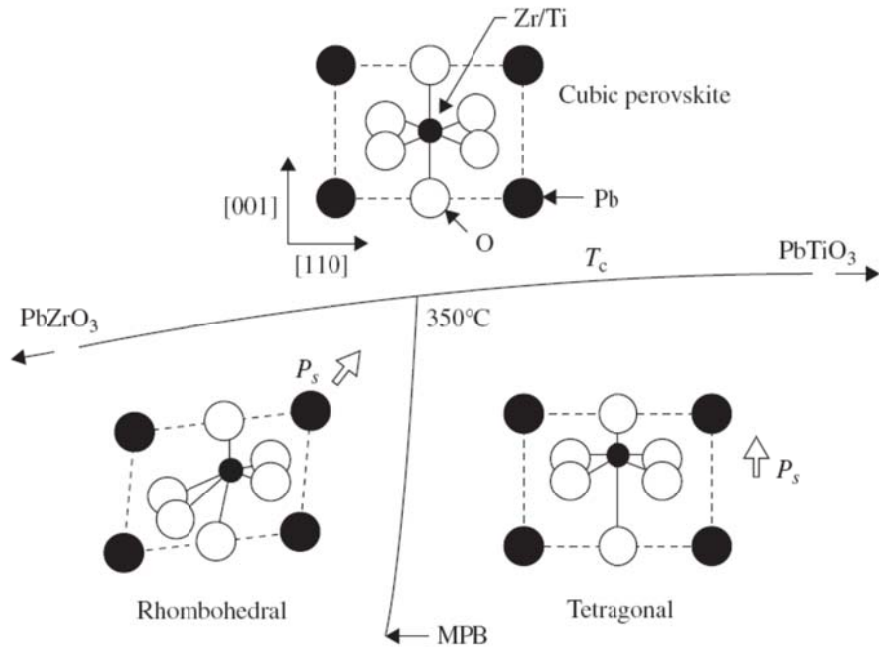


Figure 2.3 The spontaneous polarization P_s that arises from the charge center displacements in perovskite structures, as exemplified by a portion of the phase diagram of $\text{Pb}(\text{Zr},\text{Ti})\text{O}_3$.¹

2.2.3 Ferroelectric domains

In addition to the crystal structure, another microscopic feature is equivalently critical to the ferroelectric and piezoelectric properties of the material. This feature is the ferroelectric domain structure. As mentioned above, the spontaneous polarization in the unit cells of the perovskite compounds arises from the displacement between the charge centers of cations and anions. Since such displacements are considered occurring from the cubic structure that possesses many equivalent crystallographic orientations, they are not necessarily along any specific one of these equivalent orientations across the entire grain.

Instead, the grain is usually separated into several regions, each of which exhibits polarizations along one of the equivalent crystallographic orientations. Such regions are called ferroelectric domains.² The relationship between the grain and the domains within it can be well illustrated using BaTiO₃ as an example.⁶ The spontaneous polarization of the tetragonal BaTiO₃ is a result of distortion from the cubic BaTiO₃ along the *c* axis. Therefore, the cation/anion charge center displacement associated with such a distortion could possibly occur along any one of the six <001> directions. When the tetragonal phase is forming out of a grain of the cubic BaTiO₃, several regions starts to form within the grain, and each exhibits a uniform polarization orientation along one of the six <001> directions. Consequently, in the specific case of tetragonal perovskites, the polarizations of ferroelectric domains can only be 90° or 180° to each other within one grain, like the six <001> directions. Figure 2.4 is a schematic illustration for the ferroelectric domains within a single grain in BaTiO₃.

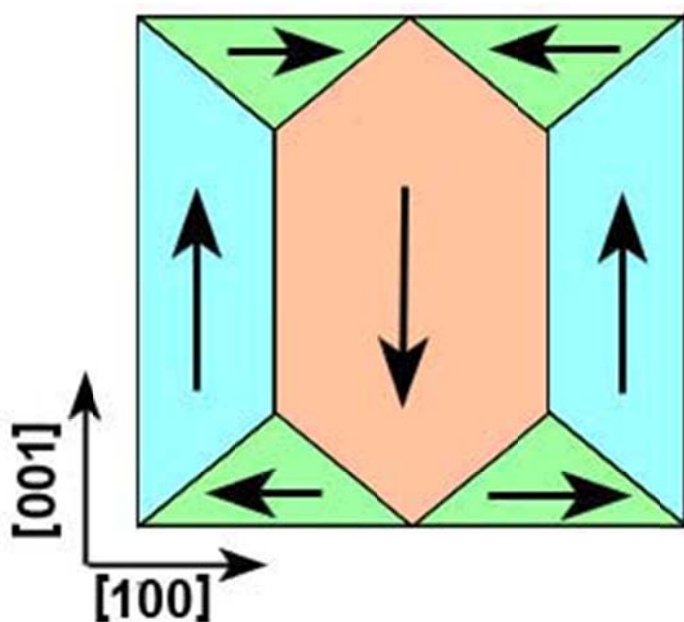


Figure 2.4 Schematic illustration of the ferroelectric domains within one grain of the tetragonal BaTiO_3 . The arrows are the directions of charge center displacement. The coordinates of the crystallographic directions follow the cubic system.

It should be pointed out that detailed domain morphologies cannot be revealed through the commonly used structural characterization techniques such as x-ray and neutron diffractions. The x-ray/neutron diffraction techniques analyze the beam diffracted from numerous grains. Therefore, only the average crystal structure of all these grains can be obtained, while the features related to the orientations of individual grains are largely missed. Since the domains differ only in orientations but not in crystal structures, it cannot be studied in detail through x-ray or neutron diffraction. However, the different orientations of the ferroelectric domains still generate different Bragg diffraction. Therefore, the domain structure can be imaged unambiguously under transmission electron microscope (TEM)

through the bright-field or centered-dark-field imaging techniques, which form the contrast primarily from Bragg diffractions.

The domain morphology significantly influences the dielectric, ferroelectric and piezoelectric behaviors of perovskite ceramics.^{4,7-10} The as-sintered ferroelectric ceramic needs to be poled under strong electric fields in order to develop usable piezoelectricity. The resulted piezoelectric performance depends on how well the originally randomly oriented polarizations are aligned by the field. This is largely determined, and also microstructurally manifested, by the evolution of ferroelectric domains during electrical poling.¹¹⁻¹³ The study of the ferroelectric domain structures and their evolution with composition, temperature, and, most importantly, electric fields, is critical in revealing the microstructural origin of the excellent performances in certain piezoelectric materials like BNT-BT. The importance of ferroelectric domains to the ferro- and piezoelectricity will also be reflected in the following sections.

2.2.4 Normal ferroelectrics

The ferroelectric behaviors may vary significantly due to the differences in domain structures, leading to different types of ferroelectric materials. This section and the following one introduce the characteristics of normal and relaxor ferroelectrics, respectively.

The microstructural origins of these two types of ferroelectric behaviors are critical to the studies presented in the following chapters of this dissertation.

The normal ferroelectric materials usually exhibit micrometer-sized ferroelectric domains.^{2,3} As an example of this type of domain structure, Fig. 2.5 shows the TEM bright-field image of the 90° domains of the tetragonal BaTiO₃.¹⁴ The domains with polarizations perpendicular to each other form lamellar patterns in the grain. The domain wall lies within the {011} plane, forming 45° angle with the polarizations of the two adjacent domains it separates. The size of these lamellar domains implies the polarization order occurs in the micrometer scale.

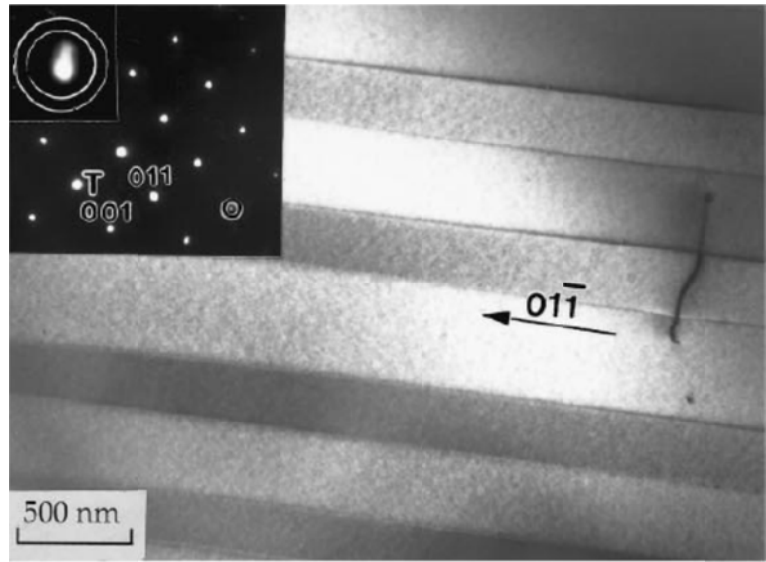


Figure 2.5 TEM bright-field image of the 90° ferroelectric domains in BaTiO₃ along the [100] zone axis.¹⁴ Inset: electron diffraction pattern along the [100] zone axis.

When exposed to a sufficiently strong electric field, the domains with polarizations closer to the external field direction grow, consuming those with polarizations farther away from the field direction.^{2,3} The macroscopic manifestation of this process is the alignment of the spontaneous polarizations along the applied field. When the field is removed, the domain morphology is mostly preserved, leaving a non-zero remanent polarization (P_r). When the field is applied towards the opposite direction, this polarization is suppressed and finally diminishes. The electric field required to return the material with a non-zero P_r to the zero-polarization state is referred to as the coercive field (E_C). If the electric field is applied alternately on the material, the polarization P vs electric field E curve form a closed loop, as displayed in Fig. 2.6. In addition to P_r and E_C that are reflected directly in the loop (Fig. 2.6), the spontaneous polarization P_s can be obtained by extrapolating the high-field portion of the P vs E curve to zero field. The P vs E loop with non-zero P_r and E_C is one of the most important characteristics for normal ferroelectric materials.^{2,3}

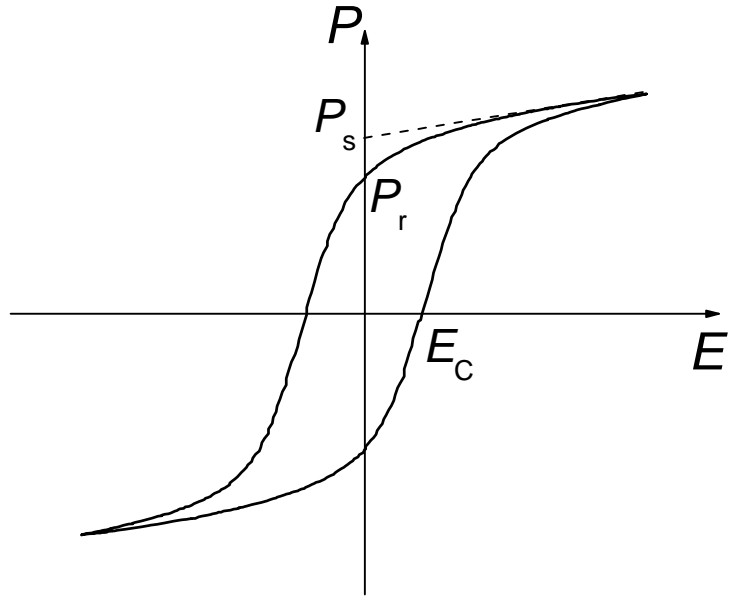


Figure 2.6 Typical polarization P vs electric field E hysteresis loop for the normal ferroelectrics. P_s , P_r , and E_C stands for spontaneous polarization, remanent polarization, and coercive field, respectively.

With increasing temperature, the polar crystal structure of normal ferroelectric materials will become cubic through a first-order phase transition. In terms of electric behaviors, the material loses the ferroelectricity and becomes paraelectric, which does not exhibit spontaneous polarization. The temperature where such a transition takes place is referred to as the Curie temperature (T_C). Above T_C , The dielectric permittivity ϵ_r follows the Curie-Weiss law: $\epsilon_r - 1 = C / (T - T_C)$, where C is the Curie constant.² For normal ferroelectric materials, the aforementioned transition occurs within a very narrow temperature range, resulting in a sharp peak in the permittivity ϵ_r vs temperature T curve (Fig. 2.7). Besides the anomaly at T_C , another important characteristic for normal ferroelectrics

revealed in Fig. 2.7 is the absence of frequency dependence in the magnitude of permittivity below T_c . The dielectric frequency dependence will be revisited during the discussion of relaxor ferroelectrics in the next section.

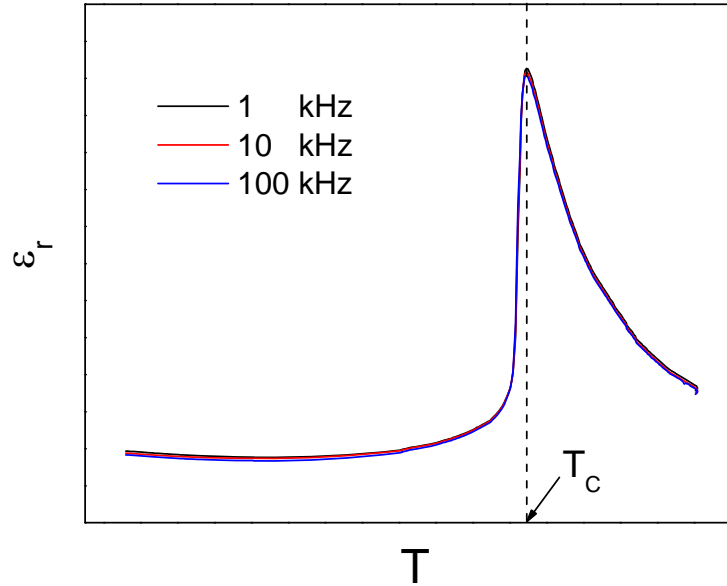


Figure 2.7 Typical temperature dependence of the permittivity (ϵ_r) for normal ferroelectric materials.

2.2.5 Relaxor ferroelectrics

Relaxor ferroelectrics are characterized by the polar nanoregions (PNRs), as schematically illustrated in Fig. 2.8.^{7,8} At high temperatures the relaxor ferroelectrics exist in a non-polar paraelectric phase, similar to the case of normal ferroelectrics. Upon cooling, the PNRs, rather than the micrometer-sized ferroelectric domains, emerge out of the matrix with the cubic structure. The polarizations of the PNRs are dynamically flipping among the

equivalent polar crystallographic directions due to the thermal fluctuation. At this stage all the possible polarization states of the PNRs can be experienced within a reasonable time, so the system is called “ergodic relaxor”.^{7,8} The temperature where the material transforms from the paraelectric state to the ergodic relaxor state is referred to as the Burns temperature (T_B). It should be noted that this transition is not associated with any change in the macroscopic crystal structure. However, since the PNRs give rise to unique physical behaviors, the transition across T_B is still considered as a phase transition.^{7,8} With further decreasing temperature below T_B , the dynamics of the PNRs slow down and are finally frozen into a non-ergodic state. The temperature where this transition takes place is referred to as the freezing temperature T_f .^{7,8} For some relaxors, the ergodic relaxor phase may transform into a normal ferroelectric phase at low temperature, and thus non-ergodic relaxor state cannot be achieved. In this case, the relaxor-to-normal-ferroelectric transition temperature is also called the Curie temperature T_C .⁷

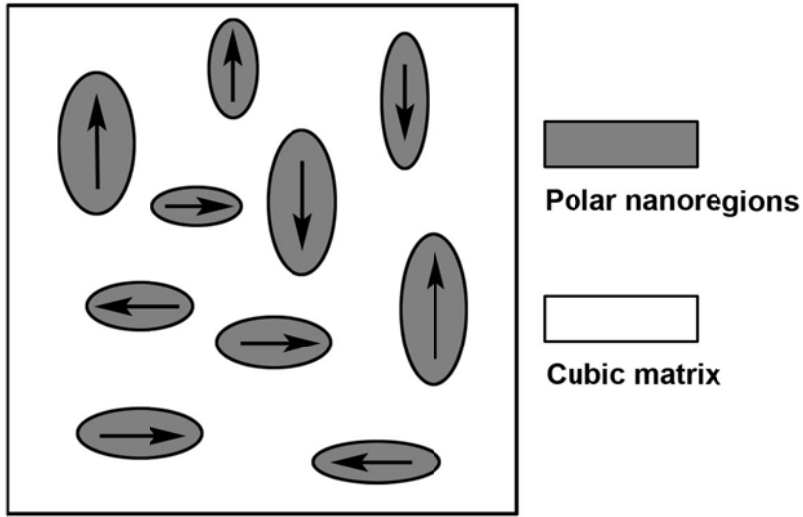


Figure 2.8 Schematic illustration of the PNRs in relaxor ferroelectrics.

The non-ergodic relaxor can irreversibly transform into a normal ferroelectric phase under a strong enough electric field.^{7,8} Therefore, the P vs E loops of the non-ergodic relaxors look almost identical to those of normal ferroelectrics. When heated, the electric-field-induced ferroelectric phase will transform to the ergodic relaxor at its Curie temperature T_C , which is very close to the freezing temperature T_f . Unlike the non-ergodic relaxor, the dipole moments in the high-temperature ergodic relaxor state are free to rotate. As a result, after removal of the externally applied field, the system largely returns to the state with randomly oriented polarizations. The typical P vs E loop for the ergodic relaxor is displayed in Fig. 2.9. The extremely low P_r implies that the ergodic relaxor is almost impossible to be effectively poled to develop piezoelectricity.

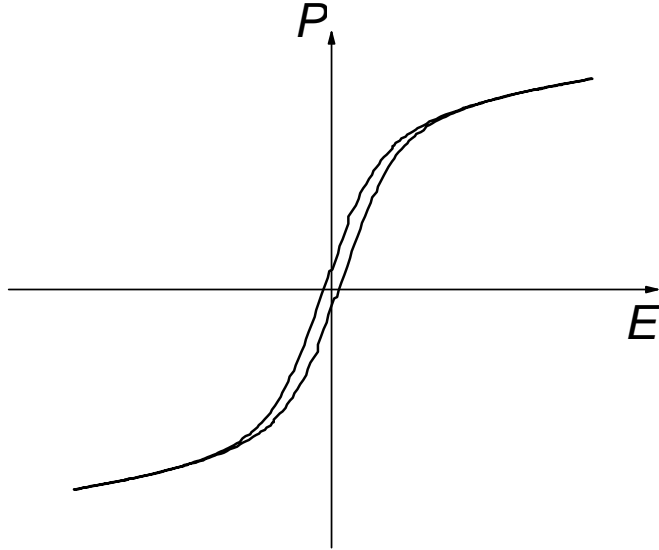


Figure 2.9 Typical polarization P vs electric field E hysteresis loop for the ergodic relaxor ferroelectrics.

The dielectric response of the relaxor ferroelectrics is closely related to the behaviors of PNRs. The typical temperature dependence of permittivity for relaxor ferroelectrics is displayed in Fig. 2.10, with critical temperatures indicated.⁷ At high temperatures where the paraelectric state is stable, the dielectric permittivity follows the Curie-Weiss law (section 2.2.4) and does not exhibit apparent frequency dependence. Below T_B , the ergodic PNRs emerges, leading to a minor frequency dispersion of the permittivity. This dispersion is referred to as the universal relaxor dispersion (URD). As temperature decreases, the freezing of the PNR dynamics occurs gradually, elongating the dipole relaxation time. This results in a wide permittivity peak and the emergence of significant dielectric frequency dispersion. The magnitude of permittivity at this peak is comparable to that at the anomaly

associated with T_C in normal ferroelectrics. However, unlike the latter case, this peak is very broad, and the temperature with the maximum permittivity, T_m , varies with frequency. Furthermore, it is only a dielectric anomaly associated with the freezing of PNRs and does not represent any structural change or phase transition. The additional dielectric frequency dispersion that suddenly arises around T_m is referred to as the conventional relaxor dispersion (CRD). It is believed that both URD and CRD contribute to the frequency dispersion below T_m (Fig. 2.10). With further decrease in temperature, the system could either be completely frozen into the non-ergodic relaxor below T_f , which does not leave any apparent anomaly in the dielectric curves [Fig. 2.10(a)], or transform into a normal ferroelectric phase, which leads to the truncation of the dielectric frequency dispersion by a sharp decrease of the permittivity [Fig. 2.10(b)]. For certain systems, the transition from the ergodic relaxor to the normal ferroelectric state (if occurring) may also take place before the temperature is low enough to show the entire frequency-dependent broad peak in the permittivity vs temperature curves. In this case, T_C coincides with T_m , the temperature where the permittivity peaks [Fig. 2.10(c)].

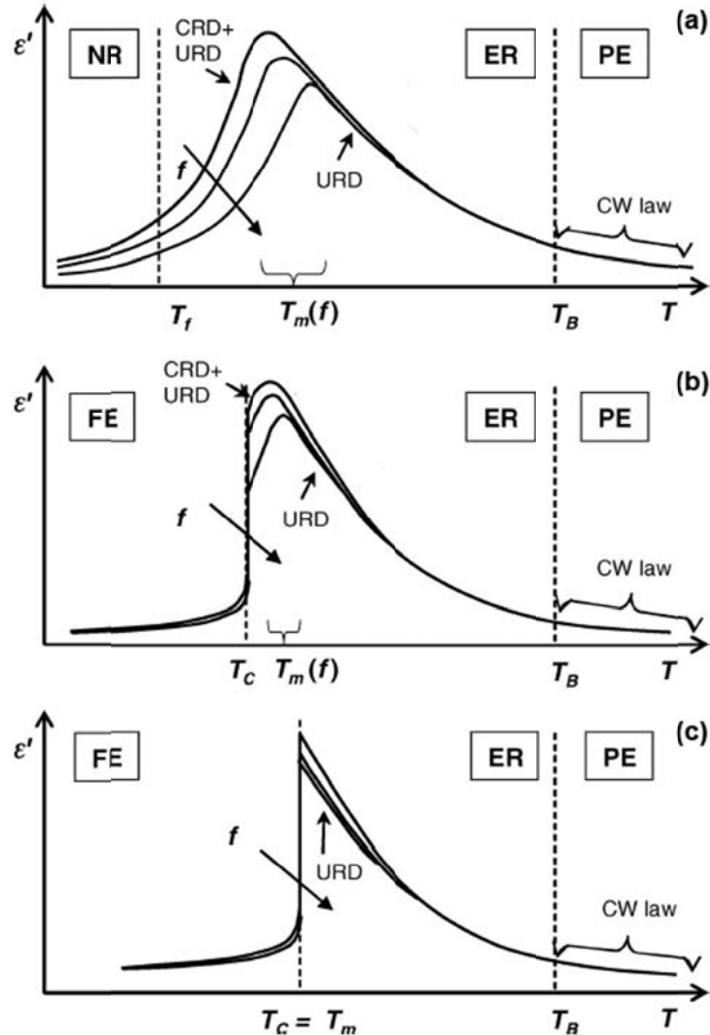


Figure 2.10 Different possibilities of temperature-dependent phase transitions and the associated permittivity ϵ' vs temperature T curves in relaxor ferroelectrics. (a) System without temperature-induced transition from the ergodic relaxor to normal ferroelectric phase; (b) System with a sharp relaxor-to-normal-ferroelectric transition at $T_C < T_m$; (c) System with a sharp relaxor-to-normal-ferroelectric transition at $T_C = T_m$. NR, ER, FE, PE, and CW stands for non-ergodic relaxor, ergodic relaxor, ferroelectric, paraelectric, and Curie-Weiss, respectively. This figure is adapted from ref. 7.

2.2.6 Morphotropic phase boundary (MPB)

The morphotropic phase boundary (MPB), where multiple ferroelectric phases coexist, offers significant enhancement in piezoelectricity.² Originally the term MPB specifically describes a phase boundary across which the ferroelectric-to-ferroelectric phase transition is induced by the composition change.² This is because, following the discovery of the large piezoelectricity in the composition-induced rhombohedral/tetragonal phase boundary of the industrial standard piezoelectric material $\text{Pb}(\text{Zr},\text{Ti})\text{O}_3$ (Fig. 2.3), composition variation in solid solutions has been the only approach to form ferroelectric-ferroelectric phase boundaries for nearly six decades.²⁻⁴ Recently pressure¹⁵ and epitaxial strain¹⁶ were also reported to induce the aforementioned phase boundaries, but they were still noted as MPBs. The term MPB is now used in a broader sense for a state where multiple ferroelectric phases coexist, regardless of the driving force for its formation.

Although MPBs give rise to superior piezoelectricity in various ferroelectric perovskite systems, the microstructural mechanism is still not conclusively established even for $\text{Pb}(\text{Zr},\text{Ti})\text{O}_3$. Recently a monoclinic symmetry was observed in $\text{Pb}(\text{Zr},\text{Ti})\text{O}_3$ within a very narrow composition range bridging the rhombohedral and tetragonal phase regions.¹⁷ One view thus proposed that the MPB is phase-pure with the monoclinic phase.^{17,18} A second view attributes the monoclinic distortion observed in x-ray diffraction to the result of the

coexisting rhombohedral and tetragonal nanodomains.¹⁹ The last one suggests the MPB is a broad region where all of the three phases mentioned above coexist, resulting in a macroscopic monoclinic symmetry as observed in x-ray diffraction.²⁰ Despite the existence of different microscopic models proposed for the piezoelectricity enhancement associated with MPBs, it is commonly accepted that the superior performances for compositions around the MPB should be attributed to the facilitation of the polarization rotation process during electrical poling.^{2-4,17-20}

2.3 Antiferroelectrics and ferrielectrics

As opposed to ferroelectrics that display parallel cation displacements and thus carry a non-zero spontaneous polarization in the unit cell, antiferroelectrics are a type of material that displays antiparallel cation displacements.²¹ The dipole moments associated with the antiparallel cation displacements set off each other completely, leading to a zero spontaneous polarization in the unit cell.²¹ The first compound that was found to exhibit antiferroelectricity is PbZrO_3 .²¹ Later the antiferroelectric characteristics were also observed in PbHfO_3 , $(\text{Bi}_{1/2}\text{Na}_{1/2})\text{TiO}_3$, NaNbO_3 , and AgNbO_3 , etc..²¹

When an antiferroelectric crystal is exposed to electric fields, the antiparallel dipoles can be flipped and forced to be parallel, corresponding to an electric-field-induced

antiferroelectric-to-ferroelectric phase transition.^{2,21} This transition is associated with an abrupt increase in polarization, as well as a significant change in other quantities such as strain and optical properties.²¹ Depending on the stability of the antiferroelectric phase, the electric-field-induced ferroelectric phase could either return to the original antiferroelectric phase, or be preserved after removing the fields.²¹ These two cases yield different polarization P vs electric field E hysteresis loops, as schematically shown in Fig. 2.11. For the former case [Fig. 2.11(a)], as fields decrease, the polarization will abruptly drop at a field slightly lower than the critical field of the antiferroelectric-to-ferroelectric transition in the first quarter of the electric field cycle; the reappearance of the antiferroelectric phase eliminates the large polarization in the induced ferroelectric phase. The remanent polarization P_r is zero because only the non-polar antiferroelectric phase exists at zero field. When the field is applied along the opposite direction, the phase transitions occur in the same sequence. As a result, a pinched hysteresis loop is observed. For the latter case [Fig. 2.11(b)], although the electric-field-induced antiferroelectric-to-ferroelectric transition will also give rise to a sharp increase of polarization during the very first quarter of the electric field cycle, upon removing the field the polarization does not vanish completely. Instead, a considerably large remanent polarization is present. The non-zero remanent polarization results from the persistence of the electric-field-induced ferroelectric phase. When further electric field cycles are applied, the original antiferroelectric phase will not appear again.

Therefore, the P vs E loop of this type of antiferroelectric material differs from that of a normal ferroelectric material only in the very first quarter of the electric field cycle. Apparently only the antiferroelectric materials showing irreversible electric-field-induced antiferroelectric-to-ferroelectric transition can possibly be poled to exhibit usable piezoelectricity.

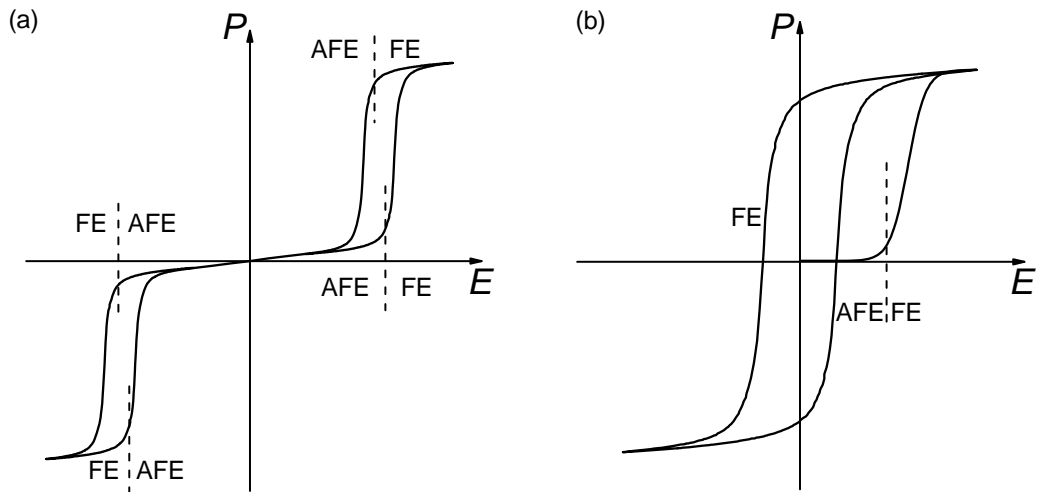


Figure 2.11 Typical polarization P vs electric field E hysteresis loop for the antiferroelectric materials with (a) reversible and (b) irreversible field-induced antiferroelectric-to-ferroelectric phase transitions. FE and AFE stands for ferroelectric and antiferroelectric, respectively.

Similar to the antiferroelectric materials, ferrielectric materials also exhibit antiparallel cation displacements. However, the dipole moments associated with these cation displacements do not set off each other completely, leaving a non-zero spontaneous polarization in the unit cell.²¹ While such a spontaneous polarization is usually very weak,

it still leads to macroscopic behaviors that are very similar to those of normal ferroelectric materials (e.g. non-zero P_r and E_C , etc.) in the low field level. When exposed to a sufficiently strong electric field, the antiparallel aligned dipoles are forced to a parallel configuration, corresponding to a ferrielectric-to-ferroelectric phase transition. Similar to antiferroelectrics, depending on the reversibility of this electric-field-induced phase transition, two different types of P vs E loops resembling those displayed in Fig. 2.11 could possibly be observed. The primary difference is, if the transition is reversible and thus the original ferrielectric phase is present at zero field, there would be a non-zero remanent polarization P_r and coercive field E_C in the pinched hysteresis loop.²¹ For certain systems, the dipole moments resulted from the antiparallel cation displacements are so small that P_r cannot be observed in the macroscopic P vs E measurement. These systems are frequently referred to as antiferroelectrics too.²¹ No matter whether the electric-field-induced ferrielectric-to-ferroelectric transition is reversible, the ferrielectric material may be poled to exhibit piezoelectricity.^{21,22} However, usually only those with irreversible transitions can develop reasonably strong piezoelectricity.^{21,22}

2.4 (Bi_{1/2}Na_{1/2})TiO₃-BaTiO₃ solid solutions

(1-x)(Bi_{1/2}Na_{1/2})TiO₃-xBaTiO₃ [(1-x)BNT-xBT] solid solution was first studied by Takenaka et. al..²³ It stands out among various solid solutions of BNT due to the high

piezoelectric performance and ease of processing.⁴ The compositions exhibiting most promising piezoelectric/electromechanical behaviors lie around $x = 6\text{--}7\%$, where an MPB is observed.^{23,24} An enhanced d_{33} value of ~ 170 pC/N was observed at $x = 7\%$,²⁴ and the mechanical strengths are about three times larger than $\text{Pb}(\text{Zr,Ti})\text{O}_3$.²³ Slight modifications of these compositions also lead to interesting behaviors. For example, a giant electric-field-induced strain has been observed in the $x = 6\%$ composition doped with minor amount of $(\text{K}_{0.5}\text{Na}_{0.5})\text{NbO}_3$ (< 3 mol.%).²⁵ The peak-field strain/field ratio reaches 560 pm/V, equivalent to 560 pC/N.²⁵ The $(1-x)\text{BNT-}x\text{BT}$ compounds with $x = 6\text{--}7\%$ may be regarded as pure BNT slightly modified with BT; most phases, structural transitions, and dielectric anomalies of these compositions are inherited from pure BNT. In this section, the characteristics of pure BNT will be introduced first, followed by an overview of the reported phase diagram, structure-property relationship, and the ferroelectric domain morphologies of $(1-x)\text{BNT-}x\text{BT}$ solid solutions. The issues that remain unresolved over years will also be discussed.

2.4.1 $(\text{Bi}_{1/2}\text{Na}_{1/2})\text{TiO}_3$

The BNT compound was first synthesized by Smolenskii et al. about 50 years ago.²⁶ With varying temperature, a series of complicated structural phase transitions with wide regions of coexisting phases occur.²⁷ The system is phase-pure with $R3c$ symmetry from

-268 to 255 °C, $P4bm$ symmetry from 400 to 500 °C, and $Pm\bar{3}m$ symmetry above 540 °C. The $R3c$ and $P4bm$ phases coexist between 255 °C and 400 °C, while the $P4bm$ and $Pm\bar{3}m$ phases were observed simultaneously between 500 °C and 540 °C. The room-temperature $R3c$ phase possesses a rhombohedrally distorted perovskite structure with the $a^-a^-a^-$ oxygen octahedra tilting. The tilting axis coincides with the polar axis, lying along the [111] direction. The presence of a polar axis in the crystal structure indicates a macroscopic ferroelectricity associated with this phase. The $P4bm$ phase at the intermediate temperature range exhibits antiparallel cation displacements, which arise from the oxygen octahedra tilting $a^0a^0c^+$. As schematically shown in Fig. 2.12, the A-site cations ($\text{Bi}^{3+}/\text{Na}^+$) and B-site cations (Ti^{4+}) are displaced oppositely along the [001] direction. The dipole moments associated with such antiparallel cation displacements do not cancel out each other, but leave a non-zero spontaneous polarization.^{21,27} Therefore, strictly speaking this $P4bm$ phase is ferrielectric.²¹ However, its spontaneous polarization is small,²⁷ which implies macroscopically this phase may behave like an antiferroelectric. The high-temperature $Pm\bar{3}m$ phase exhibit cubic symmetry, and is thus expected to be paraelectric.

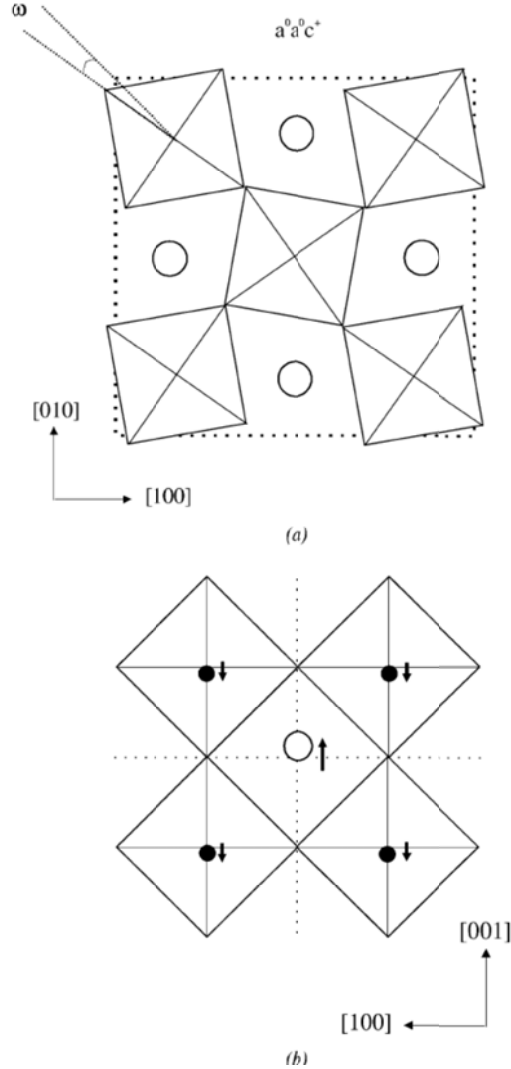


Figure 2.12 The antiparallel cation displacements in the *P4bm* structure with $a^0 a^0 c^+$ oxygen octahedra tilting.²⁷ The open circles represent A-site cations ($\text{Bi}^{3+}/\text{Na}^+$), while filled circles represent B-site cations (Ti^{4+}).

The electric properties of BNT show interesting decoupling from the structural phase transitions with regard to transition temperatures.²¹ Pure BNT is ferroelectric up to 200 °C. Between 200 and 320 °C, pinched P vs E hysteresis loop with a non-zero P_r and E_C was

observed. These characterize a ferrielectric behavior. However, since P_r is small, the phase in this temperature region is more commonly referred to as antiferroelectric.^{4,21,23} Above 320 °C BNT is paraelectric. In the paraelectric regime, there is a ferroelastic-paraelectric transition at ~520 °C. Although the sequence of the appearance of different electric behaviors seems to match that of the structure evolution, the transition temperatures do not show apparent correlation. The reason for such a structure-property decoupling has not been conclusively interpreted in literature.

2.4.2 Reported phase diagram

The first phase diagram of (1-x)BNT-xBT was reported by Takenaka et. al. in 1991 (Fig. 2.13).²³ The room-temperature crystal structures were obtained by x-ray diffraction, while the transition temperatures were derived from the dielectric curves. Thus Fig. 2.13 is actually a dielectric phase diagram overlapped with the room-temperature structural phase diagram. Compared with the phase transitions of pure BNT described in the last section, it is apparent that the rhombohedral ferroelectric phase in the low-BT-content compositions, the antiferroelectric phase in the intermediate temperature range, and the high-temperature paraelectric phase are inherited from pure BNT. With increasing BT content, the antiferroelectric phase is more and more stabilized, as reflected by the lowering of the ferroelectric-to-antiferroelectric transition temperature. At compositions around $x = 6\%$, the

antiferroelectric phase is most stabilized, and simultaneously a tetragonal ferroelectric phase emerges, forming an MPB with the rhombohedral $R3c$ ferroelectric phase. Further increase in the BT content leads to the stabilization of this $P4mm$ phase, which is reflected by the increase of the ferroelectric-to-antiferroelectric transition temperature. As the composition x varies between 0 and 30%, the antiferroelectric-to-paraelectric transition temperature only shows weak dependence on the composition.

Similar to $\text{Pb}(\text{Zr},\text{Ti})\text{O}_3$, optimal piezoelectric properties were observed at the MPB separating rhombohedral and tetragonal ferroelectric phases ($x \sim 6\%$).^{23,24,30} However, in contrast to $\text{Pb}(\text{Zr},\text{Ti})\text{O}_3$, the MPB in BNT-BT is highly curved, and for most compositions both ferroelectricity and piezoelectricity vanish prior to reaching the high-temperature paraelectric phase region due to the ferroelectric-to-antiferroelectric transition. Because the presence of the antiferroelectric phase diminishes the polarization, the ferroelectric-to-antiferroelectric transition temperature, which is determined by a hump in the temperature dependence curve of loss tangent, is referred to as the depolarization temperature T_d .^{23,30} At higher temperatures, the antiferroelectric-to-paraelectric transition leaves a broad peak of permittivity in the ε_r vs T curve. This transition temperature, referred to as T_m , is determined from the temperature where the permittivity reaches its maximum value.^{23,30}

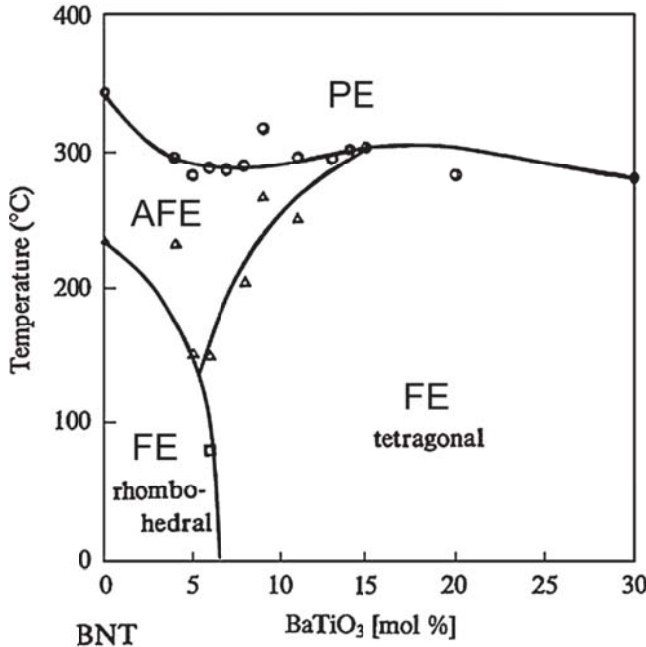


Figure 2.13 Phase diagram of BNT-BT reported by Takenaka et. al. at 1991.^{21,23} FE, AFE, and PE stand for ferroelectric, antiferroelectric, and paraelectric, respectively.

Although much work has been done following this phase diagram,⁴ several issues are still far from clear. First of all, the physical nature of the antiferroelectric phase in Fig. 2.13 is under debate. It was originally claimed as an antiferroelectric because of the observation of the pinched polarization hysteresis loop.²³ However, the recently observed nanodomains without any large ferroelectric domains, as well as the almost linear elastic behavior, rather indicate a relaxor ferroelectric behavior.²⁹ Second, the determination of T_d is doubtful. In the phase diagram in Fig. 2.13 and the work following it, T_d was determined from the hump in the temperature dependence curve of loss tangent.^{23,30,32,33} Nevertheless, this hump does not exist for the as-sintered ceramics with compositions around the $x = 6\%$ MPB.^{32,33} In

this case, electrical poling was performed before the dielectric measurement so that the hump emerges.^{32,33} T_d was then determined from these poled ceramics.^{32,33} This alternative method is highly questionable: the intensive electric field during poling causes a phase transition, which is irreversible even after removing the field.³⁴ Thus the phase diagram of the as-sintered ceramics must be different from the ones obtained through this approach from poled ceramics.^{23,33} Unfortunately this phase diagram has not been reported in literature.

2.4.3 Structure-property relationship

The structure-property relationship of (1- x)BNT- x BT may be discussed in two aspects: the relationship against temperature, and that against composition (at room temperature). The structure-property relationship against temperature needs to be traced back to the base compound BNT. As mentioned in section 2.4.1, the structural and dielectric transition temperatures do not show apparent correlation for BNT, and the reason is still unknown. The (1- x)BNT- x BT solid solutions with composition in the vicinity of the $x \sim 6\%$ MPB inherit most structural and dielectric transitions from pure BNT.^{21,23,27} As a result, it is likely that the unexplained structure-property decoupling in BNT is also present in these compositions. Although the complete scenario of the structure-property relationship in BNT-BT solid solutions has not been conclusively determined due to the lack of temperature-dependent structural study, recently there has been a work probing the

correlation between the structural and dielectric transition temperatures.³⁵ Without revealing the detailed crystal structure evolution with temperature, the structural transition temperatures are determined from anelastic anomalies. On one hand, the combined anelastic and dielectric analysis indicates that for compositions around $x = 6\%$ a structural phase transition occurs right at the depolarization temperature T_d , where the room-temperature ferroelectric phase transforms to the antiferroelectric phase. By comparing the phase transitions in pure BNT, this may very likely suggest the *R3c*-to-*P4bm* transition correlates with the ferroelectric-to-antiferroelectric transition at T_d . On the other hand, it is observed that with increasing x the *P4bm*-to-*Pm* $\overline{3}m$ transition temperature drops toward T_m , and these two transition temperatures are converging in $x = 5\%$. However, the anelastic anomaly associated with the *P4bm*-to-*Pm* $\overline{3}m$ transition becomes extremely broadened for $x > 5\%$, preventing the accurate determination of the structural transition temperature. As a result, whether the *P4bm*-to-*Pm* $\overline{3}m$ transition temperature merges with T_m for $x > 5\%$ remains an open question.

The room-temperature structure-property relationship against composition also deserves more detailed study. The issues that are not very well understood lie in the compositions in the vicinity of the $x \sim 6\%$ MPB. Although the crystal structure of the poled ceramics with these compositions is clearly tetragonal,^{33,34} the unpoled ones can only be described as pseudocubic,³⁴ because the distortion from the prototype cubic perovskite

structure is beyond the detectable limit of x-ray diffraction. The possibility of rhombohedral, tetragonal, or even a third structure cannot be excluded. Furthermore, the physical nature of this pseudocubic phase in the unpoled ceramics is unclear. The *in-situ* x-ray diffraction on the $x = 7\%$ composition has demonstrated that the pseudocubic phase will be forced into a tetragonal ferroelectric phase by the externally applied electric field.³⁴ Based on the electric polarization and strain analysis, an electric-field-induced antiferroelectric-to-ferroelectric transition was observed in the $x = 6\%$ composition doped with minor amount of $(K_{0.5}Na_{0.5})NbO_3$ (< 3 mol%). The antiferroelectric phase present in the virgin state of the $(K_{0.5}Na_{0.5})NbO_3$ -modified BNT-BT also exhibits pseudocubic structure and behaves similarly to the intermediate-temperature antiferroelectric phase in BNT-BT solid solutions in many aspects, such as the dielectric frequency dispersion and the magnitude of strain associated with the electric-field-induced phase transition, etc..^{22,31,36,37} It is possible that these two electric-field-induced transitions actually cross the same phase boundary. In another word, the room-temperature pseudocubic phase in the unpoled $(1-x)BNT-xBT$ ceramics with $x \sim 6\%$, the antiferroelectric phase observed in the virgin state of $(K_{0.5}Na_{0.5})NbO_3$ -modified BNT-BT, and the intermediate-temperature antiferroelectric phase in BNT-BT may probably be the same phase. However, this has not been verified experimentally. Besides, the physical nature of the intermediate-temperature antiferroelectric phase in BNT-BT is not conclusively determined either (section 2.4.2.).

2.4.4 Ferroelectric domain structure

As the fundamental microstructural units in ferroelectric materials, ferroelectric domains dictate the dielectric, ferroelectric, and piezoelectric behaviors.^{2,3} In addition to the crystal structure analysis and electric property measurements, the study of domain morphology is certainly critical in resolving the unexplained issues mentioned above. However, such study is currently very rare in the literature, and many of them show inconsistent results.^{22,29,38-45} For the rhombohedral phase region in the reported phase diagram (Fig. 2.13),²³ it was observed that the pure BNT exhibits nanometer-sized platelets with tetragonal symmetry in the rhombohedral matrix at room temperature. In addition, a one-dimensional modulated texture was observed.³⁸⁻⁴⁰ However, it was claimed that no signs of domain exist in the single crystal with the composition $x = 3\%$,⁴¹ which also belongs to the rhombohedral phase region according to Fig. 2.13.²³ For the tetragonal phase region (Fig. 2.13),²³ the lamellar ferroelectric domains were observed in the single crystal with the composition $x = 8\%$,⁴² while the crystal with the same composition has also been reported to exhibit no domains.⁴¹ For the region close to the $x \sim 6\%$ MPB that displays pseudocubic symmetry in the unpoled state,³⁴ nanodomains of oxygen octahedra tilting were visualized using the centered-dark-field imaging technique in BNT-BT ceramics doped with minor amount of $(Bi_{1/2}K_{1/2})TiO_3$ and $(Bi_{1/2}Li_{1/2})TiO_3$.^{43,44} In contrast, large lamellar domains were observed in $(K_{0.5}Na_{0.5})NbO_3$ -modified 94% BNT-6% BT ceramics, which also exhibit

macroscopic pseudocubic symmetry.²⁹ These previous studies on scattered compositions can hardly lead to a conclusive picture about the domain structure in BNT-BT solid solutions.

References

- ¹ R. E. Newnham, *Properties of Materials: Anisotropy, Symmetry, Structure* (Oxford University Press, New York, 2005).
- ² B. Jaffe, W. R. Cook, and H. Jaffe, *Piezoelectric Ceramics* (Academic Press, London, 1971).
- ³ G. H. Haertling, *J. Am. Ceram. Soc.* **82**, 797 (1999).
- ⁴ J. Rödel, W. Jo, K. Seifert, E. M. Anton, T. Granzow, and D. Damjanovic, *J. Am. Ceram. Soc.* **92**, 1153 (2009).
- ⁵ A. M. Glazer, *Acta Cryst.* **A31**, 756 (1975).
- ⁶ H. Hu, H. M. Chan, X. W. Zhang, and M. P. Harmer, *J. Am. Ceram. Soc.* **69**, 594 (1986).
- ⁷ A. A. Bokov and Z.-G. Ye, *J. Mater. Sci.* **41**, 31 (2006).
- ⁸ L. E. Cross, *Ferroelectrics* **76**, 241 (1987).
- ⁹ X. Zhao, W. Qu, X. Tan, A. A. Bokov, and Z.-G. Ye, *Phys. Rev. B* **75**, 104106 (2007).
- ¹⁰ G. A. Smolenskii, *J. Phys. Soc. Jpn.* **28** (Supl.), 26 (1970).
- ¹¹ D. A. Hall, *J. Mater. Sci.* **36**, 4575 (2001).
- ¹² D. Damjanovic, *J. Am. Ceram. Soc.* **88**, 2663 (2005).

- ¹³ N. Bassiri-Gharb, I. Fujii, E. Hong, S. Trolier-McKinstry, D. V. Taylor, and D. Damjanovic, *J. Electroceram.* **19**, 47 (2007).
- ¹⁴ J.-F. Chou, M.-H. Lin, and H.-Y. Lu, *Acta Mater.* **48**, 3569 (2000).
- ¹⁵ M. Ahart, M. Somayazulu, R. E. Cohen, P. Ganesh, P. Dera, H.-K. Mao, R. J. Hemley, Y. Ren, P. Liermann, and Z. Wu, *Nature* **451**, 545 (2008).
- ¹⁶ R. J. Zeches, M. D. Rossell, J. X. Zhang, A. J. Hatt, Q. He, C.-H. Yang, A. Kumar, C. H. Wang, A. Melville, C. Adamo, G. Sheng, Y.-H. Chu, J. F. Ihlefeld, R. Erni, C. Ederer, V. Gopalan, L. Q. Chen, D. G. Schlom, N. A. Spaldin, L. W. Martin, and R. Ramesh, *Science* **326**, 977 (2009).
- ¹⁷ B. Noheda, D. E. Cox, G. Shirane, J. A. Gonzalo, L. E. Cross, and S.-E. Park, *Appl. Phys. Lett.* **74**, 2059 (1999).
- ¹⁸ R. Guo, L. E. Cross, S.-E. Park, B. Noheda, D. E. Cox, and G. Shirane, *Phys. Rev. Lett.* **84**, 5423 (2000).
- ¹⁹ K. A. Schonau, L. A. Schmitt, M. Knapp, H. Fuess, R.-A. Eichel, H. Kungl, and M. J. Hoffmann, *Phys. Rev. B* **75**, 184117 (2007).
- ²⁰ A. M. Glazer, P. A. Thomas, K. Z. Baba-Kishi, G. K. H. Pang, and C. W. Tai, *Phys. Rev. B* **70**, 184123 (2004).
- ²¹ X. Tan, C. Ma, J. Frederick, S. Beckman, and K. G. Webber, *J. Am. Ceram. Soc.* **94**, 4091 (2011).
- ²² S.-T. Zhang, A. B. Kounga, E. Aulbach, T. Granzow, W. Jo, H.-J. Kleebe, and J. Rödel, *J. Appl. Phys.* **103**, 034107 (2008).
- ²³ T. Takenaka, K. Maruyama, and K. Sakata, *Jpn. J. Appl. Phys., Part 1* **30**, 2236 (1991).

- ²⁴ W. Jo, J. E. Daniels, J. L. Jones, X. Tan, P. A. Thomas, D. Damjanovic, and J. Rödel, *J. Appl. Phys.* **109**, 014110 (2011).
- ²⁵ S.-T Zhang, A.B. Kounga, E. Aulbach, H. Ehrenberg, and J. Rödel, *Appl. Phys. Lett.* **91**, 112906 (2007).
- ²⁶ G. A. Smolenskii, V. A. Isupov, A. I. Agranovskaya, and N. N. Krainik, *Sov. Phys. - Solid State* **2**, 2651 (1961).
- ²⁷ G. O. Jones and P. A. Thomas, *Acta Cryst. B* **58**, 168 (2002).
- ²⁸ G. A. Smolenskii, *Ferroelectric and Related Materials* (Gorden and Breach, New York, 1984).
- ²⁹ X. Tan, E. Aulbach, W. Jo, T. Granzow, J. Kling, M. Marsilius, H. J. Kleebe, and J. Rödel, *J. Appl. Phys.* **106**, 044107 (2009).
- ³⁰ C. Xu, D. Lin, and K. W. Kwok, *Solid State Sci.* **10**, 934 (2008).
- ³¹ W. Jo, T. Granzow, E. Aulbach, J. Rödel, and D. Damjanovic, *J. Appl. Phys.* **105**, 094102 (2009).
- ³² Y. Hiruma, H. Nagata, and T. Takenaka, *J. Appl. Phys.* **104**, 124106 (2008).
- ³³ Y. Hiruma, Y. Watanabe, H. Nagata, and T. Takenaka, *Key Eng. Mater.* **350**, 93 (2007).
- ³⁴ J. E. Daniels, W. Jo, J. Rödel, and J. L. Jones, *Appl. Phys. Lett.* **95**, 032904 (2009).
- ³⁵ F. Cordero, F. Craciun, F. Trequattrini, E. Mercadelli, and C. Galassi, *Phys. Rev. B* **81**, 144124 (2010).
- ³⁶ S.-T. Zhang, A. B. Kounga, E. Aulbach, W. Jo, T. Granzow, H. Ehrenberg, and J. Rödel, *J. Appl. Phys.* **103**, 034108 (2008).
- ³⁷ S.-T. Zhang, A. B. Kounga, E. Aulbach, and Y. Deng, *J. Am. Ceram. Soc.* **91**, 3950 (2008).

- ³⁸ V. Dorcet, G. Trolliard, and P. Boullay, *Chem. Mater.* **20**, 5061 (2008).
- ³⁹ V. Dorcet and G. Trolliard, *Acta Mater.* **56** (8), 1753 (2008).
- ⁴⁰ G. Trolliard and V. Dorcet, *Chem. Mater.* **20**, 5074 (2008).
- ⁴¹ A. N. Soukhojak, H. Wang, G. W. Farrey, and Y. M. Chiang, *J. Phys. and Chem. Solids* **61**, 301 (2000).
- ⁴² L. Liu, M. Zhu, Y. Hou, H. Yan, and R. Liu, *J. Mater. Res.* **22**, 1188 (2007).
- ⁴³ C. W. Tai, S. H. Choy, and H. L. W. Chan, *J. Am. Ceram. Soc.* **91**, 3335 (2008).
- ⁴⁴ C. W. Tai and Y. Lereah, *Appl. Phys. Lett.* **95**, 062901 (2009).
- ⁴⁵ J. Kling, X. Tan, W. Jo, H. J. Kleebe, H. Fuess, and J. Rödel, *J. Am. Ceram. Soc.* **93**, 2452 (2010).

CHAPTER 3. Experiment Details

3.1 Polycrystalline ceramic preparation

(1-x)(Bi_{1/2}Na_{1/2})TiO₃-xBaTiO₃ [(1-x)BNT-xBT] polycrystalline ceramics are prepared via a conventional solid state reaction approach. Powders of Bi₂O₃ (\geq 99.9%), Na₂CO₃ (\geq 99.9%), BaCO₃ (\geq 99.99%), TiO₂ (\geq 99.99%) are used as starting materials. Stoichiometric amount of powders are mixed and vibratory milled in ethanol with zirconia milling media for 7 hours and then dried. The Na₂CO₃ powders are baked at 200 °C for 15 hours and then weighed immediately to ensure stoichiometry. The mixture is calcined at 800 °C for 2 hours and then vibratory milled in ethanol with zirconia milling media for another 16 hours. After drying, the powders are evenly mixed with binder (10 wt% polyvinyl alcohol solution) and then uniaxially pressed into pellets. For the ceramics used in the electric-field *in-situ* TEM study, a cold isostatic pressing is performed after the uniaxial pressing to improve the quality of the green body. Following binder burnout at 500 °C, sintering is carried out at 1150 °C for 5 hours to obtain dense ceramic pellets. In order to prevent the loss of Bi³⁺ and Na⁺, the pellets are buried in a plenty amount of protective powder with the same composition during sintering. The relative density of the sintered pellets is higher than 95% as determined by the Archimedes' method. Scanning electron microscopy is used to further confirm the relative density and examine the grain size. The x-ray diffraction experiments

(PANalytical X'pert PRO MPD x-ray diffractometer, monochromatic Cu $K\alpha$ radiation, step scanning mode with increments of 0.05°) on as-sintered ceramics indicate pure perovskite phases in all compositions.

3.2 Dielectric/ferroelectric/piezoelectric characterization

Both sides of the sintered ceramic pellets are polished and made parallel prior to electrical measurements. Fired-on silver paste (Dupont 6160) is applied as electrodes. Dielectric permittivity and loss tangent under weak electric field above room temperature are measured with an LCR meter (HP-4284A, Hewlett-Packard) in conjunction with a tube furnace during heating at a rate of $3\text{ }^\circ\text{C}/\text{min}$. The dielectric characterization below room temperature is performed on a Novocontrol dielectric spectrometer in the step scanning mode with an increment of $5\text{ }^\circ\text{C}$ during heating. The polarization vs electric field hysteresis loop measurement is performed at room temperature with a frequency of 4 Hz using a standardized ferroelectric test system (RT-66A, Radian Technologies). The piezoelectric coefficient d_{33} of poled $(1-x)\text{BNT}-x\text{BT}$ ceramics is measured with a piezo- d_{33} meter. The ceramic samples are poled in silicon oil at room temperature under a series of fields ranging from 15 to 65 kV/cm with increasing sequence of field levels. At each field level the ceramic is poled for 20 minutes and subsequently aged for 24 hours at room temperature. Then the d_{33} value is measured ten times across the electrode surface.

3.3 Transmission electron microscopy (TEM) study

As-sintered ceramic pellets are mechanically ground and polished down to about 150 μm for TEM specimen preparation. Disks with diameter of 3 mm are ultrasonically cut from the polished slices and the central portion is further thinned to $\sim 5 \mu\text{m}$ by mechanical dimpling. The dimpled disks are annealed at 250 °C for 2 hours to minimize the residual stresses before Ar-ion mill to perforation. Specimens obtained through this approach are ready for the conventional and hot-stage TEM studies, which are performed using the conventional and hot-stage double-tilt specimen holder, respectively.

For electric-field *in-situ* TEM study, further treatment of the specimen is required, and a specially designed electric-field *in-situ* TEM specimen holder needs to be used. The experiment configuration is schematically illustrated in Fig. 3.1. Two half-circle shaped gold electrodes separated by 120 μm are evaporated onto the flat side of the perforated TEM specimen [Fig. 3.1(a)]. With the help of one droplet of insulating varnish, the specimen is fixed to the sample cup in such a way that the electrodes face up and the spacing between two electrodes is parallel to the rod of the specimen holder. Platinum wires and conductive epoxy are used to connect the electrodes of the specimen with the electrical contacts on the TEM holder tip, which are further connected to the external high-voltage power supply [Fig. 3.1(b) and (c)]. It should be noted that the circular shape of the central perforation disturbs

the electric field. As a result, only the field in the two small shaded areas at the edge of the central perforation in Fig. 3.1(a) preserves the direction of the nominal field, while the magnitude of the electric field in these two areas is about twice of the nominal value. All of the electric-field *in-situ* TEM observations in the present study are performed in the grains within these two areas. Because of the same electric field intensification phenomenon, the specimen used in such study must be crack-free. Otherwise significantly intensified electric field will be present in the crack tip, and thus no field exists in the shaded areas in Fig. 3.1(a), preventing the proper *in-situ* observation.

The conventional, hot-stage, and electric-field *in-situ* TEM studies are performed on a Phillips CM-30 microscope operated at 300 kV. Bright-field images, centered-dark-field images, and selected area electron diffraction patterns are recorded with a charge-coupled device camera. For each TEM study, multiple TEM experiments are conducted to make sure the observed microstructures and their evolution represent the behaviors of the entire sample.

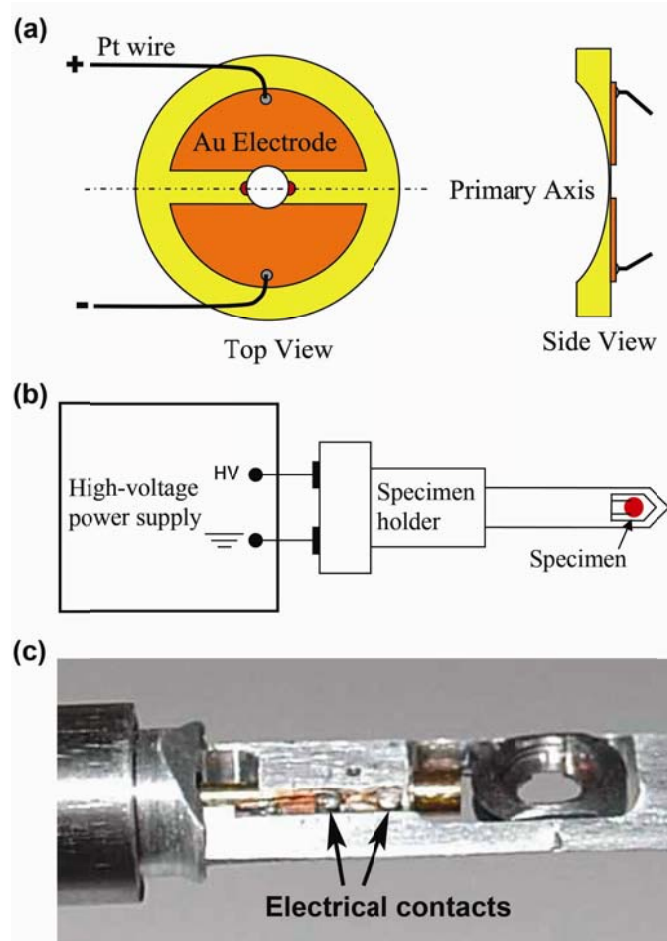


Figure 3.1 (a) The specimen configuration for the electric-field *in-situ* TEM experiment. (b) The connection of the high-voltage power supply to the TEM specimen. (c) Photograph of the tip of the electric-field *in-situ* TEM specimen holder used in the present study. The Pt thin wires in (a) are connected to the two electrical contacts indicated by the dark arrows.

CHAPTER 4. Domain Structure-Dielectric Property Relationship in Lead-Free $(1-x)(\text{Bi}_{1/2}\text{Na}_{1/2})\text{TiO}_3\text{-}x\text{BaTiO}_3$ Ceramics

A paper published in *Journal of Applied Physics* **108**, 104105 (2010)

Cheng Ma, Xiaoli Tan, Evgeniy Dul'kin, and Michael Roth

Abstract

The domain morphology and crystal structure of $(1-x)(\text{Bi}_{1/2}\text{Na}_{1/2})\text{TiO}_3\text{-}x\text{BaTiO}_3$ lead-free piezoelectric ceramics were systematically studied with transmission electron microscopy (TEM) for compositions $x = 0.04$ through 0.11 . It was found that the ceramics with compositions $x < 0.06$ display a $R3c$ symmetry with ferroelectric domains of ~ 100 nm forming complex structures at room temperature. Only nanodomains with faint contrast were observed in the compositions of $0.07 \leq x \leq 0.09$. The presence of weak $\frac{1}{2}(oe)$ superlattice diffraction spots and absence of $\frac{1}{2}(ooo)$ ones (o stands for odd and e stands for even miller indices) seem to suggest a $P4bm$ symmetry at room temperature. The morphotropic phase boundary (MPB) composition $x = 0.06$ showed mixed $R3c$ and $P4bm$ phases. Large lamellar ferroelectric domains with $P4mm$ symmetry were found to dominate in the ceramic of $x = 0.11$. The observed domain structure correlates extremely well with

the frequency dispersion of dielectric constant at room temperature and a new concept “relaxor antiferroelectric” was proposed to describe the dielectric behavior of compositions $0.07 \leq x \leq 0.09$. These results are summarized in a phase diagram for unpoled ceramics in the $(1-x)(\text{Bi}_{1/2}\text{Na}_{1/2})\text{TiO}_3-x\text{BaTiO}_3$ binary solid solution system.

4.1 Introduction

Piezoelectric materials are of technological importance because of their wide applications in transducers, actuators, and microelectronic devices.¹⁻³ Although lead-based perovskites such as $\text{Pb}(\text{Zr}_x\text{Ti}_{1-x})\text{O}_3$ (PZT) have been the material of first choice for the past five decades due to their excellent piezoelectric performance,^{1,2} the toxicity of lead raised serious environmental concerns and the restriction of use of lead in electronic devices has been implemented in environmental legislations in many countries.³ This has led to intensive worldwide efforts in the search for lead-free ferroelectric ceramics with good piezoelectric properties.

The $(\text{Bi}_{1/2}\text{Na}_{1/2})\text{TiO}_3-\text{BaTiO}_3$ (BNT-BT) solid solution is one of the most promising and extensively studied lead-free piezoelectric ceramics.³⁻⁷ The high piezoelectric coefficient and low free permittivity make it superior in high-frequency ultrasonic applications and piezoelectric actuators.⁴ The optimal piezoelectric property in $(1-x)\text{BNT}-x\text{BT}$ was found at

its morphotropic phase boundary (MPB) $x \sim 0.06$, which was believed to separate a rhombohedral ferroelectric phase isostructural with pure BNT ($R3c$) and a tetragonal ferroelectric one isostructural with BT ($P4mm$).⁴⁻⁶ The investigation of the ferroelectric domain morphology, crystal structure, and their correlation with electrical properties for the BNT-BT system is critical for the understanding of the origin of the electric field-induced strains in these lead-free piezoelectric ceramics. However, systematic studies on such issues are still missing in literature.

(1-x)BNT- x BT displays complex dielectric behaviors with strong frequency dispersion. When heated, the room-temperature ferroelectric phase transforms into an antiferroelectric one at the depolarization temperature T_d , and the antiferroelectric phase further changes to a paraelectric one at T_m .^{4,30} The dielectric constant, ε_r , peaks at the temperature T_m around 280 °C. The frequency dispersion in dielectric permittivity vanishes at temperatures several tens of degrees below T_m .^{4,30} In literature, T_d is determined from the hump of the temperature dependence curve of loss tangent. However, for many compositions, this hump does not exist in as-sintered unpoled samples. In this case, T_d is determined by the hump in the loss tangent curve in electrically poled samples.^{32,33} This alternative approach is highly questionable because it has been reported that the phase structure can be completely altered by the applied electric field during poling, and the change is not reversed after removing the field.³⁴ Thus the phase diagram for as-sintered ceramics in the virgin state must be different

from those determined using the electrically poled ceramics.^{4,33} Unfortunately this phase diagram has not yet been reported in literature.

The crystal structure of the antiferroelectric phase above T_d was assigned as pseudocubic previously based on X-ray diffraction,³² implying that the lattice distortion from the parent $Pm\bar{3}m$ cubic perovskite structure is below the detect limit of X-ray diffraction. Neutron diffraction of the base compound $(Bi_{1/2}Na_{1/2})TiO_3$ suggests that the antiferroelectric phase should take the $P4bm$ symmetry, with $a^0a^0c^+$ oxygen octahedron tilt and antiparallel displacements between A-site and B-site cations.¹¹ Phase diagrams of poled $(1-x)BNT-xBT$ ceramics show that T_d reaches a minimum at the MPB composition $x = 0.06$,^{4,33} indicating that the antiferroelectric phase is most stabilized at the MPB. Recent transmission electron microscopy (TEM) studies revealed that the antiferroelectric $P4bm$ phase is present even at room temperature in the form of nanometer-scale platelets embedded in the $R3c$ matrix in pure $(Bi_{1/2}Na_{1/2})TiO_3$.¹² Considering the fact that this antiferroelectric phase is more stabilized in the MPB compositions of $(1-x)BNT-xBT$ than in pure $(Bi_{1/2}Na_{1/2})TiO_3$ as mentioned above, it is highly likely that this $P4bm$ phase is prominent in the unpoled samples with MPB compositions at room temperature. Experimental evidences are needed to confirm this. On the other hand, the nature of this phase is still under debate.^{4,30,29} Although the pinched polarization hysteresis loop suggests an antiferroelectric (AFE) behavior,^{4,30} the presence of nanodomains without any large ferroelectric domains, and the

almost linear elastic behavior rather indicates a relaxor behavior.²⁹ The verification of the existence of the *P4bm* phase in unpoled samples at room-temperature and the determination of its nature are the first step toward understanding the origin of the high piezoelectric performance of BNT-BT.

Associated with the crystal structure and dielectric behavior is the ferroelectric domain morphology. However, domains and their evolution with composition around the MPB in (1-*x*)BNT-*x*BT has not been systematically investigated with TEM. Limited reports on individual compositions in literature show inconsistent results.¹²⁻²⁰ In the single crystals of 0.97BNT-0.03BT and 0.92BNT-0.08BT, it was claimed that no signs of domains exist.¹⁶ Recently nanodomains of oxygen octahedron tilt were imaged using the dark field technique in BNT-BT ceramics doped with K⁺ and Li⁺.^{17,18} However, we did observe large lamellar ferroelectric domains in a composition of 0.94BNT-0.05BT-0.01(K_{0.5}Na_{0.5})NbO₃.²⁹ These previous studies on scattered compositions can hardly lead to a consistent picture about the evolution of the domain morphology with compositions around the MPB in (1-*x*)BNT-*x*BT.

The present study is designed to sort these issues out with detailed TEM investigations on a series of compositions in the MPB region. Based on the results, a phase diagram for unpoled (1-*x*)BNT-*x*BT ceramics is constructed. In contrast to the previously reported phase diagrams,^{4,33} an additional phase region exhibiting *P4bm* symmetry and nanodomains

is revealed within $0.07 \leq x \leq 0.09$ at room temperature. The MPB at $x \sim 0.06$ with the best piezoelectric properties is shown to separate the $R3c$ and $P4bm$ phases rather than the $R3c$ and $P4mm$ phases.^{4,33} Combined with the dielectric study, a new concept “relaxor antiferroelectric” is proposed to describe the $P4bm$ phase with nanodomains.

4.2 Experimental procedure

Polycrystalline ceramic samples of $(1-x)$ BNT- x BT ($x = 0.04, 0.06, 0.07, 0.09, 0.11$) were prepared via a solid state reaction approach. Powders of Bi_2O_3 ($\geq 99.9\%$, nanopowder, Aldrich), Na_2CO_3 ($\geq 99.9\%$, Fisher), BaCO_3 ($\geq 99.99\%$, Alfa Aesar) and TiO_2 ($\geq 99.99\%$, Aldrich) were used as starting materials. Stoichiometric amount of powders were mixed and vibratory milled in ethanol with zirconia mill media for 7 hours and then dried. The Na_2CO_3 powder was baked at 200°C for 15 hours and then weighed immediately to ensure stoichiometry. The mixture was calcined at 800°C for 2 hours and then vibratory milled for another 16 hours. After drying, the powders were evenly mixed with binder (10 wt% polyvinyl alcohol solution) and then uniaxially pressed into pellets. Following binder burnout at 500°C , sintering was carried out at 1150°C for 5 hours to obtain dense ceramic pellets. In order to prevent the loss of Bi^{3+} and Na^+ , the pellets were buried in a plenty amount of protective powder with the same composition during sintering. The relative density of the sintered pellets is higher than 95% as determined by the Archimedes' method.

Scanning electron microscopy examination indicates that the grain size slightly decreases with increasing x . The average grain size is $\sim 3 \mu\text{m}$ for $x = 0.04$, and $\sim 2 \mu\text{m}$ for $x = 0.11$.

The X-ray diffraction experiments were carried out on a PANalytical X'pert PRO MPD X-ray diffractometer with monochromatic CuK α radiation in the step scanning mode with increments of 0.05° on as-sintered ceramic pellets. With the resolution of the instrument, the results indicated pure pervoskite phases in all ceramics. Then both sides of the pellets were polished and made parallel prior to electrical measurements. Silver paste (Dupont 6160) was fired on at 850°C for 6 minutes as electrodes. Dielectric constant and loss tangent under weak electric field above room temperature were measured with an LCR meter (HP-4284A, Hewlett-Packard) in conjugation with a tube furnace during heating at a rate of $3^\circ\text{C}/\text{min}$. The dielectric characterization below room temperature was performed on a Novocontrol dielectric spectrometer in the step scanning mode with an increment of 5°C during heating.

As-sintered pellets were mechanically ground and polished down to about $150 \mu\text{m}$ for TEM specimen preparation. Disks with diameter of 3 mm were ultrasonically cut from the polished slices and the center portion was further thinned to $\sim 5 \mu\text{m}$ by mechanical dimpling. The dimpled disks were annealed at 250°C for 2 hours to minimize the residual stresses

before Ar-ion mill to electron transparency. TEM studies were performed on a Phillips CM-30 microscope operated at 300 kV with a Gatan CCD camera installed.

4.3 Results

4.3.1 Dielectric characterization

The temperature dependences of the dielectric constant ε_r and loss tangent $\tan\delta$ for unpoled $(1-x)$ BNT- x BT ceramics are displayed in Fig. 4.1. The features of the curves and their variations with the composition are consistent with previous studies.⁴⁻⁷ The temperature T_m , which is defined as the temperature exhibiting maximum ε_r , shows a weak dependence on composition and is close to 280 °C for all compositions studied. The depolarization temperature T_d is determined by the temperature where the loss tangent shows a hump.^{32,33} A strong composition dependence of T_d is seen in Fig. 4.1. Compositions $x = 0.04$, 0.06 , and 0.11 show an apparent anomaly in their loss tangent curves and T_d can be easily determined. However, the change of loss tangent as a function of temperature is very gradual in unpoled $x = 0.07$ and 0.09 ceramics that T_d cannot be identified. It should be pointed out that T_d is not the temperature where a local maximum in ε_r appears. This is most evident in the ceramic $x = 0.06$ where T_d (114 °C) is found about 30 °C below the local maximum in ε_r . In addition to T_d , the frequency dispersion of ε_r and $\tan\delta$ also display

composition dependence. It does not appear until the temperature is above T_d for $x \leq 0.06$ and $x \geq 0.11$, but is present at room temperature and gets stronger with temperature increase for $0.07 \leq x \leq 0.09$. The significant frequency dispersion in the dielectric behavior seems to suggest relaxor characteristics. Unlike the classical relaxor ferroelectrics such as $\text{Pb}(\text{Mg}_{1/3}\text{Nb}_{2/3})\text{O}_3$ where frequency dispersion disappears at temperatures slightly above T_m ,²¹ the frequency dependence in (1-x)BNT-xBT ceramics vanishes at a temperature ~ 30 °C below T_m .

4.3.2 TEM study

Previous studies in literature suggest that only perovskite phases with $R3c$, $P4mm$, $P4bm$, and $Pm\bar{3}m$ symmetries need to be considered for (1-x)BNT-xBT ceramics at room temperature.^{32,33} The $R3c$ perovskite structure is characterized by the presence of $\frac{1}{2}(ooo)$ superlattice diffraction spots and the absence of $\frac{1}{2}(ooe)$ spots, while the $P4bm$ phase is accompanied by the $\frac{1}{2}(ooe)$ superlattice spots without $\frac{1}{2}(ooo)$ ones (o stands for odd and e stands for even miller indices).^{22,5} These superlattice diffractions are known to be extremely weak in X-ray diffraction. Therefore, selected area electron diffraction (SAED) in TEM offers unique advantages for structural analysis.

Figure 4.2 displays TEM micrographs and electron diffraction patterns from the same area in a grain with representative features for the composition $x = 0.04$. Ferroelectric

domains with sizes around 100 nm are seen when tilted to the [011], [111] and [$\bar{1}\bar{1}1$] zone axes, respectively. Figure 4.2(a) indicates that the domain walls are along {100} planes. Often times a stack of up to ten domains forms a colony and these colonies made up of differently oriented domains occupy the whole grain in a complex pattern. When tilted to [111] or [$\bar{1}\bar{1}1$] zone axis, {100} domain walls are inclined to the electron beam. As a result, no sharp contrast of domains is seen. This type of domain morphology does not resemble the previously studied systems including pure $(\text{Bi}_{1/2}\text{Na}_{1/2})\text{TiO}_3$.¹² We refer to this type of domain structure as “complex domain” hereafter. In spite of the different domain morphology, electron diffraction analysis indicates that the crystal structure of composition $x = 0.04$ is identical to that of $(\text{Bi}_{1/2}\text{Na}_{1/2})\text{TiO}_3$ at room temperature, which exhibits $R3c$ symmetry with the $a\bar{a}\bar{a}$ oxygen octahedron tilt.^{11,22,5} This is evidenced by the presence of strong $\frac{1}{2}(ooo)$ superlattice diffraction spots in SAED patterns of the [011] zone axis [see inset in Fig. 4.2(a)] and the absence of any superlattice spots in SAED patterns of the [111] or [$\bar{1}\bar{1}1$] zone axes.

The {100} domains with complex morphology that dominate the composition $x = 0.04$ transforms to nanodomains with increasing BaTiO_3 content. For the sample with $x = 0.06$, $\sim 40\%$ of the grains display a core-shell structure: the core exhibits the complex domains, while the shell consists of nanodomains with faint contrast. The rest of the grains consist of nanodomains only. Figure 4.3 shows the bright field micrographs and diffraction patterns

from the same area of a grain with the core-shell structure recorded along the [011] and [111] zone axes. The SAED pattern from the core exhibits $\frac{1}{2}(ooo)$ superlattice spots along the [011] zone axis and no superlattice spots along the [111] zone axis, confirming that the core has the same *R3c* symmetry as the composition $x = 0.04$. In contrast, the diffraction pattern from the shell with nanodomains in the same grain displays no superlattice spots along the [011] zone axis, while the $\frac{1}{2}(ooe)$ spots were observed along the [111] zone axis. This is characteristic of the *P4bm* symmetry with $a^0a^0c^+$ oxygen octahedron tilt.^{12,22} The presence of complex domains within limited volume and the dominating nanodomains seem to be consistent with the dielectric measurement results, which indicate that the antiferroelectric phase is stabilized as evidenced by the decrease in T_d from 162 °C in $x = 0.04$ to 114 °C in $x = 0.06$. The structural instability as evidenced by the coexistence of *R3c* core and *P4bm* shell in one grain is in direct support of the excellent piezoelectric properties observed previously in this composition.

For the as-sintered samples with $x = 0.07$ and 0.09 , only nanodomains were observed. The TEM results from representative grains in these two ceramics are shown in Figs. 4.4 and 4.5, respectively. The size of the nanodomains in $x = 0.07$ and 0.09 appears slightly larger than that in $x = 0.06$. In addition, tendency of texture can also be seen in both compositions when observed along the [011] zone axis. The electron diffraction patterns suggest the crystallographic structure of the nanodomains in these two compositions is identical to that of

the shell in the $x = 0.06$ composition: weak $\frac{1}{2}(ooe)$ spots were observed when the grain is tilted to its [111] zone axis and no superlattice spot was detected when tilted to the [011] zone axis. The absence of large domains at room temperature seems to be correlated to the absences of T_d in $x = 0.07$ and 0.09 within the temperature range for dielectric characterization shown in Fig. 4.1.

Further increase in BaTiO₃ content to $x = 0.11$ leads to a microstructure that is dominated by large lamellar ferroelectric domains. Around 20% of the grains contain a small volume occupied by nanodomains, while the rest exhibit lamellar domains only. Figure 4.6 shows the TEM results of a grain with both lamellar domains and nanodomains. Similar to the ceramics with $x = 0.06, 0.07$ and 0.09, the volume with nanodomains exhibits $P4bm$ symmetry as demonstrated by the presence of $\frac{1}{2}(ooe)$ spots and the absence of $\frac{1}{2}(ooo)$ spots. When viewed from the [111] zone axis, most lamellar domains are at edge-on position with sharp domain walls. Figures 4.6(d) and 4.6(f) indicate that the domain walls are on {101} planes. No superlattice spot was observed along either [011] or [111] zone axis from the volume with large lamellar domains, indicating no oxygen octahedron tilt is present. These are precisely the characteristic domain features of the $P4mm$ BaTiO₃.⁶ The coexistence of $P4bm$ nanodomains and $P4mm$ lamellar domains indicates that the composition $x = 0.11$ is the one across which the transition from the $P4bm$ to the $P4mm$ phase occurs with increasing x in unpoled (1- x)BNT- x BT ceramics.

4.4 Discussion

The evolution of the domain structure in the $(1-x)$ BNT- x BT ceramics demonstrates a clear correlation with the dielectric behavior from room temperature up to ~ 100 °C: nanodomains correspond to a strong frequency dispersion while regular ferroelectric domains show a weaker frequency dependence. Since the frequency dependence vanishes at ~ 30 °C below T_m in $(1-x)$ BNT- x BT, the dielectric constant above T_m cannot be used to evaluate the relaxation parameter and the diffuseness parameter which were used to characterize Pb-based relaxor ferroelectrics.²⁵ In order to quantify the frequency dispersion in the dielectric behavior, we define a parameter $\Delta\epsilon_r$ as

$$\Delta\epsilon_r = \epsilon_{r,1kHz} - \epsilon_{r,100kHz} \quad (1).$$

The frequency dispersion in the ceramics from room temperature up to ~ 100 °C can well be represented by $\Delta\epsilon_r$ at 50 °C. This value is plotted against composition x for $(1-x)$ BNT- x BT in Fig. 4.7(a). It is apparent that compositions $x = 0.07$ and 0.09 are outstanding for their large values of $\Delta\epsilon_r$. This is consistent with their short range order confined within nanodomains.

The frequency dispersion vanishes at a temperature well below T_m for all the compositions studied. However, to identify this relaxor transition temperature for all compositions studied here, the procedure for classical relaxor ferroelectrics, i.e. finding the

local maximum in frequency-dependent ε_r , cannot be followed since the frequency dispersion is cut off by T_d in $x = 0.04$, 0.06 , and 0.11 . The temperature for the local maximum in ε_r appears to be below T_d in $x = 0.04$ and 0.11 and hence cannot be revealed by the permittivity measurement. The significance of the parameter $\Delta\varepsilon_r$ is also manifested in offering an alternative way to locate this relaxor transition temperature in $(1-x)\text{BNT-}x\text{BT}$. It is interesting to notice that all the compositions tested display a local minimum in $\Delta\varepsilon_r$ right after the maximum. Figure 4.7(b) exemplifies the $\Delta\varepsilon_r$ vs. T plot for $x = 0.06$ and 0.07 . We define this unique temperature where $\Delta\varepsilon_r$ is a minimum as T_{RE} , the upper limit for the frequency dependent dielectric behavior. It is clear from Fig. 4.7(b) that a strong frequency dispersion occurs from room temperature up to T_{RE} for the composition $x = 0.07$, while from T_d up to T_{RE} for the composition $x = 0.06$. It should be pointed out that the temperature T_{RE} is unique for the dielectric behavior. It does not necessarily correspond to a structural phase transition.

The dielectric characterization above room temperature shown in Fig. 4.1 does not reveal T_d in compositions $x = 0.07$ and 0.09 . We speculated that T_d might be below room temperature for these two compositions. Figure 4.8 displays the temperature dependence of ε_r and $\tan\delta$ of $x = 0.07$ measured during heating from -140 °C to 100 °C. The dielectric behavior of $x = 0.09$ is more or less the same as that of $x = 0.07$ below room temperature. Neither of them displays any obvious anomaly that can be identified as T_d in the temperature

range studied, indicating the phase with the unique relaxor characteristics is still stable at least down to -140 °C in compositions $x = 0.07$ and 0.09 . However, it is noteworthy that the frequency dispersion is minimum at -140 °C and gradually strengthens as temperature increases. This again resembles the behavior of a relaxor ferroelectric, where the fluctuation of the randomly oriented nanodomains giving rise to the frequency dispersion is suppressed at low temperatures due to the lack of dynamics.^{7,8} Since the unique relaxor characteristics of $x = 0.07$ and 0.09 are also associated with nanodomains, the low-temperature frequency convergence of dielectric properties seems to suggest these characteristics arise from the dynamic fluctuation of nanodomains.

We have been using the term “relaxor” to describe the dielectric behavior between T_d and T_{RE} for $x = 0.04, 0.06$ and 0.11 (this behavior persists from -140 °C up to T_{RE} for $0.07 \leq x \leq 0.09$ as demonstrated in Fig. 4.1 and Fig. 4.8). However, $(1-x)\text{BNT-}x\text{BT}$ has also been historically described as “antiferroelectric” above T_d . Supporting evidences exist in literature for both terms.^{4,29} We propose a new term “relaxor antiferroelectric”, as oppose to “relaxor ferroelectric” represented by $\text{Pb}(\text{Mg}_{1/3}\text{Nb}_{2/3})\text{O}_3$,⁸ to reconcile the dispute. In the prototype relaxor ferroelectric compound $\text{Pb}(\text{Mg}_{1/2}\text{Nb}_{2/3})\text{O}_3$, the nanodomains are ferroelectric domains, implying that within the volume of individual nanodomains, all the electrical dipoles are parallel and aligned. Relaxor ferroelectric behavior is resulted from randomly oriented and dynamically fluctuating nanodomains.⁷ In the case of “relaxor

“antiferroelectric” as present in $(1-x)$ BNT- x BT, we suggest that the displacements of A-site cations (Bi^{3+} , Na^+ , Ba^{2+}) are antiparallel to the displacement of B-site cation (Ti^{4+}) within each individual nanodomain, i.e. the nanodomains are of antiferroelectric nature. This is supported by the fact that the nanodomained $x = 0.07$ and 0.09 display the $P4bm$ symmetry, which is identical to the antiferroelectric phase of the base compound $(\text{Bi}_{1/2}\text{Na}_{1/2})\text{TiO}_3$ existing between 255 and 540 °C with the displacement of $\text{Bi}^{3+}/\text{Na}^+$ antiparallel to that of Ti^{4+} and along the [001] direction.¹¹ However, the antiferroelectric ordering in $(1-x)$ BNT- x BT below T_{RE} is a short-ranged one confined within each individual nanodomains. Similar to the relaxor ferroelectric $\text{Pb}(\text{Mg}_{1/3}\text{Nb}_{2/3})\text{O}_3$ with polar vectors fluctuating among equivalent <111> directions,⁷⁻²⁹ the dynamic fluctuation of the cation displacements along the six equivalent <001> directions in $(1-x)$ BNT- x BT leads to the observed frequency dispersion in the dielectric behavior. In addition, as in relaxor ferroelectrics where ferroelectric nanodomains are embedded in a non-polar cubic matrix,⁷⁻²⁹ the antiferroelectric nanodomains in $(1-x)$ BNT- x BT are also suggested to be embedded in a matrix of undistorted cubic lattice. As a result, only very weak $\frac{1}{2}(ooe)$ superlattice spots characterizing the $P4bm$ phase are seen in electron diffraction patterns. A schematic diagram was presented in Fig. 4.9 to illustrate the concept of relaxor antiferroelectric nanodomains in $(1-x)$ BNT- x BT.

It has been speculated previously that the competition between long range antiferroelectric order and ferroelectric order results in the short-range order relaxor

behavior.³⁰ Following this speculation, adding ferroelectric BaTiO₃ to (Bi_{1/2}Na_{1/2})TiO₃ introduces the competition between the antiferroelectric *P4bm* and the ferroelectric *P4mm* phase. At compositions $0.07 \leq x \leq 0.09$, the frustration due to the competing long range order reaches a maximum and leads to a relaxor behavior persisting at room temperature. We expect that the long range antiferroelectric order will be enhanced at higher temperatures and the normal antiferroelectric behavior prevails over the competition. Therefore, the dielectric behavior in (1-*x*)BNT-*x*BT between *T_{RE}* and *T_m* can still be described as “antiferroelectric”. The different relaxor behaviors in (1-*x*)BNT-*x*BT and Pb(Mg_{1/2}Nb_{2/3})O₃ can be attributed to the displacements of different cations for electrical dipoles. In Pb(Mg_{1/2}Nb_{2/3})O₃, the displacement of A-site Pb²⁺ along <111> is the primary mechanism for electrical dipoles and the random fields due to disordered B-site cations Mg²⁺ and Nb⁵⁺ are responsible for the relaxor behavior.⁷⁻²⁹ In (1-*x*)BNT-*x*BT the situation seems to be reversed. The B-site cation Ti⁴⁺ is prone to shifting from the center of the oxygen octahedron,³¹ and the resulted dipole moment is balanced by the displacement of A-site cations along the opposite direction. Now the random fields come from the A-site disordered cations of Bi³⁺, Na⁺ and Ba²⁺. It should be noted that the dipole moment resulted from the Ti⁴⁺ displacement is not fully balanced by that from the A-site cation displacement, leading to a weakly polar ferrielectric order.¹¹

We would extend the clear correlation between nanodomains and frequency dispersion in compositions $x = 0.07$ and 0.09 to other compositions studied: Antiferroelectric nanodomains are anticipated between T_d and T_{RE} in ceramics of $x = 0.04, 0.06$ and 0.11 . At temperatures below T_d in these compositions, the room temperature domain structure (as revealed in Figs. 4.2, 4.3, and 4.6) will be more or less preserved. However, the fraction of volume with nanodomains is expected to increase as the ceramic is heated toward T_d . TEM experiments with a hot stage on the temperature-induced change of domain structure in these three compositions are currently underway to verify this.

The results obtained in this study are summarized in a new phase diagram for unpoled $(1-x)$ BNT- x BT ceramics displayed in Fig. 4.10. The symbols of solid triangles represent T_d , open circles for T_{RE} , and solid squares for T_m . The room-temperature composition dependence of the crystal structure and domain morphology is highlighted as shaded boxes. For compositions $x = 0.04, 0.06$, and 0.11 , the features for the room temperature domain morphology are expected to persist up to T_d and these fields are denoted as “FE” (stands for “ferroelectric”). For compositions $x = 0.07$ and 0.09 , the nanodomain morphology observed at room temperature is likely to be preserved until temperatures reach T_{RE} . A similar nanodomain morphology is speculated for the compositions $x = 0.04, 0.06$, and 0.11 between T_d and T_{RE} . This field with $P4bm$ nanodomains is denoted as “relaxor AFE” (stands for “relaxor antiferroelectric”) in the phase diagram. For all the compositions between T_{RE} and

T_m , a long range antiferroelectric order is speculated and is denoted as “AFE” (stands for “antiferroelectric”) in the phase diagram. “PE” in Fig. 4.10 marks the paraelectric phase above T_m .

Compared with the published phase diagrams determined using poled (1- x)BNT- x BT ceramics,^{4,33} the difference is obvious and yet significant. First of all, there are two composition-induced phase transitions at room temperature in unpoled ceramics within the composition range $x = 0.04 \sim 0.11$, instead of one in poled ceramics. With increase in x , the long range ferroelectric order ($R3c$) changes to a short range antiferroelectric order ($P4bm$) at around $x = 0.06$, and the relaxor antiferroelectric phase then transforms to a long range ferroelectric order with the $P4mm$ symmetry around $x = 0.11$. The MPB composition $x = 0.06$ previously identified from poled ceramics corresponds to a transition from a ferroelectric $R3c$ to a relaxor antiferroelectric $P4bm$ phase in unpoled ceramics. Secondly, a new phase transition temperature T_{RE} is defined and included. This transition is diffuse and frequency dependent and may not correspond to any structural symmetry change. The decoupling of dielectric response from the crystal structural phase transition has been noticed previously in the base compound $(\text{Bi}_{1/2}\text{Na}_{1/2})\text{TiO}_3$.^{4,30,11,14} Thirdly, a new “relaxor antiferroelectric” model is introduced to describe the broad phase region with antiferroelectric nanodomains. Under sufficient applied electric fields, two types of electric-field-induced phase transitions, i.e. the relaxor-to-ferroelectric and the

antiferroelectric-to-ferroelectric, can be expected during the poling process of unpoled ceramics of $x = 0.07$ and 0.09 at room temperature. From the previous phase diagrams for poled ceramics,^{4,33} a tetragonal ferroelectric phase should be resulted. Indeed recent *in situ* X-ray diffraction confirmed such phase transitions.³⁴ However, to visualize the evolution of the domain morphology during the phase transition, *in situ* TEM studies with applied electric fields are needed.^{20,32,33}

4.5 Conclusions

In summary, the composition dependence of domain morphology and crystal structure as well as their correlation with the dielectric behavior are investigated at room temperature in unpoled $(1-x)$ BNT- x BT ceramics around the MPB composition. It is found that, for $0.04 \leq x \leq 0.06$, the ceramics are characterized with $\{100\}$ ferroelectric domains with a length around 100 nm. These domains display the $R3c$ symmetry and form a complex pattern. For $0.06 \leq x \leq 0.11$, nanodomains with short range antiferroelectric order are observed. Electron diffraction suggests the $P4bm$ symmetry for these nanodomains. For $x \geq 0.11$, large lamellar $\{101\}$ domains with $P4mm$ structure are the dominant feature. The composition $x = 0.11$ and the previously determined MPB composition $x = 0.06$ both display a core-shell grain structure with mixed domain features. The observed domain morphology shows excellent correlation with the dielectric behavior: Regular ferroelectric domains

correspond to minimum frequency dispersions in dielectric permittivity while nanodomains lead to strong frequency dispersions.

A new critical temperature, T_{RE} , is defined based on the analysis of the dielectric behavior. Combined with the TEM results, a phase diagram for unpoled $(1-x)$ BNT- x BT ceramics to account for different dielectric phases is constructed. We propose that regular ferroelectric domains observed at room temperature will persist up to T_d . The nanodomains are believed to be disrupted antiferroelectric domains and are stable up to T_{RE} . The term “relaxor antiferroelectric” is coined to describe the phase region where the ceramic only contains $P4bm$ antiferroelectric nanodomains. Since the frequency dispersion in dielectric permittivity vanishes at T_{RE} , we suggest that a long range antiferroelectric order exists between T_{RE} and T_m .

Acknowledgements

This work was supported by the National Science Foundation (NSF) through Grant DMR-1037898 and the U.S.-Israel Binational Science Foundation through Grant No. 2006235. TEM experiments were performed at the Ames Laboratory which is operated for the U.S. Department of Energy by Iowa State University under Contract No. DE-AC02-07CH11358.

Figures

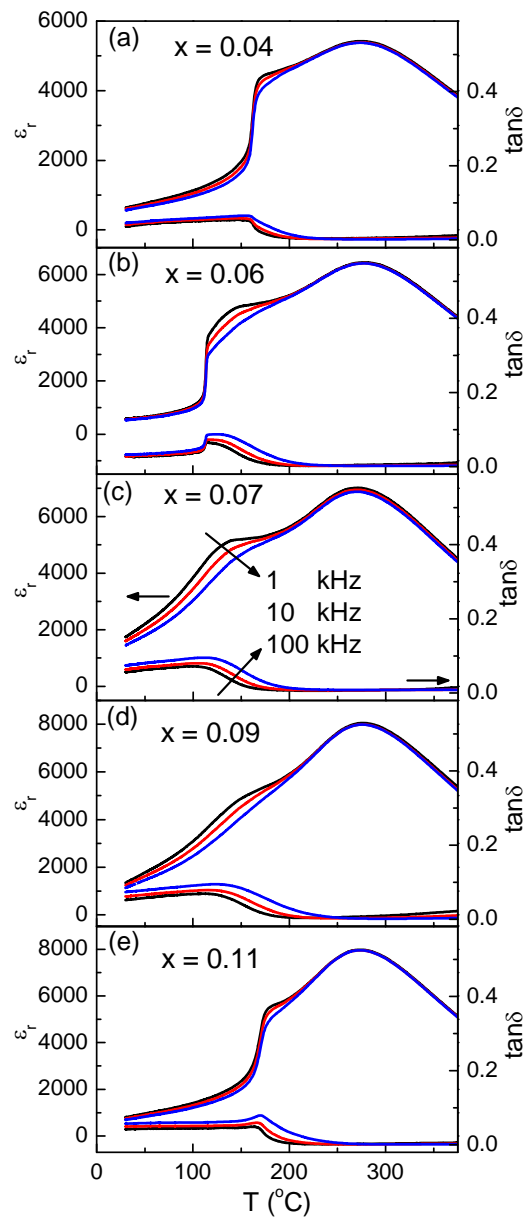


Figure 4.1 Temperature dependence of the dielectric constant ϵ_r and loss $\tan\delta$ for $x = 0.04, 0.06, 0.07, 0.09$ and 0.11 above room temperature measured during heating.

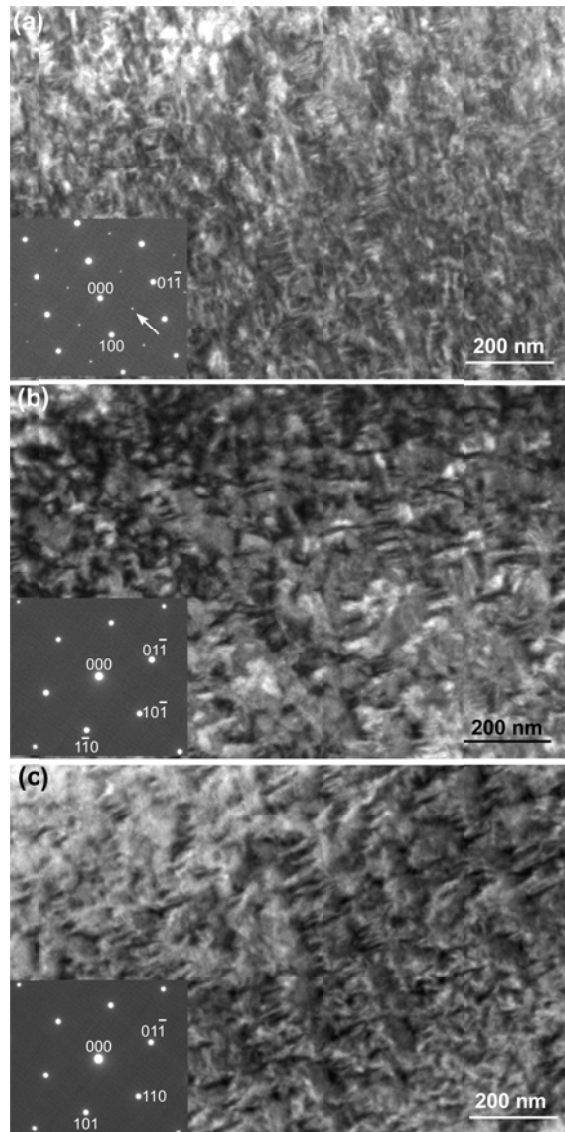


Figure 4.2 TEM bright field images of the same area in a representative grain for the composition $x = 0.04$ tilted to (a) [011] zone axis; (b) [111] zone axis; (c) [$\bar{1}11$] zone axis. The insets are the corresponding diffraction patterns.

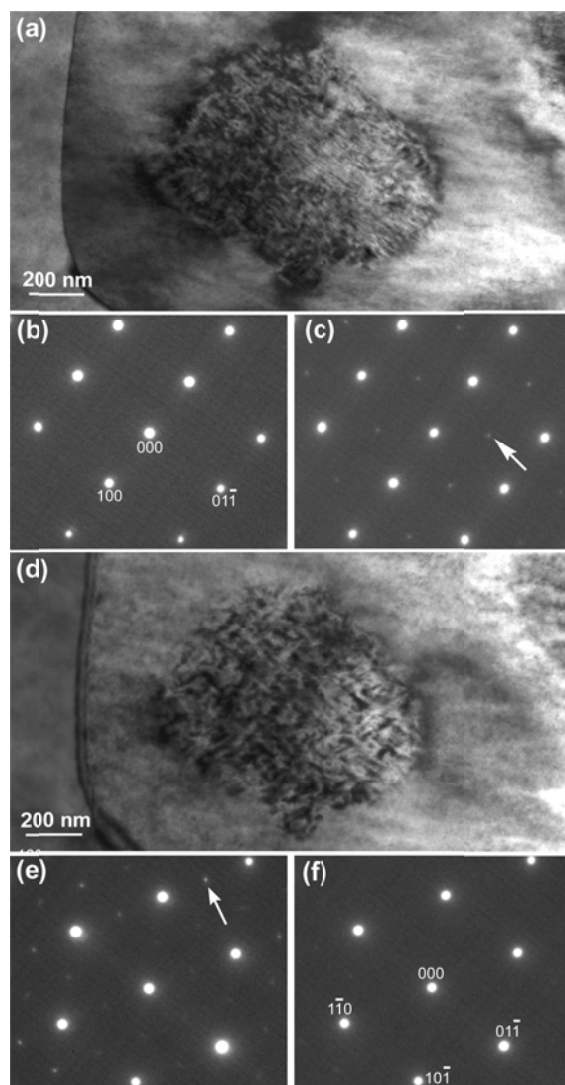


Figure 4.3 (a) TEM bright field image of a typical grain with core-shell structure for the composition $x = 0.06$ along its [011] zone axis; (b) diffraction pattern of nanodomains along [011] zone axis; (c) diffraction pattern of the complex domain along [011] zone axis; (d) TEM bright field image of the same grain in (a) tilted to its [111] zone axis; (e) diffraction pattern of nanodomains along [111] zone axis; (f) diffraction pattern of complex domains along [111] zone axis.

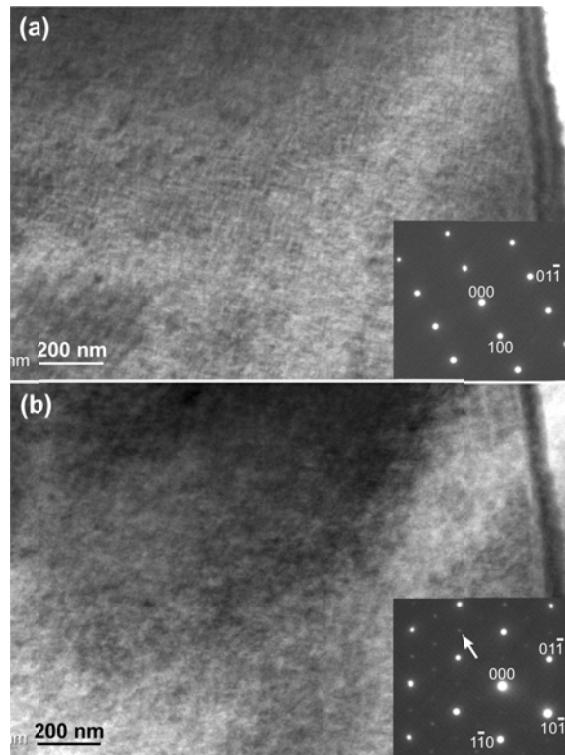


Figure 4.4 TEM bright field images of the same area in a representative grain for the composition $x = 0.07$ tilted to (a) [011] zone axis; (b) [111] zone axis. The insets are the corresponding diffraction patterns.

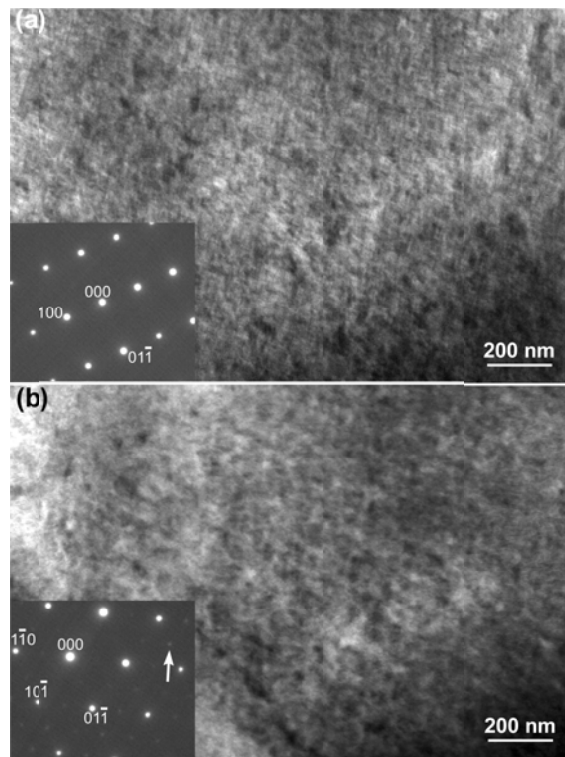


Figure 4.5 TEM bright field images of the same area in a representative grain for the composition $x = 0.09$ tilted to (a) [011] zone axis; (b) [111] zone axis. The insets are the corresponding diffraction patterns.

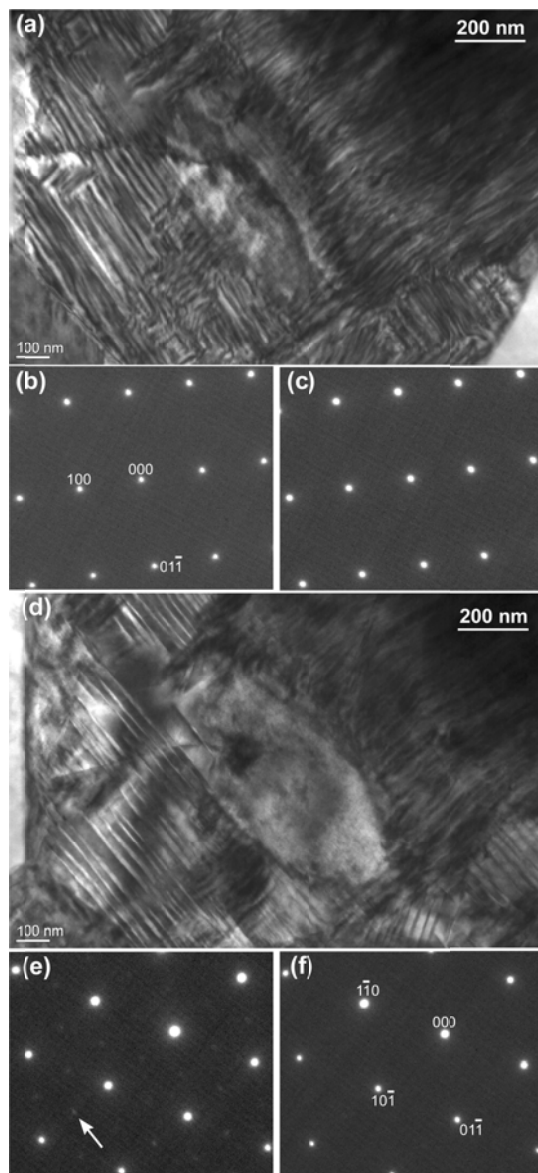


Figure 4.6 (a) TEM bright field image of a typical grain exhibiting both lamellar domains and nandomains for the composition $x = 0.11$ along its [011] zone axis; (b) diffraction pattern of nanodomains along [011] zone axis; (c) diffraction pattern of the lamellar domain along [011] zone axis; (d) TEM bright field image of the same grain in (a) tilted to its [111] zone axis; (e) diffraction pattern of nanodomains along [111] zone axis; (f) diffraction pattern of lamellar domains along [111] zone axis.

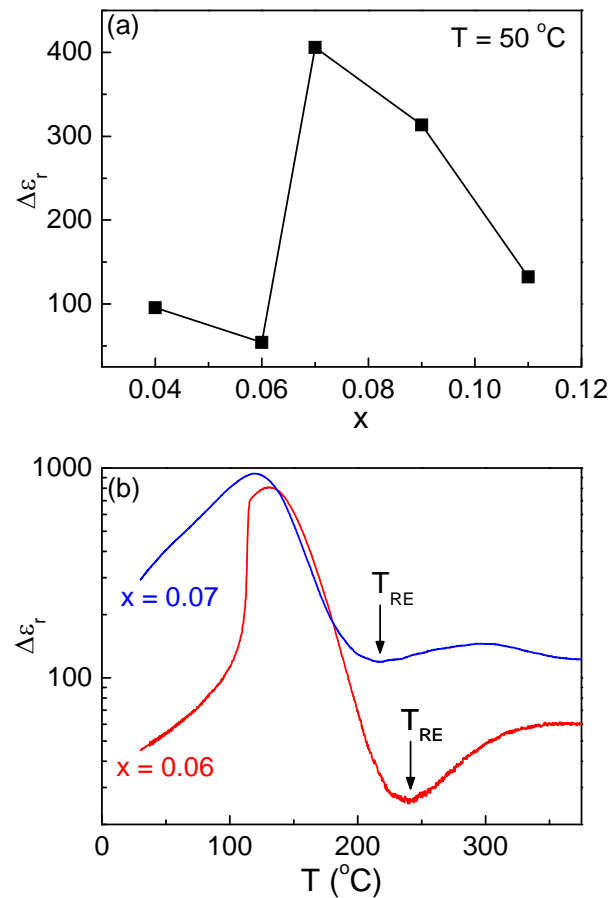


Figure 4.7 (a) The composition dependence of $\Delta\epsilon_r$ at 50°C ; (b) The temperature dependence of $\Delta\epsilon_r$ for $x = 0.06$ and 0.07 .

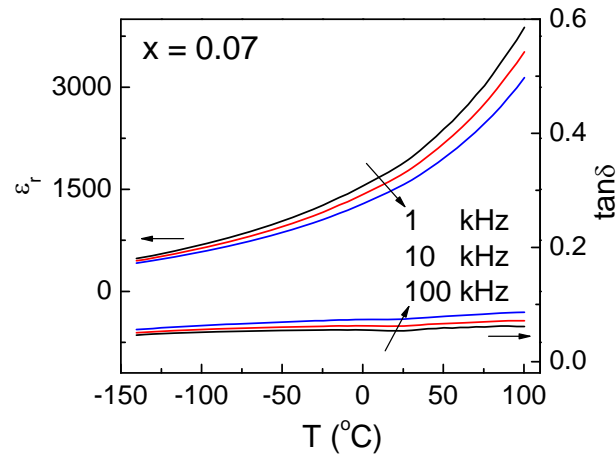


Figure 4.8 Temperature dependence of the dielectric constant ϵ_r and loss $\tan\delta$ for $x = 0.07$ from -140 $^{\circ}\text{C}$ to 100 $^{\circ}\text{C}$ measured during heating.

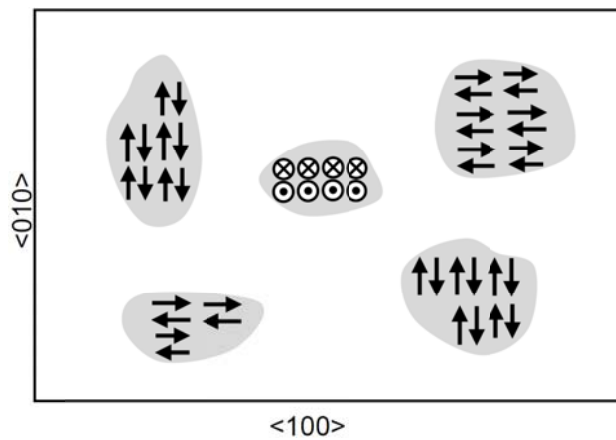


Figure 4.9 Schematic diagram of the nanodomains responsible for the observed “relaxor antiferroelectric” behavior in BNT-BT. These antiferroelectric nanodomains (the grey islands in the diagram) with the $P4bm$ symmetry are embedded in the undistorted cubic matrix (the white background in the diagram). The antiparallel arrow pairs denote the cation displacements which fluctuate among the six equivalent $\langle 001 \rangle_c$ directions.

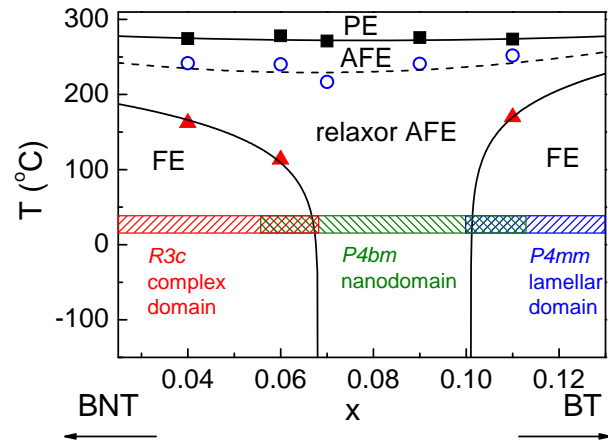


Figure 4.10 The phase diagram for unpoled $(1-x)$ BNT- x BT ceramics. The crystal structure and domain morphology at room temperature are highlighted as shaded boxes. Symbols of solid squares, open circles, and solid triangles represent T_m , T_{RE} , and T_d , respectively, determined from dielectric measurements. PE, AFE, and FE stand for paraelectric, antiferroelectric, and ferroelectric, respectively.

References

- ¹ B. Jaffe, W. R. Cook, and H. Jaffe, *Piezoelectric Ceramics* (Academic Press, London, 1971).
- ² G. H. Haertling, *J. Am. Ceram. Soc.* 82, 797 (1999).
- ³ J. Rödel, W. Jo, K. Seifert, E. M. Anton, T. Granzow, and D. Damjanovic, *J. Am. Ceram. Soc.* 92, 1153 (2009).
- ⁴ T. Takenaka, K. Maruyama, and K. Sakata, *Jpn. J. Appl. Phys.*, Part 1 30, 2236 (1991).
- ⁵ C. Xu, D. Lin, and K. W. Kwok, *Solid State Sci.* 10, 934 (2008).
- ⁶ M. Chen, Q. Xu, B. H. Kim, B. K. Ahn, J. H. Ko, W. J. Kang, and O. J. Nam, *J. Eur. Ceram. Soc.* 28, 843 (2008).
- ⁷ E. Dul'kin, E. Mojaev, M. Roth, S. Greicius, and T. Granzow, *Appl. Phys. Lett.* 92, 012904 (2008).
- ⁸ Y. Hiruma, H. Nagata, and T. Takenaka, *J. Appl. Phys.* 104, 124106 (2008).
- ⁹ Y. Hiruma, Y. Watanabe, H. Nagata, and T. Takenaka, *Key Eng. Mater.* 350, 93 (2007).
- ¹⁰ J. E. Daniels, W. Jo, J. Rödel, and J. L. Jones, *Appl. Phys. Lett.* 95, 032904 (2009).
- ¹¹ G. O. Jones and P. A. Thomas, *Acta Cryst. B* 58, 168 (2002).
- ¹² V. Dorcet and G. Trolliard, *Acta Mater.* 56 (8), 1753 (2008).
- ¹³ X. Tan, E. Aulbach, W. Jo, T. Granzow, J. Kling, M. Marsilius, H. J. Kleebe, and J. Rödel, *J. Appl. Phys.* 106, 044107 (2009).
- ¹⁴ V. Dorcet, G. Trolliard, and P. Boullay, *Chem. Mater.* 20, 5061 (2008).
- ¹⁵ G. Trolliard and V. Dorcet, *Chem. Mater.* 20, 5074 (2008).

- ¹⁶ A. N. Soukhojak, H. Wang, G. W. Farrey, and Y. M. Chiang, *J. Phys. and Chem. Solids* 61, 301 (2000).
- ¹⁷ C. W. Tai, S. H. Choy, and H. L. W. Chan, *J. Am. Ceram. Soc.* 91, 3335 (2008).
- ¹⁸ C. W. Tai and Y. Lereah, *Appl. Phys. Lett.* 95, 062901 (2009).
- ¹⁹ S. T. Zhang, A. B. Kounga, E. Aulbach, T. Granzow, W. Jo, H. J. Kleebe, and J. Rödel, *J. Appl. Phys.* 103, 034107 (2008).
- ²⁰ J. Kling, X. Tan, H. J. Kleebe, H. Fuess, W. Jo, and J. Rödel, *J. Am. Ceram. Soc.* 2010, in print.
- ²¹ X. Zhao, W. Qu, X. Tan, A. A. Bokov, and Z.-G. Ye, *Phys. Rev. B* 79, 144101 (2009).
- ²² D. I. Woodward and I. M. Reaney, *Acta Cryst. B* 61, 387 (2005).
- ²³ A. M. Glazer, *Acta Cryst. A* 31, 756 (1975).
- ²⁴ H. Hu, H. M. Chan, X. W. Zhang, and M. P. Harmer, *J. Am. Ceram. Soc.* 69, 594 (1986).
- ²⁵ N. Vittayakorn, G. Rujijanagul, X. Tan, M. A. Marquardt, and D. P. Cann, *J. Appl. Phys.* 96, 5103 (2004).
- ²⁶ A. A. Bokov and Z.-G. Ye, *J. Mater. Sci.* 41, 31 (2006).
- ²⁷ L. E. Cross, *Ferroelectrics* 76, 241 (1987).
- ²⁸ X. Zhao, W. Qu, X. Tan, A. A. Bokov, and Z.-G. Ye, *Phys. Rev. B* 75, 104106 (2007).
- ²⁹ G. A. Smolenskii, *J. Phys. Soc. Jpn.* 28 (Supl.), 26 (1970).
- ³⁰ I. W. Chen, *J. Phys. Chem. Solids* 61, 197 (2000).
- ³¹ I. Grinberg, M. R. Suchomel, P. K. Davies, and A. M. Rappe, *J. Appl. Phys.* 98, 094111 (2005).
- ³² H. He and X. Tan, *Phys. Rev. B* 72, 024102 (2005).
- ³³ W. Qu, X. Zhao, and X. Tan, *J. Appl. Phys.* 102, 084101 (2007).

CHAPTER 5. *In situ* Transmission Electron Microscopy Study on the Phase Transitions in Lead-Free $(1-x)(\text{Bi}_{1/2}\text{Na}_{1/2})\text{TiO}_3-x\text{BaTiO}_3$ Ceramics

A paper published in *Journal of the American Ceramic Society* **94**, 4040 (2011)

Cheng Ma and Xiaoli Tan

Abstract

The phase transitions in unpoled lead-free $(1-x)(\text{Bi}_{1/2}\text{Na}_{1/2})\text{TiO}_3-x\text{BaTiO}_3$ ($x = 0.06$ and 0.11) ceramics are investigated using hot-stage transmission electron microscopy (TEM). It is found that large ferroelectric domains in both ceramics start to disappear around T_d , the depolarization temperature. After the transition, both compositions exhibit the *P4bm* tetragonal symmetry in the form of nanodomains. The structural transition observed by the *in situ* TEM experiments seems to be gradual and occurs within a temperature range of several tens of degrees, in contrast to the sharp anomaly at T_d revealed by the dielectric characterization. With further increasing temperature, no structural change was observed for both compositions across T_{RE} , where the dielectric frequency dispersion vanishes, and T_m , where the dielectric permittivity reaches maximum. The tetragonal-to-cubic transition is diffuse and takes place in a broad temperature window well above both T_{RE} and T_m . These

results of structural phase transitions are summarized in a phase diagram with its composition range covering the morphotropic phase boundary (MPB).

5.1 Introduction

The development of high-performance lead-free piezoelectric ceramics becomes an increasingly urgent task because of the environmental concerns raised by lead-containing piezoelectric ceramics such as $\text{Pb}(\text{Zr},\text{Ti})\text{O}_3$.¹ The $(1-x)(\text{Bi}_{1/2}\text{Na}_{1/2})\text{TiO}_3-x\text{BaTiO}_3$ solid solution system, whose piezoelectric properties peak at its morphotropic phase boundary (MPB) $x \approx 0.06$, has shown great promises for piezoelectric applications.¹⁻³⁰ However, several fundamental issues, especially those on the structure-property relationships, are not very well understood in this system and the origin of the piezoelectric strain is still unclear.³⁴ The complications regarding the structure-property relationships in $(1-x)(\text{Bi}_{1/2}\text{Na}_{1/2})\text{TiO}_3-x\text{BaTiO}_3$ can be traced back to the base compound $(\text{Bi}_{1/2}\text{Na}_{1/2})\text{TiO}_3$, which displays decoupled crystal structures and dielectric properties.⁶⁻⁹ Neutron diffraction experiments¹¹ indicate that $(\text{Bi}_{1/2}\text{Na}_{1/2})\text{TiO}_3$ exhibits $R3c$ symmetry below 255 °C, $P4bm$ symmetry from 400 to 500 °C, and $Pm\bar{3}m$ symmetry above 540 °C. The $R3c$ and $P4bm$ phases coexist between 255 °C and 400 °C, and the $P4bm$ and $Pm\bar{3}m$ phases coexist between 500 °C and 540 °C. Structural refinements suggest that the tetragonal $P4bm$ phase exhibits Ti^{4+} displacements antiparallel to those of $\text{Bi}^{3+}/\text{Na}^+$.¹¹ However, dielectric characterizations

reveal that the room-temperature ferroelectric state in $(\text{Bi}_{1/2}\text{Na}_{1/2})\text{TiO}_3$ transforms to an antiferroelectric state at ~ 230 °C (T_d) where a hump in dielectric constant and loss tangent was observed, and then to a paraelectric one at ~ 340 °C (T_m) where dielectric constant exhibits a maximum.⁴ The disconnection between the structural and the dielectric transitions is poorly understood.

The dielectric phase transitions in $(\text{Bi}_{1/2}\text{Na}_{1/2})\text{TiO}_3$ are inherited by the MPB compositions of $(1-x)(\text{Bi}_{1/2}\text{Na}_{1/2})\text{TiO}_3-x\text{BaTiO}_3$,^{4-30,10} but the structure-property relationship against temperature is unknown due to the absence of systematic temperature dependent structural studies. In the recently reported phase diagram for unpoled $(1-x)(\text{Bi}_{1/2}\text{Na}_{1/2})\text{TiO}_3-x\text{BaTiO}_3$ ceramics (Fig. 5.1),^{11,12} excellent structure-property correlation against composition was observed at room temperature. The unique relaxor antiferroelectric (AFE) behavior is associated with nanodomains with $P4bm$ symmetry in the phase region $0.07 \leq x \leq 0.09$, and long-range ferroelectric (FE) order was observed in both neighboring phase regions with large ferroelectric domains. The MPB composition $x = 0.06$ displays a two-phase mixture with volumes of $R3c$ ferroelectric domains embedded in the matrix of $P4bm$ nanodomains, while the composition $x = 0.11$ contains both $P4bm$ nanodomains and $P4mm$ large lamellar ferroelectric domains. Based on the excellent structure-property correlation at room temperature, it was further speculated that the $R3c$ complex domains in $x \leq 0.06$ and the $P4mm$ lamellar domains in $x \geq 0.11$ transform to the $P4bm$ nanodomains across T_d , the

dielectric anomaly delineating the FE and relaxor AFE regions in Fig. 5.1.^{11,12} Given the aforementioned complications arising from the decoupled dielectric and structural transitions in $(\text{Bi}_{1/2}\text{Na}_{1/2})\text{TiO}_3$,⁶⁻⁹ experimental evidences are needed to verify this speculation. In addition, the structure-property relationship across T_{RE} , where the dielectric frequency dispersion vanishes,^{11,12} and T_m , where the dielectric permittivity peaks,⁴ is unknown for the compositions around the MPB. It has been proposed that T_{RE} may not correspond to a structural change.¹² As for T_m , a recent study suggests that the tetragonal-cubic transition temperature drops towards T_m with increasing x , and these two transition temperatures start to converge in $x = 0.05$.¹⁰ For $x > 0.05$, though, the anelastic anomaly caused by the tetragonal-cubic transition becomes extremely broadened, which prevents accurate determination of the structural transition temperature.¹⁰ Whether the tetragonal-cubic transition temperature merges with T_m , and how the domain structure evolves with temperature above T_m for $x > 0.05$ thus remain open questions. In the present work, hot-stage transmission electron microscopy (TEM) study was performed on ceramics of $x = 0.06$ and 0.11 to reveal the structural transitions.

5.2 Experimental procedure

The preparation of $(1-x)(\text{Bi}_{1/2}\text{Na}_{1/2})\text{TiO}_3-x\text{BaTiO}_3$ polycrystalline ceramics and TEM specimens was reported previously.^{11,12} Hot-stage TEM experiments on ceramic specimens

of $x = 0.06$ and 0.11 were performed on a Phillips CM-30 microscope operated at 300 kV. Bright field micrographs, centered-dark-field (CDF) micrographs, and selected area electron diffraction (SAED) patterns were recorded with a charge-coupled device camera during specimen heating. The temperature was increased in a stepwise manner with a step size ~ 20 °C and each step took ~ 1 minute. At temperature points of interest, TEM micrographs and/or diffraction patterns were recorded 10 minutes after the temperature reading was stabilized. Due to the concern of possible evaporation loss of Bi^{3+} and Na^+ , all specimens were heated to a temperature at or below 600 °C and the whole heating experiment was finished within 3 hours.

5.3 Results and discussion

5.3.1 Phase transitions across T_d

In agreement with previous results,^{11,12} ~ 40 % of the grains in the composition $x = 0.06$ at room temperature exhibit the mixed-phase structure with volumes of complex ferroelectric domains embedded in the matrix of nanodomains, and the rest of the grains contain nanodomains only. Figure 5.2(a) displays the room-temperature bright field image of a grain with the mixed-phase structure along the [112] zone axis. The volume in the center of the micrograph is occupied by ferroelectric domains in a complex pattern. These domains

exhibit the $R3c$ symmetry as characterized by the presence of strong $\frac{1}{2}\{ooo\}$ and absence of $\frac{1}{2}\{ooe\}$ superlattice spots [Fig. 5.2(b)] (o and e denotes odd and even Miller indices, respectively).²²⁻¹⁵ The nanodomains in the volume surrounding the $R3c$ ferroelectric domains possess the $P4bm$ symmetry as evidenced by the presence of $\frac{1}{2}\{ooe\}$ and absence of $\frac{1}{2}\{ooo\}$ spots [Fig. 5.2(c)].^{11,14,22-15}

With increasing temperature, the volume containing the complex ferroelectric domains starts to shrink at around 130 °C and this process continues until ~170 °C where the whole grain is completely occupied by nanodomains with the $P4bm$ symmetry. Figure 5.2(d) depicts the morphology of the volume with $R3c$ ferroelectric domains at 140 °C. Obviously the $R3c \rightarrow P4bm$ structural phase transition takes place through the motion of the interphase boundary: The volume with $P4bm$ nanodomains expands at the expense of the volume with the $R3c$ complex ferroelectric domains and finally occupies the whole grain above 170 °C [Fig. 5.2(e)]. Figures 5.2(f) and 5.2(g) display the SAED patterns recorded at 190 °C from the volume originally occupied by $R3c$ ferroelectric domains and from the surrounding volume, respectively. Both show identical diffraction patterns with apparent $\frac{1}{2}\{ooe\}$ spots.

We have proposed a new term “relaxor antiferroelectric” to describe the dielectric behavior of the $P4bm$ phase for its strong frequency dispersion and its nanometer-sized domains in our previous work.^{11,12} It is in analogy with “relaxor ferroelectric” which has

been used to describe $\text{Pb}(\text{Mg}_{1/3}\text{Nb}_{2/3})\text{O}_3$ where the nanodomains are ferroelectric ones.¹⁶⁻¹⁸

For the “relaxor antiferroelectric” $P4bm$ phase in $(1-x)(\text{Bi}_{1/2}\text{Na}_{1/2})\text{TiO}_3-x\text{BaTiO}_3$, the nanodomains are of antiferroelectric nature because the displacements of A-site cations (Bi^{3+} , Na^+ , Ba^{2+}) are antiparallel to the displacement of B-site cation (Ti^{4+}) within each individual nanodomain. However, the dipole moment resulted from the Ti^{4+} displacement is not fully cancelled by that from the A-site cation displacement in the unit cell.¹¹ Therefore, the nanodomains in the $P4bm$ phase are actually uncompensated antiferroelectric, or weakly polar ferrielectric domains.¹² As a result, the dielectric behavior of the $P4bm$ relaxor antiferroelectric phase is similar to that of a relaxor ferroelectric in many aspects.¹²

For the unpoled ceramic of $x = 0.06$, dielectric measurements indicated that T_d is 115 °C (Fig. 5.1).^{11,12} Considering the difference in the sample geometry for dielectric and TEM characterizations and the accuracy in the temperature reading for hot-stage TEM experiments, the observed $R3c$ -to- $P4bm$ structural phase transition from the *in situ* TEM study seems to correlate with the ferroelectric-to-relaxor-antiferroelectric transition at T_d from the dielectric characterization.

Similar results were observed in $x = 0.11$ (Fig. 5.3). At room temperature, the unpoled ceramic is dominated by lamellar ferroelectric domains [Fig. 5.3(a)]. Figure 5.3(b) is the SAED pattern along the [112] zone axis recorded from the area in the lower left portion of

the grain where nanodomains are observed [indicated by the bright arrow in Fig. 5.3(a)].

The presence of weak $\frac{1}{2}\{ooe\}$ and absence of $\frac{1}{2}\{ooo\}$ superlattice spots confirm the $P4bm$ symmetry.^{11,14,22-15} As shown in Fig. 5.3(c), the large lamellar domains exhibit the $P4mm$ symmetry as characterized by the absence of any superlattice spots. During heating, the volume with $P4bm$ nanodomains started to grow at the expense of lamellar domains at 170 °C and all the lamellar domains in the grain disappeared at 240 °C. Figure 5.3(e) displays the bright field micrograph recorded at 250 °C for the same grain where faint contrast of nanodomains is evident. The $\frac{1}{2}\{ooe\}$ superlattice spots, although very weak, are still visible at this temperature (see the inset). Therefore, the $P4mm \rightarrow P4bm$ structural transition appears to correlate well with the dielectric transition at T_d , which is 170 °C for $x = 0.11$ (Fig. 5.1).^{11,12}

The present *in situ* TEM study demonstrates that the temperature T_d not only marks the ferroelectric-to-relaxor-antiferroelectric phase transition, but also corresponds to structural changes in the $(1-x)(Bi_{1/2}Na_{1/2})TiO_3-xBaTiO_3$ binary solid solution system. The results are hence in supportive of the phase diagram we proposed previously for unpoled ceramics.^{11,12} However, it should be noted that the dielectric transition at T_d is sharp while the structural transition revealed by *in situ* TEM experiments takes place over a wide temperature window of several tens of degrees. Although exact reasons for this discrepancy are the subject for

future studies, the different sample geometry and in turn the different electromechanical boundary conditions definitely are contributing factors.

5.3.2 Transitions across and beyond T_{RE} and T_m

More detailed hot-stage TEM study was performed on the nanodomains in $x = 0.06$ and 0.11 in order to investigate the domain structures at high temperatures up to 600 °C. Figure 5.4 displays the CDF image of the nanodomains in $x = 0.06$ at room temperature, which was formed with the $\frac{1}{2}(3\bar{1}0)$ superlattice diffraction spot in the $[130]_c$ zone axis. The CDF micrograph reveals that the nanodomains (bright speckles) took a thin platelet shape parallel to the (001) plane, which causes streaking of $\frac{1}{2}\{ooe\}$ diffraction spots along the $[001]$ direction (inset of Fig. 5.4). The matrix with dark contrast should be a mixture of nanodomains of other variants and the cubic perovskite phase.¹² No detectable change in the shape, size, or population of the nanodomains was observed from room temperature up to 335 °C. Dark field imaging was not performed beyond 335 °C due to the severe drifting and weak contrast.

Figure 5.5 displays the $[130]_c$ zone axis SAED patterns in $x = 0.06$ recorded from the volume occupied by nanodomains at a series of temperatures. The characteristic feature of the $P4bm$ symmetry, *i.e.* the presence of $\frac{1}{2}\{ooe\}$ and absence of $\frac{1}{2}\{ooo\}$ superlattice spots, persists to temperatures well beyond T_m , which is ~ 280 °C for $x = 0.06$.¹² The SAED

pattern does not exhibit any significant change up to 335 °C [Figs. 5.5(a) and (b)]. Gradual weakening of the $\frac{1}{2}\{ooe\}$ spots was observed above 335 °C, as exemplified by the SAED pattern recorded at 425 °C [Fig. 5.5(c)]. This indicates that the tetragonal-to-cubic structural transition started to occur at 335 °C. Above 335 °C, the $\frac{1}{2}\{ooe\}$ spots become more diffused and severely streaking with increasing temperature, suggesting that the size, in addition to the population, of the *P4bm* nanplatelets is also decreasing during the structural transition. When the temperature reached 500 °C, as shown in Fig. 5.5(d), only weak residues of the $\frac{1}{2}\{ooe\}$ spots were observed and they remained, although barely detectable, even at 600 °C. The *in situ* TEM results thus suggest that the tetragonal (*P4bm*) to cubic structural transition starts at 335 °C and completes at 500 °C. However, the high-temperature phase (at least between 500 and 600 °C) seems not to be a “clean” cubic phase. The persistent residues of $\frac{1}{2}\{ooe\}$ superlattice spots, which have also been observed in pure $(Bi_{1/2}Na_{1/2})TiO_3$ up to 620 °C,¹⁹ reveal the presence of local lattice distortions. It should be noted that local lattice distortions in an average cubic structure has previously been revealed by the x-ray absorption fine structure in pure $(Bi_{1/2}Na_{1/2})TiO_3$ at 600 °C.²⁰ Note that T_{RE} and T_m for $x = 0.06$ are 240 °C and 280 °C, respectively (Fig. 5.1), from dielectric measurements.^{11,12} The lack of obvious changes in either the domain morphology or the superlattice diffraction spots up to 335 °C from this study indicates that the

dielectric anomalies at T_{RE} and T_m do not correspond to any structural phase transitions.

The tetragonal-to-cubic structural transition occurs progressively between 335 °C and 500 °C.

Figure 5.6 displays the SAED patterns of nanodomains in $x = 0.11$ at different temperatures. Similar to $x = 0.06$, the SAED patterns exhibit $\frac{1}{2}\{ooe\}$ superlattice spots without $\frac{1}{2}\{ooo\}$ ones. The $\frac{1}{2}(3\bar{1}0)$ superlattice diffraction spot from the nanodomains was very weak even at room temperature for $x = 0.11$ [Fig. 5.6(a)], so the CDF image was not recorded. The bright field images (not shown here) could not reveal any obvious morphology change of nanodomains from room temperature to 600 °C. The superlattice spots with streaking at all temperatures studied suggest a thin platelet domain morphology of the $P4bm$ phase, which is similar to that in $x = 0.06$ (Fig. 5.4). Weakening in the $\frac{1}{2}\{ooe\}$ superlattice spots is noted at 310 °C [Fig. 5.6(b)]. However, these superlattice spots are still discrete and can be distinguished from background at this temperature. As the temperature further increased, the superlattice spots are more dramatically elongated and diffused [Fig. 5.6(c)]. At 425 °C, the superlattice diffractions become so weak and streaked that they can hardly be distinguished as individual spots [Fig. 5.6(d)]. No significant change was observed in the SAED patterns with increasing temperature above 425 °C, except the slow and gradual weakening of the diffuse residues of the superlattice diffractions. These residues are still visible up to 550 °C and eventually cannot be well recorded at 600 °C. Thus the *in situ* TEM study suggests that the tetragonal-to-cubic structural transition starts at

a temperature slightly below 310 °C and finishes at 425 °C in the composition of $x = 0.11$. The local distortions in the high-temperature cubic phase are gradually weakening with increase in temperature and persist up to at least 550 °C. The dielectric transition temperatures T_{RE} and T_m for $x = 0.11$ are 255 and 275 °C, respectively (Fig. 5.1).^{11,12} Again, neither of them is associated with the tetragonal-to-cubic structural phase transition according to the present hot-stage TEM study.

Summarizing the results of this study and previous work,¹⁰⁻¹² a schematic phase diagram accounting for the structural phase transitions in unpoled $(1-x)(\text{Bi}_{1/2}\text{Na}_{1/2})\text{TiO}_3 - x\text{BaTiO}_3$ ceramics can be constructed (Fig. 5.7). While the dielectric anomaly T_d correlates well with the structural transition to the $P4bm$ phase, the dielectric anomalies at T_{RE} and T_m do not correspond to any structural phase transition. The tetragonal-to-cubic structural transition takes place progressively within a wide temperature range above T_m where both the size and the population of the platelets of $P4bm$ nanodomains decrease with increasing temperature. The extremely weak residues of $\frac{1}{2}\{ooe\}$ superlattice diffractions observed after this structural transition reveals the presence of local lattice distortions in the high-temperature cubic phase, similar to those in pure $(\text{Bi}_{1/2}\text{Na}_{1/2})\text{TiO}_3$.²⁰ However, the gradual weakening of these residues after the structural transition appears to suggest such distortion may eventually disappear at higher temperatures. This scenario agrees with

previous anelasticity measurement results which indicate a broad and diffuse tetragonal-to-cubic transition above T_m in compositions of $x \geq 0.05$.¹⁰

5.4 Conclusions

In summary, structural phase transitions in unpoled $(1-x)(\text{Bi}_{1/2}\text{Na}_{1/2})\text{TiO}_3-x\text{BaTiO}_3$ ceramics were investigated using hot-stage TEM. The dielectric transition at T_d is found to be correlated with structural transitions to a $P4bm$ tetragonal phase. Nanodomains with the $P4bm$ symmetry are confirmed in compositions of $x = 0.06$ and 0.11 at temperatures above T_d . With further increase in temperature, no structural phase transition is observed to occur at T_{RE} or T_m . The tetragonal-to-cubic phase transition takes place progressively within a wide temperature range above T_m : from 335 °C to 500 °C in $x = 0.06$ and from a temperature slightly below 310 °C to 425 °C in $x = 0.11$. Local distortions are present in the high-temperature cubic phase after the tetragonal-to-cubic structural transition and persist to temperatures close to 600 °C. Such local distortions are expected to eventually vanish with further increase in temperature.

Acknowledgements

This work was supported by the National Science Foundation (NSF) through Grant DMR-1037898. TEM experiments were performed at the Ames Laboratory which is

operated for the U.S. Department of Energy by Iowa State University under Contract No. DE-AC02-07CH11358.

Figures

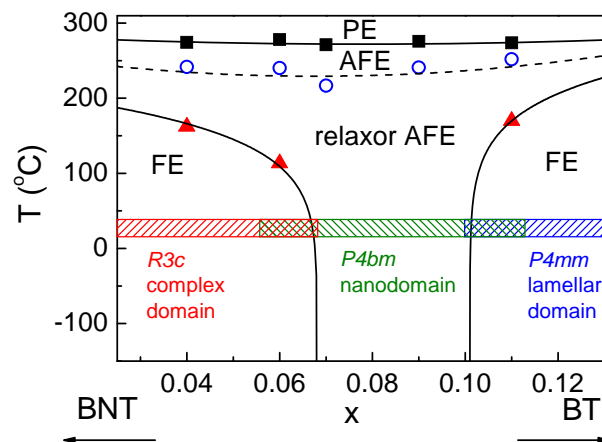


Figure 5.1 The phase diagram for unpoled $(1-x)(\text{Bi}_{1/2}\text{Na}_{1/2})\text{TiO}_3 - x\text{BaTiO}_3$ ceramics.¹² Note that the transition temperatures are determined from dielectric characterizations rather than structural analysis. The dielectric constant and loss tangent curves of the compositions with $0.04 \leq x \leq 0.11$, including the two compositions for the *in situ* TEM study here, were reported in Ref. 12.

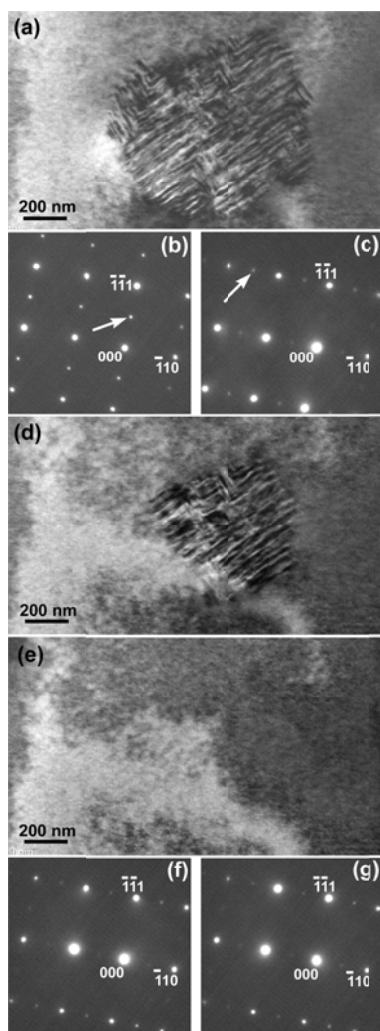


Figure 5.2 *In situ* TEM experiment on the $0.94(\text{Bi}_{1/2}\text{Na}_{1/2})\text{TiO}_3 - 0.06\text{BaTiO}_3$ ceramic along the [112] zone axis. (a) The bright field micrograph at 25°C ; (b) the SAED pattern recorded at 25°C from the volume with complex ferroelectric domains in the central portion of (a); (c) the SAED pattern recorded at 25°C from the surrounding volume in the grain with relaxor antiferroelectric nanodomains; (d) the same grain at 140°C ; (e) the same grain at 190°C ; (f) the SAED pattern recorded at 190°C from the volume originally occupied by complex ferroelectric domains; (g) the SAED pattern recorded at 190°C from the surrounding volume.

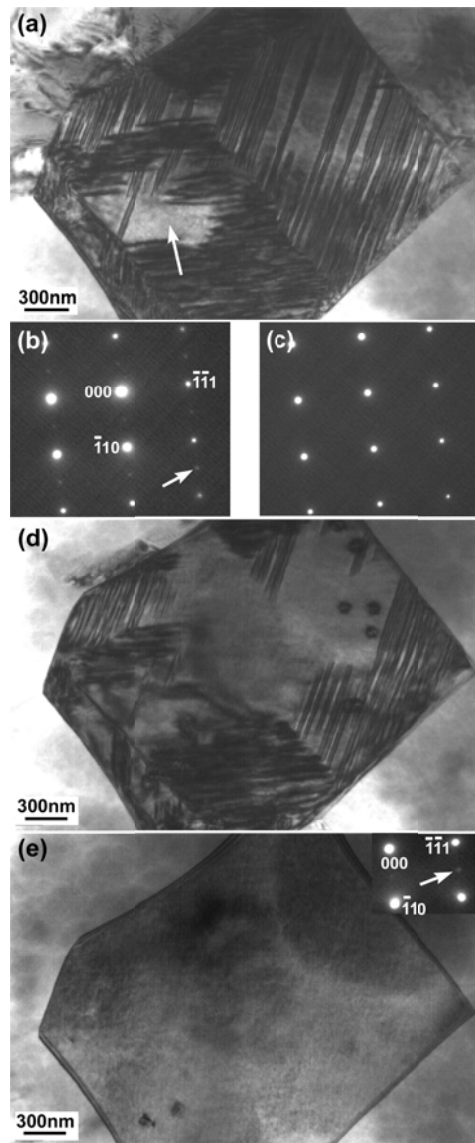


Figure 5.3 *In situ* TEM experiment on the $0.89(\text{Bi}_{1/2}\text{Na}_{1/2})\text{TiO}_3 - 0.11\text{BaTiO}_3$ ceramic along the [112] zone axis. (a) The bright field micrograph at 25°C ; (b) the SAED pattern recorded at 25°C from the volume occupied by relaxor antiferroelectric nanodomains [indicated by the bright arrow in (a)]; (c) the SAED pattern recorded at 25°C from the volume with large lamellar domains in the grain; (d) the same grain at 200°C ; and (e) the same grain at 250°C . The inset in (e) shows the SAED pattern recorded at 250°C .

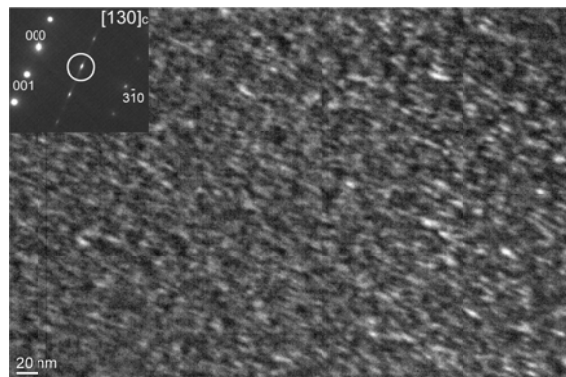


Figure 5.4 Centered-dark-field image of the relaxor antiferroelectric nanodomains in the $0.94(\text{Bi}_{1/2}\text{Na}_{1/2})\text{TiO}_3\text{--}0.06\text{BaTiO}_3$ ceramic at room temperature. The image was formed using the $\frac{1}{2}(3\bar{1}0)$ superlattice diffraction spot in the $[130]_c$ zone-axis. The inset shows the SAED pattern with the $\frac{1}{2}(3\bar{1}0)$ spot circled.

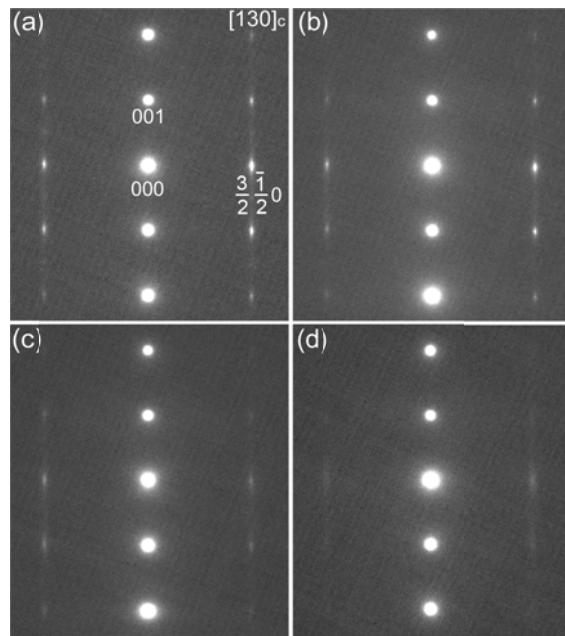


Figure 5.5 The [130]_c zone-axis SAED patterns of the nanodomains in the 0.94(Bi_{1/2}Na_{1/2})TiO₃–0.06BaTiO₃ ceramic at (a) room temperature, (b) 335 °C, (c) 425 °C, (d) 500 °C.

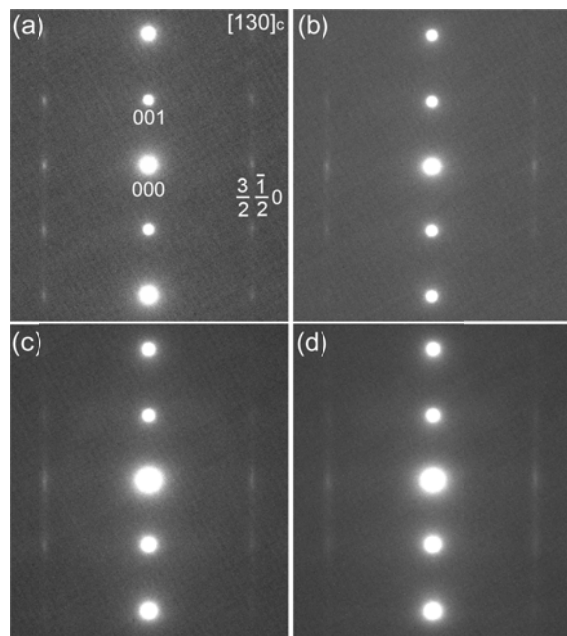


Figure 5.6 The $[130]_c$ zone-axis SAED patterns of the nanodomains in the $0.89(\text{Bi}_{1/2}\text{Na}_{1/2})\text{TiO}_3 - 0.11\text{BaTiO}_3$ ceramic recorded at (a) room temperature, (b) 310°C , (c) 360°C , (d) 425°C .

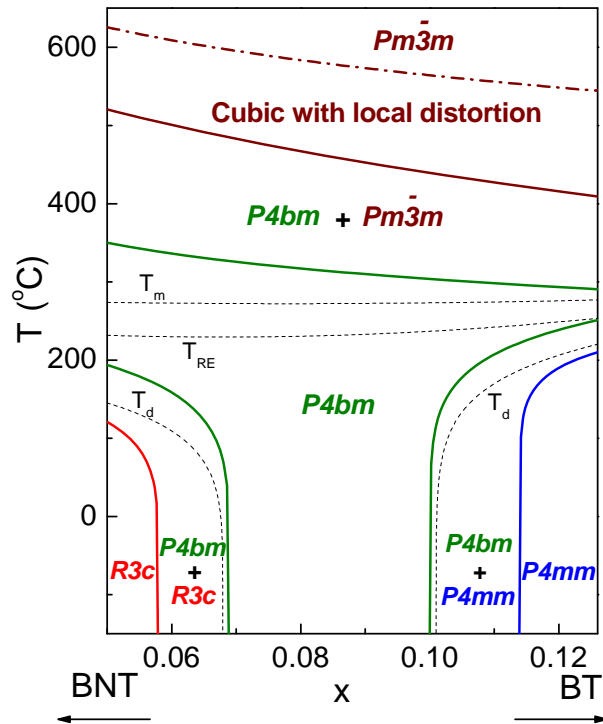


Figure 5.7 A schematic phase diagram for structural phase transitions in unpoled $(1-x)(\text{Bi}_{1/2}\text{Na}_{1/2})\text{TiO}_3-x\text{BaTiO}_3$ ceramics. The thick solid and dash-dot lines (colored) delineate the structural phase regions. For comparison, the temperatures for dielectric anomalies (T_d , T_{RE} , T_m) are included as dark dashed lines.

References

- ¹ J. Rödel, W. Jo, K. Seifert, E. M. Anton, T. Granzow, and D. Damjanovic, "Perspective on the Development of Lead-Free Piezoceramics," *J. Am. Ceram. Soc.*, **92**, 1153 (2009).
- ² T. Takenaka, K. Maruyama, and K. Sakata, "(Bi_{1/2}Na_{1/2})TiO₃-BaTiO₃ System for Lead-Free Piezoelectric Ceramics," *Jpn. J. Appl. Phys.*, Part 1 **30**, 2236 (1991).
- ³ Y. Hiruma, Y. Watanabe, H. Nagata, and T. Takenaka, "Phase Transition Temperatures of Divalent and Trivalent Ions Substituted Bi_{0.5}Na_{0.5}TiO₃ Ceramics," *Key Eng. Mater.*, **350**, 93 (2007).
- ⁴ C. Xu, D. Lin, and K. W. Kwok, "Structure, Electrical Properties and Depolarization Temperature of (Bi_{0.5}Na_{0.5})TiO₃-BaTiO₃ Lead-Free Piezoelectric Ceramics," *Solid State Sci.*, **10**, 934 (2008).
- ⁵ J. E. Daniels, W. Jo, J. Rödel, and J. L. Jones, "Electric-Field-Induced Phase Transformation at a Lead-Free Morphotropic Phase Boundary: Case Study in a 93%(Bi_{0.5}Na_{0.5})TiO₃-7%BaTiO₃ Piezoelectric Ceramic," *Appl. Phys. Lett.*, **95**, 032904 (2009).
- ⁶ C. S. Tu, I. G. Siny, and V. H. Schmidt, "Sequence of Dielectric Anomalies and High-Temperature Relaxation Behavior in Na_{1/2}Bi_{1/2}TiO₃," *Phys. Rev. B*, **49**, 11550 (1994).
- ⁷ G. O. Jones and P. A. Thomas, "Investigation of the Structure and Phase Transitions in the Novel A-site Substituted Distorted Perovskite Compound Na_{0.5}Bi_{0.5}TiO₃," *Acta Cryst.*, **B58**, 168 (2002).

- ⁸ V. Dorcet, G. Trolliard, and P. Boullay, "Reinvestigation of Phase Transitions in $\text{Na}_{0.5}\text{Bi}_{0.5}\text{TiO}_3$ by TEM. Part I: First Order Rhombohedral to Orthorhombic Phase Transition," *Chem. Mater.*, **20**, 5061 (2008).
- ⁹ J. Yao, W. Ge, L. Luo, J. Li, D. Viehland, and H. Luo, "Hierarchical Domains in $\text{Na}_{1/2}\text{Bi}_{1/2}\text{TiO}_3$ Single Crystals: Ferroelectric Phase Transformations within the Geometrical Restrictions of a Ferroelastic Inheritance," *Appl. Phys. Lett.*, **96**, 222905 (2010).
- ¹⁰ F. Cordero, F. Craciun, F. Trequattrini, E. Mercadelli, and C. Galassi, "Phase Transitions and Phase Diagram of the Ferroelectric Perovskite $(\text{Na}_{0.5}\text{Bi}_{0.5})_{1-x}\text{Ba}_x\text{TiO}_3$ by Anelastic and Dielectric Measurements," *Phys. Rev. B*, **81**, 144124 (2010).
- ¹¹ C. Ma and X. Tan, "Phase Diagram of Unpoled Lead-Free $(1-x)(\text{Bi}_{1/2}\text{Na}_{1/2})\text{TiO}_3\text{-}x\text{BaTiO}_3$ Ceramics," *Solid State Commun.*, **150**, 1497 (2010).
- ¹² C. Ma, X. Tan, E. Dul'kin, and M. Roth, "Domain Structure-Dielectric Property Relationship in Lead-Free $(1-x)(\text{Bi}_{1/2}\text{Na}_{1/2})\text{TiO}_3\text{-}x\text{BaTiO}_3$ Ceramics," *J. Appl. Phys.*, **108**, 104105 (2010).
- ¹³ D. I. Woodward and I. M. Reaney, "Electron Diffraction of Tilted Perovskites," *Acta Cryst.*, **B61**, 387 (2005).
- ¹⁴ A. M. Glazer, "Simple Ways of Determining Perovskite Structures," *Acta Cryst.*, **A31**, 756 (1975).
- ¹⁵ L. A. Schmitt and H. J. Kleebe, "Single Grains Hosting Two Space Groups - a Transmission Electron Microscopy Study of a Lead-Free Ferroelectric," *Funct. Mater. Lett.*, **3**, 55 (2010).
- ¹⁶ L. E. Cross, "Relaxor Ferroelectrics," *Ferroelectrics*, **76**, 241 (1987).

- ¹⁷ X. Zhao, W. Qu, H. He, N. Vittayakorn, and X. Tan, "Influence of Cation Order on the Electric Field-Induced Phase Transition in Pb(Mg_{1/3}Nb_{2/3})O₃-Based Relaxor Ferroelectrics," *J. Am. Ceram. Soc.*, **89**, 202 (2006).
- ¹⁸ X. Zhao, W. Qu, X. Tan, A. Bokov, and Z.-G. Ye, "Electric Field-Induced Phase Transitions in (111)-, (110)-, and (100)-Oriented Pb(Mg_{1/3}Nb_{2/3})O₃ Single Crystals," *Phys. Rev. B*, **75**, 104106 (2007).
- ¹⁹ G. Trolliard and V. Dorcet, "Reinvestigation of Phase Transitions in Na_{0.5}Bi_{0.5}TiO₃ by TEM. Part II: Second Order Orthorhombic to Tetragonal Phase Transition," *Chem. Mater.*, **20**, 5074 (2008).
- ²⁰ V. A. Shuvaeva, D. Zekria, A. M. Glazer, Q. Jiang, S. M. Weber, P. Bhattacharya, and P. A. Thomas, "Local Structure of the Lead-Free Relaxor Ferroelectric (K_xNa_{1-x})_{0.5}Bi_{0.5}TiO₃," *Phys. Rev. B*, **71**, 174114 (2005).

CHAPTER 6. Creation and Destruction of Morphotropic Phase**Boundaries through Electrical Poling of Ferroelectric Materials**

A paper under review in *Physical Review Letters*

Cheng Ma, Hanzheng Guo, Scott P. Beckman, and Xiaoli Tan

Abstract

We report the first direct evidence that the morphotropic phase boundary (MPB) in ferroelectric materials, along with the associated strong piezoelectricity, can be created, destroyed, or even replaced by another MPB through phase transitions during electrical poling. The real-time evolution of crystal structure and domain morphology during the poling-induced phase transitions in $(\text{Bi}_{1/2}\text{Na}_{1/2})\text{TiO}_3\text{-BaTiO}_3$ is observed with *in-situ* transmission electron microscopy. These observations elucidate the microstructural origin of the macroscopic piezoelectricity's dependence on the poling field and previously unexplained strain behaviors. This study demonstrates that the ferroelectric-to-ferroelectric transitions during the poling process can completely alter the MPBs, and hence must be comprehensively investigated when interpreting the microscopic mechanism of macroscopic piezo- and ferroelectric behaviors.

6.1 Introduction

A material with coexisting energetically comparable states often displays extraordinary responses to external stimuli, such as large magnetostriction [1], giant electrocaloric effect [2], and colossal magnetoresistance [3]. In the case of piezoelectricity, ultrahigh piezoelectric responses are realized in compositions at the morphotropic phase boundary (MPB), where multiple ferroelectric phases with different crystal structures coexist [4-9]. Since piezoelectricity is forbidden by centrosymmetry, MPB materials (especially those in the polycrystalline form) have to be poled by electric fields, which break the macroscopic centrosymmetry through aligning the polarizations towards the applied field direction, in order to exhibit piezoelectricity [4]. Under poling fields, the energy landscape of the constitutive polar phases in the MPB composition may well be altered differently. Therefore, knowledge about the real-time evolution of crystal structures and domain morphologies during and after electrical poling is essentially important in understanding the physics of piezoelectricity.

However, in the past six decades, both theoretical and experimental studies are mainly focused on the virgin state of materials, prior to the application of a poling field [4-9]. Although different models on the piezoelectricity enhancement associated with MPBs have been proposed to describe interesting microscopic behaviors at zero field, the essential

understanding of the microstructural mechanisms cannot be established without a complete picture of the *in-situ* structural evolution under poling fields [10]. As a result, many fundamental questions remain unanswered for decades: Will MPBs survive the strong electric fields during poling? Can the poling field create an MPB in originally single-phase ferroelectrics? If poling fields can create or destroy MPBs, will such changes be preserved after the fields are removed? How does the change in MPBs during poling impact the macroscopic piezoelectric property?

Conclusive answers to these questions demand *in-situ* real-time structural characterizations. There are two principal difficulties that hinder such studies. First, the crystal structures of different perovskite ferroelectric phases are frequently too similar to be well resolved by X-ray or neutron diffractions. It is particularly difficult to distinguish a material with coexisting phases from a single-phase material with a more complicated crystal structure. For example, there has been a continued debate on the crystal structures of the MPB in $\text{Pb}(\text{Zr},\text{Ti})\text{O}_3$ (single monoclinic phase *vs.* mixed rhombohedral and tetragonal phases) [5,6], the most important and widely studied piezoelectric compositions. Second, *in-situ* application of electric fields in ferroelectric materials inevitably leads to a large piezoelectric strain and causes a complicated shifting of the diffraction peaks ($\eta_{hkl} = (d_{hkl}^E - d_{hkl}^0)/d_{hkl}^0$, where η_{hkl} is the piezoelectric lattice strain, d_{hkl}^E and d_{hkl}^0 are the lattice spacing of the (hkl) plane with and without field, respectively) [10]. Moreover, electric-field-induced domain

texture has to be taken into account in the structural analysis. These complications make the phase identification using x-ray/neutron diffractions particularly challenging.

These issues can be alleviated by using electric-field *in-situ* transmission electron microscopy (TEM). Unlike x-ray/neutron diffraction, which obtains average structural information of materials, TEM is capable of precisely resolving the crystal structure of each individual phase among mixed phases through selected area electron diffraction. Furthermore, *in-situ* TEM visualizes the real-time domain morphology changes under electric field, which is a direct manifestation of the polarization switching process. However, electric-field *in-situ* TEM requires very delicate sample preparation, and thus the number of such studies is still very limited [11-15].

In this Letter, direct evidences from electric-field *in-situ* TEM experiments and corresponding piezoelectricity measurements provide conclusive answers to the questions raised above; we demonstrate that MPBs, and the enhanced piezoelectric response associated with them, can be either destroyed or created irreversibly during poling. Our first-principles calculations reveal that the ferroelectric phases are energetically close to each other, which corroborates the experimental conclusions. This study establishes the dynamic correlation between the evolution of MPBs and the change of macroscopic property during electrical

poling. It paves the way for the development of the next generation energetically efficient and environmentally friendly piezoelectric materials.

One of the most extensively studied lead-free piezoelectrics, the $(1-x)(\text{Bi}_{1/2}\text{Na}_{1/2})\text{TiO}_3-x\text{BaTiO}_3$ solid solution [9,16-18], was selected to demonstrate the concept. In the virgin state prior to poling, these ceramics crystallize in the rhombohedral $R3c$ ferroelectric phase for $x \leq 6\%$, the tetragonal $P4bm$ relaxor ferrielectric phase for $5\% \leq x \leq 11\%$, and the tetragonal $P4mm$ ferroelectric phase for $x \geq 10\%$ [19-21]. Therefore, one MPB with coexistent $R3c$ and $P4bm$ phases at $5\% \leq x \leq 6\%$ and another with $P4bm$ and $P4mm$ phases at $10\% \leq x \leq 11\%$ exist in the unpoled state. Compared with results reported on poled ceramics [22-25], an irreversible $P4bm$ -to- $P4mm$ phase transition is speculated to occur during poling for compositions with $x \geq 7\%$. We have recently confirmed this transition by *in-situ* structural studies for $x = 7\%$ with poling fields up to 2.5 kV/mm [14]. However, the stability of the induced $P4mm$ phase in $x = 7\%$ against poling fields above 2.5 kV/mm is unknown. Any additional ferroelectric-to-ferroelectric transitions at higher fields may create an MPB in this composition. By the same token, electric-field-induced phase transitions in $5\% \leq x \leq 6\%$, if any, could possibly destroy the existing MPB. To verify these speculations, our study focuses on three compositions: $x = 5.5\%$, 6% , and 7% .

6.2 Experiments and methods

The preparation of $(\text{Bi}_{1/2}\text{Na}_{1/2})\text{TiO}_3$ – BaTiO_3 ceramics and TEM specimens have been described elsewhere [20]. Electric-field *in-situ* TEM study was performed on a Phillips CM-30 microscope operated at 300 kV with a specially designed specimen holder, whose detailed configuration is shown schematically in Supplemental Material [26]. Bright-field images and selected area electron diffraction patterns were recorded with a charge-coupled device camera. For each of the three compositions over ten *in-situ* TEM experiments were conducted and the results confirm those reported here. The piezoelectric coefficient d_{33} of poled ceramics was measured with a piezo- d_{33} meter. Specimens (~8 mm diameter and ~0.7 mm thickness) were poled at room temperature under fields from 1.5 to 6.5 kV/mm with increasing sequence of field levels. At each level the specimen was poled for 20 minutes at room temperature and subsequently aged for 24 hours also at room temperature. Then the d_{33} value was measured ten times across the electrode surface.

The first-principles calculations were performed on the base compound $(\text{Bi}_{1/2}\text{Na}_{1/2})\text{TiO}_3$ using the density functional theory methods encoded in the ABINIT software package [27]. The exchange-correlation energy was approximated using the local density approximation [28] and in place of the all electron ion potentials projector augmented wave pseudopotentials were employed [29]. The plane wave expansion was truncated at 816 eV

and a $4 \times 4 \times 4$ Monkhorst-Pack \mathbf{k} -point mesh was used to integrate over the Brillouin zone [30]. This allowed the forces on the atoms to be converged to better than $10 \text{ meV}/\text{\AA}$. The supercells used in the calculation were based on a superlattice constructed of alternating layers of BiTiO_3 and NaTiO_3 stacked in the [111] direction. Though not a true representation of the A-site disordered $(\text{Bi}_{1/2}\text{Na}_{1/2})\text{TiO}_3$, it allows for a reasonable determination of the relative phase energies.

6.3 Results and discussion

The electric-field *in-situ* TEM results for $x = 6\%$ are displayed in Fig. 6.1. At zero field, consistent with previous studies [19,20], approximately 40% of the grains exhibit mixed *P4bm* and *R3c* phases (see Supplemental Material [26]), and the rest of the grains consist of *P4bm* nanodomains only [Fig. 6.1(a)]. The *P4bm* and *R3c* symmetries can be unambiguously determined from diffraction patterns: the *P4bm* symmetry is characterized by the presence of $1/2\{ooe\}$ (o and e denote odd and even miller indices, respectively) and absence of $1/2\{ooo\}$ superlattice diffraction spots [Fig. 6.1(e)], while the *R3c* symmetry by the presence of $1/2\{ooo\}$ and absence of $1/2\{ooe\}$ spots [19-21,31-34]. A grain with pure *P4bm* nanodomains [Fig. 6.1(a)] is focused in the *in-situ* study. Under applied electric fields, these nanodomains coalesce into lamellar domains and the $1/2\{ooe\}$ diffraction spots weaken. At 3.2 kV/mm a large part of the grain along the grain boundary transforms into

wedge-shaped domains [region R in Fig. 6.1(b)]. This region expands as the field is increased [Fig. 6.1(c)] and occupies the entire grain at 4.0 kV/mm [Fig. 6.1(d)]. The wedge-shaped domains exhibit *R3c* symmetry as demonstrated by electron diffraction [Fig. 6.1(f)]. The lamellar domains undergo a *P4bm*-to-*P4mm* transition at 3.2 kV/mm without any obvious change in morphology. This transition is demonstrated by the sudden decrease in the $1/2\{ooe\}$ spot intensity towards zero [Fig. 6.1(h)]. Therefore, the application of an electric field creates an *R3c/P4mm* MPB from the *P4bm* phase for fields ranging between 3.2 \sim 3.6 kV/mm. Further increase in the field destroys the MPB through a *P4mm*-to-*R3c* phase transition. These transitions during electrical poling are observed to be irreversible (see Supplemental Material [26]).

Prior to poling, the $x = 7\%$ ceramic is phase-pure with all the grains exhibiting the *P4bm* nanodomains [similar to those displayed in Fig. 6.1(a)]. The detailed electric-field *in-situ* TEM results from 0 to 2.5 kV/mm were reported previously [14]; *P4bm* nanodomains irreversibly transform to *P4mm* lamellar domains under electric fields. With further increase in poling fields, the same electric-field-induced *P4mm*-to-*R3c* transition as in $x = 6\%$ is also seen in $x = 7\%$; as shown in Fig. 6.2(a), *R3c* wedge-shaped domains (region R) form along with *P4mm* lamellar domains (region T) at 3.0 kV/mm. Unlike $x = 6\%$, this transition is not completed in $x = 7\%$ even under 4.0 kV/mm, the maximum field allowed by our *in-situ* experimental device. The increase of electric fields from 3.0 to 4.0 kV/mm only leads to

slight displacement of domain walls and minor migration of the $R3c/P4mm$ interphase boundary [Fig. 6.2(b)]. The mixed $R3c$ and $P4mm$ phases remain after the applied fields are removed. Therefore, an MPB with coexisting $R3c$ and $P4mm$ phases not only emerges under electric fields in $x = 7\%$, but also survives high poling fields.

In addition to $x = 6\%$ and 7% , *in-situ* TEM experiments were also performed on $x = 5.5\%$ (see Supplemental Material [26]). Almost all the grains of $x = 5.5\%$ exhibit mixed $R3c$ and $P4bm$ phases in the unpoled state. During poling the $P4bm$ phase irreversibly transforms into the $R3c$ phase; the poling process destroys the original $R3c/P4bm$ MPB.

The creation/destruction of MPBs by poling fields, which are directly revealed and confirmed by multiple *in-situ* TEM experiments, strongly correlates with the piezoelectric property measured from bulk ceramic samples, as shown in Fig. 6.3. The measured piezoelectric coefficient d_{33} for $x = 5.5\%$ is shown in Fig. 6.3(a) as a function of poling field. The increasing d_{33} is truncated by a plateau at a relatively low value of ~ 120 pC/N because the $R3c/P4bm$ MPB transforms to a single $R3c$ phase before the field is high enough to fully pole the ceramic. The d_{33} for $x = 6\%$, shown in Fig. 6.3(b), reaches its maximum at a greater value of ~ 131 pC/N due to the replacement of the original $R3c/P4bm$ MPB by the $R3c/P4mm$ MPB at intermediate poling fields. However, at higher poling fields the d_{33} response diminishes, because the $R3c/P4mm$ MPB is destroyed. Fig. 6.3(c) shows that the

d_{33} value of $x = 7\%$ increases monotonically and reaches the maximum of 167 pC/N at the highest poling field used in this study (6.5 kV/mm), which corresponds to the formation of a stable $R3c/P4mm$ MPB out of the single $P4bm$ phase during poling. Such excellent structure-property correlation is also evident across these three compositions at the same poling field, as shown in Fig. 6.3(d). The compositions with $x = 5.5\%$ and 6% , both exhibiting the single $R3c$ phase after poling at 6.5 kV/mm, possess almost identical d_{33} values, whereas the composition $x = 7\%$, exhibiting the $R3c/P4mm$ MPB after poling, shows a much higher d_{33} value. The results shown here are also consistent with previously reported d_{33} values of these compositions [18].

A poling field vs. composition phase diagram for the $(\text{Bi}_{1/2}\text{Na}_{1/2})\text{TiO}_3$ – BaTiO_3 binary system can be constructed to summarize the evolution of phases with poling fields at room temperature [Fig. 6.3(e)]. The critical fields in this diagram are estimated with bulk samples from the d_{33} results in this study [Figs. 6.3(a), (b), (c)] and from the volume strain measurements in a previous study [35]. The $R3c/P4bm$ and the $P4bm/P4mm$ phase boundaries converge as the poling field is increased. The horizontal “iso-field” line, where $R3c$, $P4bm$, and $P4mm$ phases coexist, truncates the convergence. Further increase in the poling field results in an $R3c/P4mm$ MPB, which is inclined first but becomes almost vertical at higher fields. This phase diagram points out that the MPB can be destroyed ($x = 5.5\%$ and 6%), created ($x = 7\%$), or even replaced by another MPB ($x = 6\%$) during poling. It

unambiguously demonstrates the importance of poling-induced phase transitions in interpreting the microscopic origin of macroscopic piezoelectric behaviors.

The transition from the *P4bm* phase to the *R3c* or *P4mm* ferroelectric phase is believed to be directly driven by the poling field. Its physical mechanism is presumably similar to that of an electric-field-induced antiferroelectric-to-ferroelectric transition since the ferrielectric *P4bm* structure exhibits antiparallel cation displacements in its unit cell [14,33]. Depending on the composition, the induced ferroelectric phase with parallel dipoles could be either *R3c* or *P4mm* [24,25]. The physical mechanism of the *P4mm*-to-*R3c* ferroelectric-to-ferroelectric transition, as observed in $x = 6\%$ and 7% at higher poling fields, is more complicated. Usually transitions between two ferroelectric phases purely driven by electric fields strongly depend on the direction of the applied field [36,37]. However, our electric-field *in-situ* TEM observations indicate that the *P4mm*-to-*R3c* phase transition depends very little on the direction of the applied field with respect to a specific grain in a polycrystalline aggregate. This weak orientation dependence, which is the physics base for the observed excellent correlation between the microscopic structure change and the macroscopic piezoelectric property (d_{33}) evolution in polycrystalline samples (Fig. 6.3), suggests that electric field is not the direct driving force. As in other solid solution systems [38], the piezoelectric strain developed under the applied field may have played a critical role in facilitating the phase transition.

Despite the different driving forces, these complex phase transitions trace their origin in the base compound $(\text{Bi}_{1/2}\text{Na}_{1/2})\text{TiO}_3$. As shown in Fig. 6.4, our rudimentary first-principles calculations find that the ground state of $(\text{Bi}_{1/2}\text{Na}_{1/2})\text{TiO}_3$ is the $R3c$ ferroelectric phase, which is consistent with the experimental observation [33]. The other polar phases ($P4mm$, $R3m$ and $P4bm$) have energies very close to the $R3c$ phase. These calculations suggest that it may be possible to stabilize the material in different ferroelectric phases through composition variation and/or electrical poling. The calculations also correctly predict the trend in the unit cell volume of different polar phases in $(\text{Bi}_{1/2}\text{Na}_{1/2})\text{TiO}_3$ [33]. Assuming this trend is preserved in the $(1-x)(\text{Bi}_{1/2}\text{Na}_{1/2})\text{TiO}_3-x\text{BaTiO}_3$ binary system on the $(\text{Bi}_{1/2}\text{Na}_{1/2})\text{TiO}_3$ -rich side (e.g. $x < 10\%$), the electric-field-induced phase transition sequence ($P4bm$ -to- $P4mm$ -to- $R3c$) revealed by our *in-situ* TEM experiment on $x = 6\%$ explains very well the cusp-shaped anomaly in the volume strain vs. electric field curve at the intermediate field level in this composition [35]. Finally, it should be pointed out that, instead of being a unique case for $(\text{Bi}_{1/2}\text{Na}_{1/2})\text{TiO}_3$, the presence of multiple energetically comparable ferroelectric phases is common for many perovskite compounds due to the flexibility of the perovskite structure [4-9]. The creation and destruction of MPBs during electrical poling may very likely occur in other perovskite ferroelectric systems.

6.4 Conclusions

In conclusion, our *in-situ* TEM experiments, supported by piezoelectric property measurements from bulk samples, have unambiguously demonstrated that poling fields may irreversibly destroy or create MPBs and the associated piezoelectricity enhancement. The results point out that, in addition to the virgin-state phase structure, the ferroelectric-to-ferroelectric phase transitions during poling must also be comprehensively studied to fully understand the microstructural mechanism of the macroscopic piezoelectric behaviors. This will lead to profound changes to the research on piezoelectric materials, especially the development of new lead-free piezoelectrics [8,9] for replacing the industrial standard, but environmentally hazardous, lead-containing ones. Specifically, our results broaden the search scope for new piezoelectrics by suggesting that single-phase compositions, which were largely excluded before, may also exhibit superior piezoelectricity if stable MPBs form during poling. Beyond piezoelectricity, the discovery reported here could inspire new directions in the research in other fields where competing energetically comparable states are critical, such as magnetostrictive [1] and electrocaloric effects [2]. Not only must the state of the virgin material, but also the state under the driving stimulus for target functionality, be thoroughly investigated to optimize the performance.

Acknowledgements

The National Science Foundation (NSF), through Grant DMR-1037898, supported this work. TEM experiments were performed at the U.S.-DOE Ames Laboratory.

Figures

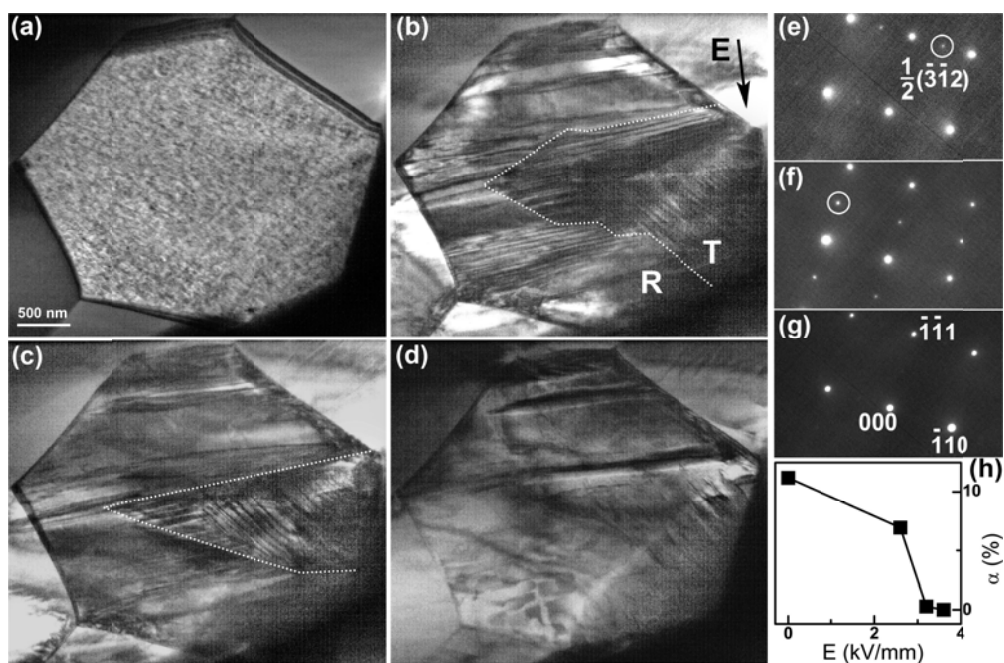


Figure 6.1 TEM bright field images along the [112] zone-axis of an originally phase-pure *P4bm* grain in $x = 6\%$ under different electric fields are displayed to demonstrate the creation and destruction of the *R3c/P4mm* MPB during poling. (a) 0 kV/mm. (b) 3.2 kV/mm. The boundary between the volume with *R3c* wedge-shaped domains (region R) and that with *P4mm* lamellar domains (region T) is highlighted by bright dotted lines. The dark arrow indicates the direction of applied fields. (c) 3.6 kV/mm. (d) 4.0 kV/mm. Representative selected area electron diffraction patterns are displayed in (e) from nanodomains at 0 kV/mm, (f) from region R at 3.2 kV/mm, and (g) from region T at 3.6 kV/mm. The superlattice diffraction spots are indicated by bright circles in (e) and (f). (h) The weakening of $1/2\{ooe\}$ superlattice diffraction spots with increasing applied fields as demonstrated by the evolution of the intensity ratio,

$$\alpha = I_{1/2(312)} / I_{(111)}.$$

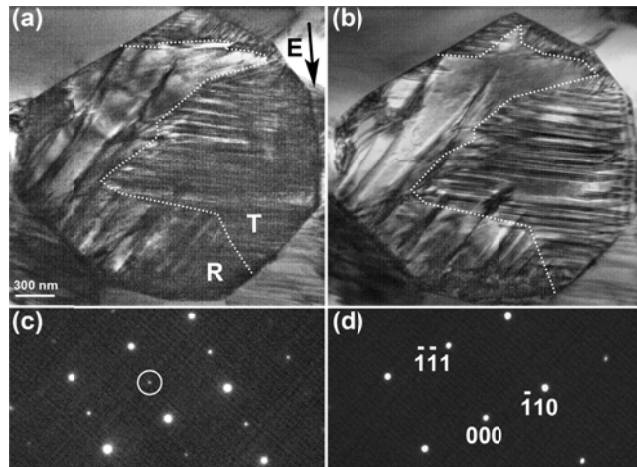


Figure 6.2 TEM bright field images along the [112] zone-axis showing the formation of the stable $R3c/P4mm$ MPB in $x = 7\%$ with originally pure $P4bm$ phase. The boundary between the volume with $R3c$ wedge-shaped domains (region R) and that with $P4mm$ lamellar domains (region T) is highlighted by bright dotted lines. The dark arrow indicates the direction of applied fields. (a) 3.0 kV/mm. (b) 4.0 kV/mm. Representative diffraction patterns taken at 3.0 kV/mm are displayed in (c) from region R with one superlattice diffraction spot highlighted by the bright circle, and in (d) from region T.

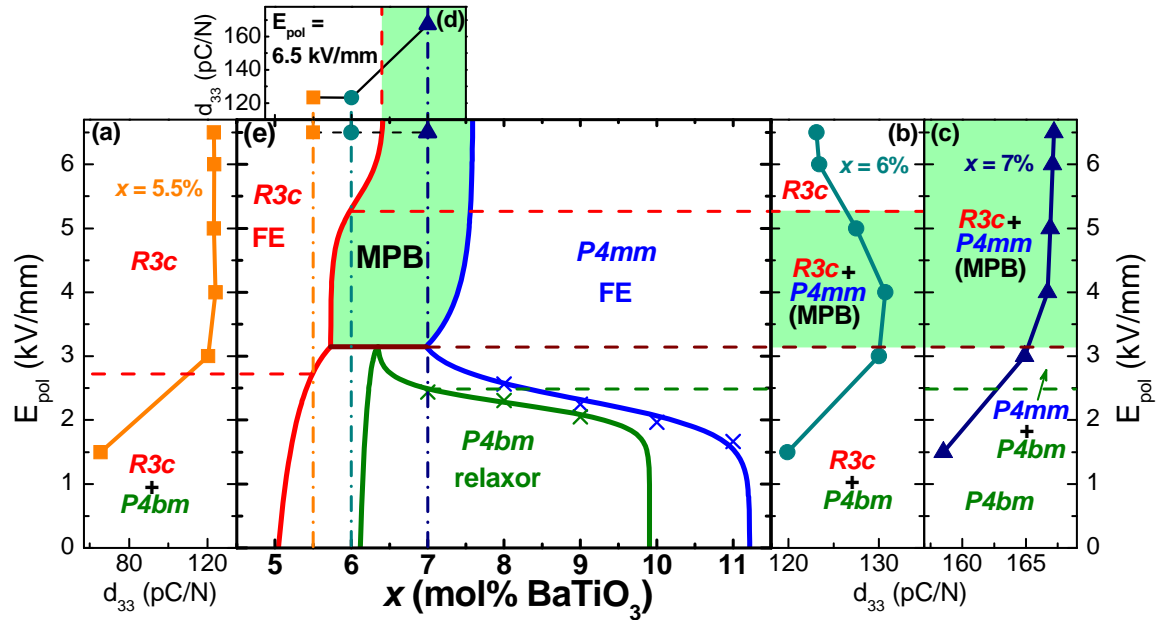


Figure 6.3 The corresponding piezoelectric property and proposed poling field vs. composition phase diagram for $(\text{Bi}_{1/2}\text{Na}_{1/2})\text{TiO}_3-\text{BaTiO}_3$. The piezoelectric coefficient d_{33} as a function of poling fields E_{pol} are displayed for (a) $x = 5.5\%$, (b) $x = 6\%$, and (c) $x = 7\%$. (d) d_{33} as a function of composition at $E_{\text{pol}} = 6.5 \text{ kV/mm}$. The error bars of the d_{33} data are smaller than the symbols and hence not shown. (e) The proposed poling field vs. composition phase diagram for $(\text{Bi}_{1/2}\text{Na}_{1/2})\text{TiO}_3-\text{BaTiO}_3$. The phase diagram shares the E_{pol} axis with (a), (b), and (c), and the x -axis with (d). FE stands for ferroelectric. Three MPBs exist in this phase diagram. Among them the electric-field-induced $R3c/P4mm$ MPB giving rise to enhanced piezoelectricity is emphasized with green shade. The phases in the virgin state are determined from previous TEM analysis [19-21]. The critical fields for $x = 5.5\%$, 6% , and 7% are determined from the piezoelectric results shown in (a), (b), and (c), as indicated by the horizontal and vertical dashed or dashed-dotted lines. The critical fields at the $P4bm/P4mm$ boundary (green and blue crosses) are estimated from the strain data on bulk ceramic samples [35].

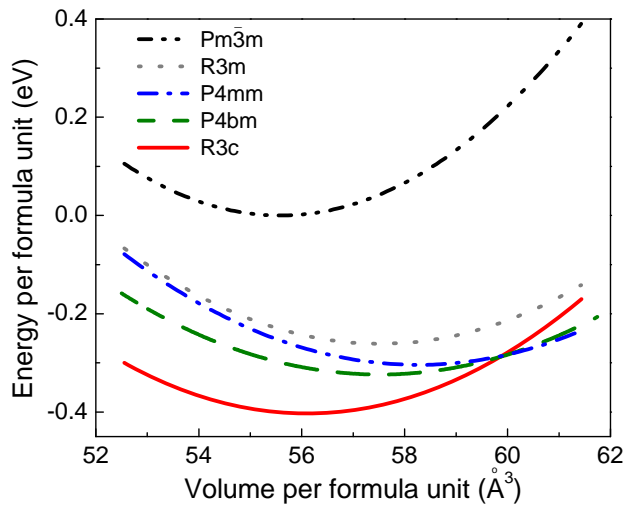


Figure 6.4 First-principles calculations of the energies of different perovskite variants for the base compound, $(\text{Bi}_{1/2}\text{Na}_{1/2})\text{TiO}_3$. The energy of the equilibrium cubic phase is arbitrarily defined as the energy zero.

Supplemental material

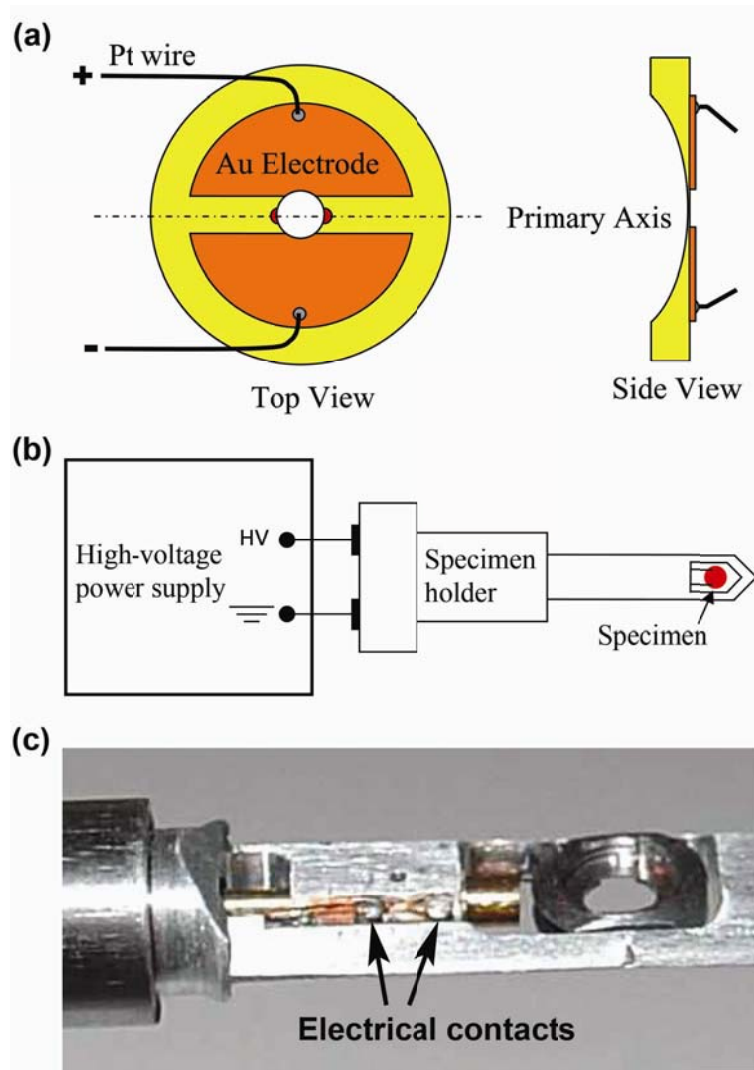


Figure S6.1 The electric-field *in-situ* transmission electron microscopy (TEM) technique. (a) Schematic illustration of the specimen configuration. The examined regions at the rim of the central perforation are marked in red. (b) Schematic illustration of the connection of the high-voltage power supply to the TEM specimen. (c) Photograph of the tip of the electric-field *in-situ* TEM specimen holder used in the present study. The Pt thin wires in (a) are connected to the two electrical contacts indicated by the dark arrows.

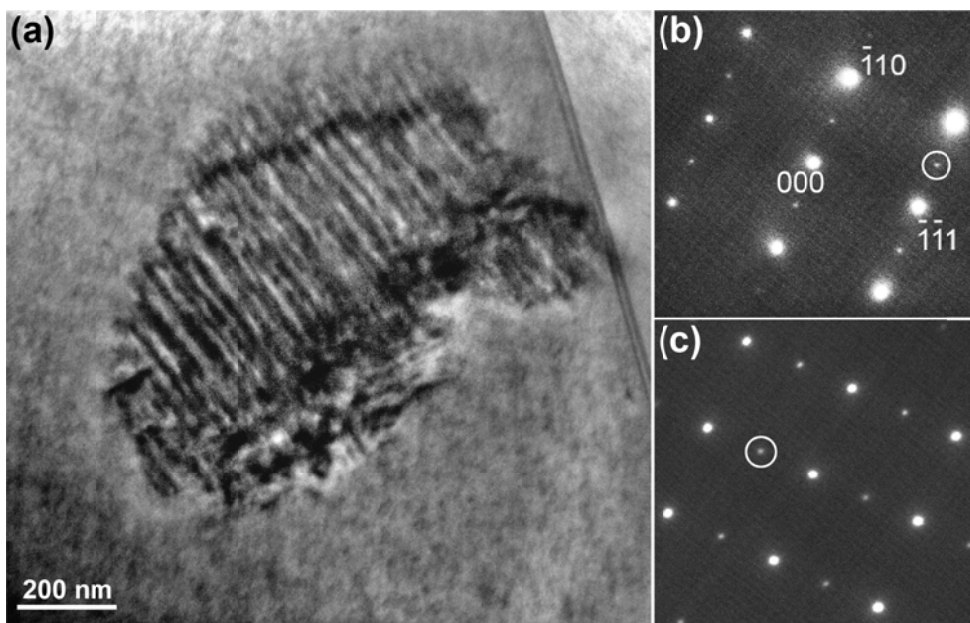


Figure S6.2 The coexistent *R3c* and *P4bm* phases revealed by TEM in $x = 6\%$ at zero electric field. (a) A TEM bright field image showing a grain with both *P4bm* nanodomains (surrounding region with faint contrast) and *R3c* large ferroelectric domains (central region with distinct domain wall contrast) along the [112] zone-axis. Approximately 40% of the grains exhibit this type domain morphology in the unpoled state. (b) Selected area electron diffraction pattern from the *P4bm* nanodomains, and (c) diffraction pattern from the *R3c* large ferroelectric domains. The superlattice diffraction spots are highlighted by bright circles.

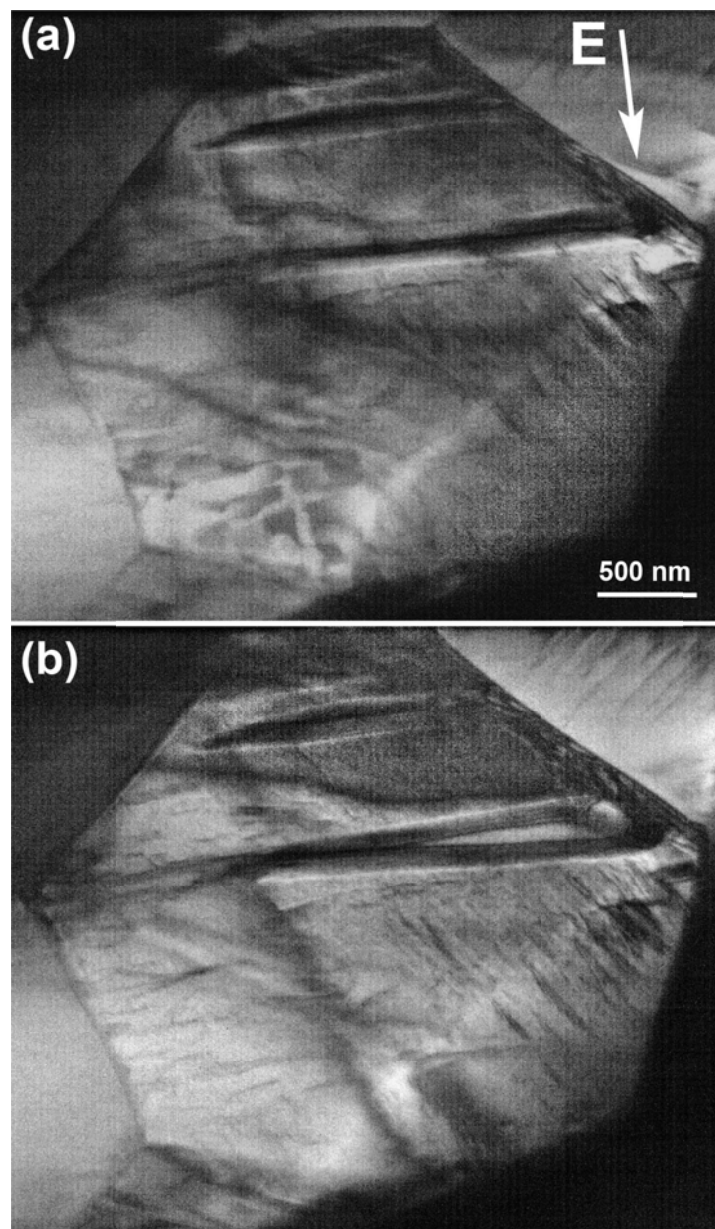


Figure S6.3 The TEM bright field images along the [112] zone-axis showing the irreversible electric-field-induced phase transitions in the composition with $x = 6\%$. (a) Under the poling electric field of 4.0 kV/mm. The bright arrow indicates the direction of the applied field. (b) Two hours after the applied field is removed.

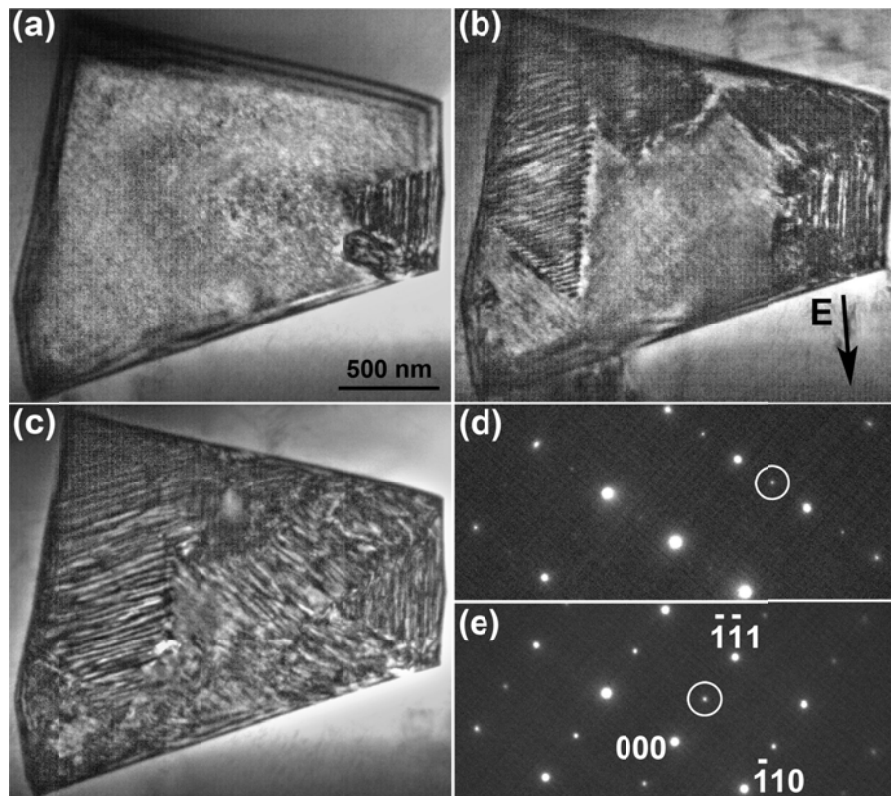


Figure S6.4 TEM bright field images along the [112] zone-axis of a grain in a specimen with $x = 5.5\%$ demonstrating the destruction of the original $R3c/P4bm$ morphotropic phase boundary (MPB) during poling. (a) 0 kV/mm. $P4bm$ nanodomains occupy most volume of the grain while $R3c$ large ferroelectric domains are located at the lower right corner of the grain. (b) 2.6 kV/mm. The dark arrow indicates the direction of the applied field. The volume with $R3c$ large ferroelectric domains starts consuming that with $P4bm$ nanodomains. (c) 3.4 kV/mm. $R3c$ large ferroelectric domains occupy the entire grain. No further phase transitions occur up to 4 kV/mm. The grain remains single $R3c$ phase after removal of electric fields. (d) Selected area electron diffraction pattern from $P4bm$ nanodomains taken at 2.6 kV/mm, and (e) diffraction pattern from $R3c$ large ferroelectric domains taken at 2.6 kV/mm. The superlattice diffraction spots are highlighted by bright circles.

References

- [1] S. Yang, H. Bao, C. Zhou, Y. Wang, X. Ren, Y. Matsushita, Y. Katsuya, M. Tanaka, K. Kobayashi, X. Song, and J. Gao, Phys. Rev. Lett. **104**, 197201 (2010).
- [2] A. S. Mischenko, Q. Zhang, J. F. Scott, R. W. Whatmore, and N. D. Mathur, Science **311**, 1270 (2006).
- [3] E. Dagotto, *Nanoscale Phase Separation and Colossal Magnetoresistance* (Springer Verlag, New York, 2003).
- [4] B. Jaffe, W. R. Cook, and H. Jaffe, *Piezoelectric Ceramics* (Academic, London, 1971).
- [5] R. Guo, L. E. Cross, S.-E. Park, B. Noheda, D. E. Cox, and G. Shirane, Phys. Rev. Lett. **84**, 5423 (2000).
- [6] K. A. Schonau, L. A. Schmitt, M. Knapp, H. Fuess, R.-A. Eichel, H. Kungl, and M. J. Hoffmann, Phys. Rev. B **75**, 184117 (2007).
- [7] D. Phelan, X. Long, Y. Xie, Z.-G. Ye, A. M. Glazer, H. Yokota, P. A. Thomas, and P. M. Gehring, Phys. Rev. Lett. **105**, 207601 (2010).
- [8] W. Liu and X. Ren, Phys. Rev. Lett. **103**, 257602 (2009).
- [9] J. Rödel, W. Jo, K. T. P. Seifert, E. M. Anton, T. Granzow, and D. Damjanovic, J. Am. Ceram. Soc. **92**, 1153 (2009).
- [10] M. Hinterstein, J. Rouquette, J. Haines, Ph. Papet, M. Knapp, J. Glaum, and H. Fuess, Phys. Rev. Lett. **107**, 077602 (2011).

- [11] Y. Sato, T. Hirayama, and Y. Ikuhara, Phys. Rev. Lett. **107**, 187601 (2011).
- [12] X. Tan, Z. Xu, J. K. Shang, and P. Han, Appl. Phys. Lett. **77**, 1529 (2000).
- [13] H. He and X. Tan, Phys. Rev. B **72**, 024102 (2005).
- [14] X. Tan, C. Ma, J. Frederick, S. Beckman, and K. G. Webber, J. Am. Ceram. Soc. **94**, 4091 (2011).
- [15] C. A. Randall, D. J. Barber, and R.W. Whatmore, J. Microsc. **145**, 275 (1987).
- [16] J. Yao, L. Yan, W. Ge, L. Luo, J. Li, D. Viehland, Q. Zhang, and H. Luo, Phys. Rev. B **83**, 054107 (2011).
- [17] F. Cordero, F. Craciun, F. Trequattrini, E. Mercadelli, and C. Galassi, Phys. Rev. B **81**, 144124 (2010).
- [18] W. Jo, J. E. Daniels, J. L. Jones, X. Tan, P. A. Thomas, D. Damjanovic, and J. Rödel, J. Appl. Phys. **109**, 014110 (2011).
- [19] C. Ma and X. Tan, Solid State Commun. **150**, 1497 (2010).
- [20] C. Ma, X. Tan, E. Dul'kin, and M. Roth, J. Appl. Phys. **108**, 104105 (2010).
- [21] C. Ma and X. Tan, J. Am. Ceram. Soc. **94**, 4040 (2011).
- [22] T. Takenaka, K. Maruyama, and K. Sakata, Jpn. J. Appl. Phys., Part 1 **30**, 2236 (1991).
- [23] Y. Hiruma, H. Nagata, and T. Takenaka, J. Appl. Phys. **104**, 124106 (2008).
- [24] J. E. Daniels, W. Jo, J. Rödel, and J. L. Jones, Appl. Phys. Lett. **95**, 032904 (2009).
- [25] H. Simons, J. Daniels, W. Jo, R. Dittmer, A. Studer, M. Avdeev, J. Rödel, and M.

Hoffman, Appl. Phys. Lett. **98**, 082901 (2011).

- [26] See the section of “Supplemental material” at the end of this chapter for the configuration of the *in-situ* TEM experiment, the grain with mixed *R3c* and *P4mm* phases in $x = 6\%$, the irreversibility of electric-field-induced phase transitions, and the electric-field *in-situ* TEM results of $x = 5.5\%$.
- [27] W. Kohn and L. J. Sham, Phys. Rev. **140**, 1133 (1965).
- [28] D. M. Ceperley and B. J. Alder, Phys. Rev. Lett. **45**, 566 (1980).
- [29] P. E. Blochl, Phys. Rev. B **50**, 17953 (1994).
- [30] H. J. Monkhorst and J. D. Pack, Phys. Rev. B **13**, 5188 (1976).
- [31] A. M. Glazer, Acta Cryst. A **31**, 756 (1975).
- [32] D. I. Woodward and I. M. Reaney, Acta Cryst. B **61**, 387 (2005).
- [33] G. O. Jones and P. A. Thomas, Acta Cryst. B **58**, 168 (2002).
- [34] V. Dorcet and G. Trolliard, Acta Mater. **56**, 1753 (2008).
- [35] W. Jo and J. Rödel, Appl. Phys. Lett. **99**, 042901 (2011).
- [36] S. Wada, S. Suzuki, T. Noma, T. Suzuki, M. Osada, M. Kakihana, S.-E. Park, L. E. Cross, and T. R. Shroud, Jpn. J. Appl. Phys. **38**, 5505 (1999).
- [37] X. Zhao, W. Qu, X. Tan, A. Bokov, and Z.-G. Ye, Phys. Rev. B **75**, 104106 (2007).
- [38] X. Tan, J. Frederick, C. Ma, W. Jo, and J. Rödel, Phys. Rev. Lett. **105**, 255702 (2010).

CHAPTER 7. Concluding Remarks

7.1 General conclusions

With the overall motivation to promote the development of high-performance lead-free piezoelectric materials, this dissertation explores and finally interprets the microscopic origin for the high piezoelectricity of the most extensively studied lead-free piezoelectric material, $(1-x)(\text{Bi}_{1/2}\text{Na}_{1/2})\text{TiO}_3-x\text{BaTiO}_3$ solid solutions, through various TEM studies.

The study consists of three steps. In the first step, through a detailed conventional TEM study on the unpoled ceramics with $x = 4\%, 6\%, 7\%, 9\%$, and 11% , the phase relationship of this solid solution is demonstrated to vary significantly after electrical poling. In comparison with the poled ceramics, an additional phase region with *P4bm* nanodomains is present in the unpoled ceramics, separating the *R3c* and *P4mm* phase regions. The corresponding dielectric analysis reveals an excellent room-temperature structure-property correlation against composition. Based on these, the physical origin of the unique electric behavior of the *P4bm* phase, which is under debate for years, is explained; the antiferroelectric behaviors arise from the *P4bm* crystal structure that exhibits antiparallel cation displacements and yields a negligibly small macroscopic polarization, while the relaxor ferroelectric characteristics are attributed to the weakly polar *P4bm* nanodomains. A new term “relaxor ferrielectric” is coined to describe this phenomenon. A phase diagram

is constructed to summarize the structure-property relationship of this system in the virgin state.

The second step of the study also focuses on the unpoled ceramics. In the host compound BNT, a structure-property decoupling is present at high temperatures. However, due to the absence of detailed temperature-dependent structural study in literature, whether such a decoupling exists in the BNT-BT solid solutions remains an open question. Therefore, the hot-stage TEM is performed on $x = 6\%$ and 11% to investigate the structural transitions of unpoled ceramics at high temperatures. The excellent structure-property correlation against composition observed at room temperature persists across the depolarization temperature T_d , which supports the aforementioned “relaxor ferrielectric” model. With further increasing temperature, the structure-property decoupling similar to that in pure BNT is observed. No structural change was observed for both compositions across T_{RE} and T_m . At temperatures way above both T_{RE} and T_m , the tetragonal-to-cubic transition takes place diffusively with a broad temperature window showing coexisting phases. These results reveal the structure-property relationship of BNT-BT against temperature, and extend the phase diagram of unpoled ceramics up to $600\text{ }^\circ\text{C}$.

Finally, based on the structure-property relationships of unpoled ceramics, the electric-field *in-situ* TEM study is performed to probe the microscopic origin for the high

piezoelectricity in $(1-x)$ BNT- x BT. The study focuses on three compositions in the vicinity of the MPB, $x = 5.5\%$, 6% , and 7% . In sharp contrast to conventional expectations, it is observed that the MPB in BNT-BT, along with the associated strong piezoelectricity, can be created, destroyed, or even replaced by another MPB during poling. For $x = 5.5\%$, the virgin-state $R3c/P4bm$ MPB is destroyed before the field is high enough to thoroughly pole the ceramic. Thus it does not exhibit a very strong piezoelectricity. For $x = 6\%$, the virgin-state $R3c/P4bm$ MPB is replaced at intermediate poling fields by an $R3c/P4mm$ MPB, which disappears at higher poling fields. Consequently, the piezoelectricity peaks at intermediate poling fields but diminishes with further increase in the field level. For $x = 7\%$, an $R3c/P4mm$ MPB forms out of the single $P4bm$ phase during poling and persists at high poling fields. Because of such a stable poling-induced MPB, this virgin-state single-phase composition displays the optimal piezoelectricity in this system. A poling field vs composition phase diagram is constructed to describe the complicated electric-field-induced phase transitions during poling.

The observation of the creation and destruction of MPBs during electrical poling in BNT-BT not only elucidates the microstructural mechanism for the high piezoelectricity in this specific system, but also broadens the search scope for high-performance piezoelectrics: it suggests even the single-phase compositions, which have been largely ignored in solid solutions for the past six decades, may also exhibit superior piezoelectricity if stable MPBs

form during poling. Such a fundamental alteration to the long-standing guiding rule adds a new dimension to the development of next generation piezoelectrics.

7.2 Directions for future research

Although the studies presented in this dissertation clarify the microstructural mechanism of the high piezoelectricity for the optimal $(1-x)$ BNT- x BT compositions, i.e. those in the vicinity of $x = 6\%$, there are still questions remaining unanswered in other regions of the poling field vs electric field phase diagram. This section will briefly discuss these questions, and then propose the studies aiming at answering them.

First of all, the composition- and poling-field-dependent structural evolution below the lower composition limit of Fig. 6.3, i.e. $0\% \leq x \leq 4\%$, deserves more detailed investigation. Recently a study on the strain vs electric field behaviors of $(1-x)$ BNT- x BT ceramics reveals that, in addition to the compositions showing $P4bm$ nanodomains ($6\% \leq x \leq 11\%$), the low-BT-content compositions ($0\% \leq x \leq 4\%$) also experience electric-field-induced phase transitions as characterized by the sharp increase of the volume strain.¹ The critical field of this electric-field-induced phase transition decreases as BT content increases. For the composition $x = 5\%$, no electric-field-induced phase transition occurs. These could possibly imply an MPB unstable against poling field exists in the vicinity of $x = 4\%$. However, no

structural study has been performed to verify this. It should be pointed out that recently the rhombohedral $R3c$ symmetry of pure BNT has been questioned.^{2,3} Instead, it is proposed that the space group of BNT is monoclinic Cc .^{2,3} It is possible that the presumed MPB at $x = 4\%$ separates an $R3c$ ($x > 4\%$) and Cc ($x < 4\%$) phase. However, due to the weakness of the intensity of the critical superlattice diffractions, the x-ray and neutron diffraction cannot distinguish these two symmetries very conveniently even in the single-phase situation. In contrast, TEM can alleviate the difficulty under such a circumstance.⁴ A conventional TEM study on the composition $x = 0\%$, 4% , and 5% is thus proposed to probe the structural evolution and verify the presumed existence of the $R3c/Cc$ MPB in these low-BT-content compositions.

Second, further electric-field-induced phase transitions could possibly occur at $E_{pol} > 6.5$ kV/mm in compositions showing the stable electric-field-induced $R3c/P4mm$ MPB ($6.5\% \leq x \leq 7.5\%$). The $R3c$ phase in this MPB exhibits antiphase oxygen octahedra tilting around the $<111>$ axis.⁶ It has been reported that intense electric fields have a tendency to de-tilt the oxygen octahedra in the $R3c$ phase, leading to a structural transition from the $R3c$ to $R3m$ symmetry.⁵ In another word, at a poling field higher than 6.5 kV/mm there could be a further electric-field-induced $R3c$ -to- $R3m$ transition for compositions with $6.5\% \leq x \leq 7.5\%$, replacing the $R3c/P4mm$ MPB with an $R3m/P4mm$ MPB. The anti-phase boundaries of oxygen octahedra tilting were known to hamper the domain wall motion process during

poling and thus result in inferior piezoelectricity.⁷ This implies that the *R3c*-to-*R3m* transition, which eliminates these anti-phase boundaries through straightening the tilted oxygen octahedra, could possibly further enhance the piezoelectricity in $6.5\% \leq x \leq 7.5\%$. However, this has never been experimentally verified, because the relatively low density of the conventionally sintered ceramics leads to low dielectric breakdown strength, which prevents the successful application of a poling field higher than 7 kV/mm. Therefore, hot-isostatic pressing (HIP) is proposed to improve the density of the ceramics. The HIPped ceramics will first be poled at a series of fields above 7 kV/mm with an increasing sequence of field level. If the recorded d_{33} vs E_{pol} curve shows an abnormal increase like those observed in Fig. 6.3(b), the *R3c*-to-*R3m* transition is very likely to occur. An electric-field *ex-situ* and/or *in-situ* x-ray diffraction study is then proposed to confirm the *R3c*-to-*R3m* transition and reveal the detailed crystal structure evolution during high-field poling.

Last but not least, more in-depth TEM study needs to be performed to investigate the dynamic switching and coalescence of *P4bm* nanodomains under electric fields. In the commonly accepted model for relaxor ferroelectrics,⁸ the non-ergodic relaxor will be irreversibly forced into a normal ferroelectric under a sufficiently strong electric field. Although this model provides reasonable explanations for many macroscopic behaviors, the coalescence of nanodomains into micrometer-sized ferroelectric domains described in this

model has never been actually visualized before. The $(1-x)$ BNT- x BT ceramic with $x = 7\%$ happens to be an excellent composition for such a purpose; it exhibits weakly polar nanodomains just like typical relaxor ferroelectrics, and, unlike $\text{Pb}(\text{Mg}_{1/3}\text{Nb}_{2/3})\text{O}_3$ -based relaxors, these nanodomains can be unambiguously visualized through centered-dark-field imaging (Fig. 5.4). A combination of electric-field *in-situ* TEM and centered-dark-field imaging can reveal the actual process of the nanodomain switching and coalescence in real time. This not only offers supportive evidences for the current model of relaxor ferroelectrics, but also provides insight into the detailed microscopic behaviors of nanodomains. Such study is critical to the fundamental understanding of the physics for relaxor ferroelectric materials.

References

- ¹ W. Jo and J. Rödel, Appl. Phys. Lett. **99**, 042901 (2011).
- ² S. Gorfman and P. A. Thomas, J. Appl. Cryst. **43**, 1409 (2010).
- ³ E. Aksel, J. S. Forrester, J. L. Jones, P. A. Thomas, K. Page, and M. R. Suchomel, Appl. Phys. Lett. **98**, 152901 (2011).
- ⁴ D. I. Woodward and I. M. Reaney, Acta Cryst. B **61**, 387 (2005).
- ⁵ X. Tan, C. Ma, J. Frederick, S. Beckman, and K. G. Webber, J. Am. Ceram. Soc. **94**, 4091 (2011).

⁶ G. O. Jones and P. A. Thomas, *Acta Cryst. B* **58**, 168 (2002).

⁷ R. Eitel and C. A. Randall, *Phys. Rev. B* **75**, 094106 (2007).

⁸ A. A. Bokov and Z.-G. Ye, *J. Mater. Sci.* **41**, 31 (2006).

ACKNOWLEDGEMENTS

I would like to take this opportunity to express my sincere thanks to those who have kindly helped and supported me during my Ph.D. study.

First and foremost, I would like to thank my Ph.D. advisor, Dr. Xiaoli Tan, who kindly gave me the opportunity to work on this interesting project. The benefits I received from his perceptive views, invaluable advices, and precious discussions throughout my entire Ph.D. study can never be exaggerated. What I learned from him are not only experimental skills and research methods, but also how to be a good scientist. Beyond research, his trust, kindness, and enthusiasm for life make me a better person. It is my great fortune to have been his student.

I would like to thank the professors in my Program of Study committee, Prof. Mufit Akinc, Prof. Nicola Bowler, Prof. Scott P. Beckman, and Prof. Gordon J. Miller, for their time and patience in my thesis work. Particularly I wish to thank Prof. Beckman for his nice ab initio calculations in our paper currently under review in *Physical Review Letters*.

Special thanks to Dr. Jiaqiang Yan, Dr. Ying Zhang, and Dr. Ying Cai, for generously sharing their research experiences with me. Their encouragement and support are definitely indispensable for my achievements during the Ph.D. study.

I would like to thank the previous and current group fellows, Dr. Hui He, Dr. Weiguo Qu, Dr. Xiaohui Zhao, Dr. Rewadee Wongmaneerung, Dr. Orawan Khamman, Mr. Joshua Frederick, Mrs. Sarah Beckman, Mr. Thanapong Sareein, Mr. Hanzheng Guo, Mr. Weixing Sun, Mr. Samuel Eli Young, and Mr. Xiaoming Liu, for their help in my experiments, suggestions for improving my Ph.D. preliminary/final oral exams, and invaluable friendship. Especially, I want to thank Mr. Hanzheng Guo, who prepared many good ceramic samples for my TEM study.

Thanks must also go to Dr. Matthew J. Kramer, Dr. Yaqiao Wu, Dr. Francis Laabs, Dr. Qingfeng Xing, Dr. Dan Shechtman, Dr. Zhiqun Lin, Dr. R. William McCallum, Dr. Kevin W. Dennis, Dr. Yue He, Dr. Lei Bi, Dr. Juejun Hu, Dr. Wei Zhao, Dr. Min Xu, Dr. Min Zou, Dr. Jie Ma, Dr. Ni Ni, Dr. Youwen Xu, Dr. Yunus Eren Kalay, Dr. Ilkay Kalay, Dr. Zhongyuan Qian, Dr. Li Li, Ms. Liwen Wan, Ms. Qing Cao, and Mr. Xiao Wang for their kind help, support, and discussion.

Last but not least, I would like to express my deepest thanks to my parents who have always been very supportive to me. Without their continuous love, I will never be able to accomplish this work.

APPENDIX: Publication List

1. **C. Ma**, H. Guo, S. Beckman, X. Tan, Creation and destruction of morphotropic phase boundaries through electrical poling of ferroelectric materials, *Physical Review Letters*, **2012**, under review.
2. W. Sun, J. E. De León, **C. Ma**, X. Tan, M. R. Kessler, Novel Si/cyanate ester nanocomposites with multifunctional properties, *Composites Science and Technology*, **2012**, under review.
3. X. Tan, **C. Ma**, J. Frederick, S. Beckman, K. G. Webber, The antiferroelectric \leftrightarrow ferroelectric phase transition in lead-containing and lead-free perovskite ceramics, *Journal of the American Ceramic Society* **2011**, *94*, 4091.
4. S. Zhang, H. J. Lee, **C. Ma**, X. Tan, Sintering effect on microstructure and properties of (K,Na)NbO₃ ceramics, *Journal of the American Ceramic Society* **2011**, *94*, 3659.
5. **C. Ma**, X. Tan, *In situ* transmission electron microscopy study on the phase transitions in lead-free (1- x)(Bi_{1/2}Na_{1/2})TiO₃- x BaTiO₃ ceramics, *Journal of the American Ceramic Society* **2011**, *94*, 4040.
6. X. Tan, J. Frederick, **C. Ma**, W. Jo, J. Rödel, Can an electric field induce an antiferroelectric phase out of a ferroelectric phase?, *Physical Review Letters* **2010**, *105*, 255702.
7. **C. Ma**, X. Tan, E. Dul'kin, M. Roth, Domain structure-dielectric property relationship in lead-free (1- x)(Bi_{1/2}Na_{1/2})TiO₃- x BaTiO₃ ceramics, *Journal of Applied Physics* **2010**, *108*, 104105.
8. **C. Ma**, X. Tan, Phase diagram of unpoled lead-free (1- x)(Bi_{1/2}Na_{1/2})TiO₃- x BaTiO₃

- ceramics, *Solid State Communications* **2010**, *150*, 1497.
9. **C. Ma**, X. Tan, Morphotropic phase boundary and electrical properties of lead-free $(1-x)\text{BaTiO}_3-x\text{Bi}(\text{Li}_{1/3}\text{Ti}_{2/3})\text{O}_3$ ceramics, *Journal of Applied Physics* **2010**, *107*, 124108.
 10. X. Tan, J. Frederick, **C. Ma**, E. Aulbach, M. Marsilius, W. Hong, T. Granzow, W. Jo, J. Rödel, Electric-field-induced antiferroelectric to ferroelectric phase transition in mechanically confined $\text{Pb}_{0.99}\text{Nb}_{0.02}[(\text{Zr}_{0.57}\text{Sn}_{0.43})_{0.94}\text{Ti}_{0.06}]_{0.98}\text{O}_3$, *Physical Review B* **2010**, *81*, 014103.
 11. **C. Ma**, J.-Q. Yan, K. W. Dennis, R. W. McCallum, X. Tan, Synthesis, thermal stability and magnetic properties of the $\text{Lu}_{1-x}\text{La}_x\text{Mn}_2\text{O}_5$ solid solution, *Journal of Solid State Chemistry* **2009**, *182*, 3013.
 12. **C. Ma**, J.-Q. Yan, K. W. Dennis, A. Llobet, R. W. McCallum, X. Tan, Effect of oxygen content on the magnetic properties of multiferroic $\text{YMn}_2\text{O}_{5+\delta}$, *Journal of Physics.: Condensed Matter* **2009**, *21*, 346002.
 13. **C. Ma**, J.-Q. Yan, K. W. Dennis, R. W. McCallum, X. Tan, Size-dependent magnetic properties of high oxygen content $\text{YMn}_2\text{O}_{5+\delta}$ multiferroic nanoparticles, *Journal of Applied Physics* **2009**, *105*, 033908.